Mathematical Modelling of Intramembranous Bone Formation During Fracture Healing

Louise Manitzky

BEng(Elec & CompEng)/BMaths
BAppSc(Hons)(Maths)

Principle Supervisor: Prof. Graeme Pettet
Associate Supervisor: A/Prof. Troy Farrell

Mathematical Sciences School
Science and Engineering Faculty
Queensland University of Technology

2014

Submitted in fulfilment of the requirements of the degree of
Doctor of Philosophy

Keywords

fracture healing, intramembranous bone formation, mathematical modelling, mineralisation, moving boundary, osteoblast differentiation, Turing patterns.

Abstract

Many processes must occur in sequence to ensure the successful healing of a bone fracture. At the fracture gap, healing progresses through endochondral bone formation. A cartilage matrix bridges the fracture gap and provides stability. This cartilage matrix is subsequently replaced with a bony matrix and clinically healing is considered complete when the gap has been fully bridged by bone tissue. Distal to the fracture site new bone is being formed through a different process, intramembranous bone formation. During intramembranous bone formation, new bone forms directly without a precursor cartilage matrix. In fracture healing intramembranous bone occurs in regions of high mechanical stability. Histological observations reveal that the new intramembranous bone appears in the early stages of fracture healing and has a woven appearance.

During intramembranous bone formation many complex cellular and chemical interactions take place. In this thesis we examine some of these interactions, and use them to build mathematical models to describe some of the processes that are taking place. In particular we investigate the regulation of the cellular differentiation of progenitor cells to become osteoblasts, and the mineralisation of new bone tissue as they occur during intramembranous bone formation.

Before new bone can form, osteoblast progenitor cells present in the callus must differentiate to become osteoblasts, the bone forming cells. This process is regulated by many different proteins present during the fracture healing process. Members of the bone morphogenetic protein (BMP) family are known to enhance the differentiation of progenitor cells to osteoblasts. However the known BMP antagonist noggin reduces the effectiveness of the BMPs. We build a model for the differentiation of progenitors to osteoblast due to the

effects of BMP and noggin. We demonstrate that the model can be reduced to a model for just BMP and noggin. This reduced model has a form that gives rise to Turing patterns. We demonstrate that the pattern forming ability of the model is conserved when the full model is considered, and that the temporal and spatial appearance of the patterning seems consistent with histological observations. We also consider the effects of a BMP source on one of the boundaries. This gives rise to a moving front of pattern formation, which moves at a speed much greater than the expected growth rate of the callus. We further extend this model to include a moving boundary to represent the growth of the callus. We show that the growth rate of the callus has an effect on the final appearance of the pattern and on the transient structures that are observed as the patterns evolve.

We also build a model for the mineralisation of the new bone tissue. Osteoblasts produce new bone tissue by first producing a collagen matrix and then regulating the deposition of mineral onto the matrix, a process referred to as mineralisation. The removal of the mineralisation inhibitor pyrophosphate (PP_i) is seen as a key requirement for mineralisation to occur. This is facilitated by osteoblasts by the production of an enzyme, tissue non-specific alkaline phosphatase (TNAP). The removal of PP_i by TNAP also increases the local concentration of phosphate (P_i), an important component of bone mineral. We start with a kinetic model for TNAP, PP_i and P_i. This model qualitatively matches results seen in cell mineralisation assays. We further take these kinetics and use them to build a model that includes the movement of the mineralisation front. Using this we demonstrate the effect that varying parameters and boundary conditions have on the speed of mineralisation.

Statement of Original Authorship

The work contained in this thesis has not been previously submitted to meet requirements for an award at this or any other higher education institution. To the best of my knowledge and belief, the thesis contains no material previously published or written by another person except where due reference is made.

Louise Manitzky

QUT Verified Signature

Signature:

Date: 5/11/14

Acknowledgements

There are many people who need to be thanked for their help during the last four years leading to the completion of this thesis. Firstly to my supervisor Graeme. Thanks for your patience, support, reassurance and guidance along the way. To my associate supervisor Troy, thanks for your advice towards the end.

Thanks to my family, particularly my parents for their love and support. Thanks Dad for proof reading and picking up all the misplaced commas.

To my fellow PhD students, thanks for all the fun times and for reminding me I'm not the only person crazy enough to go down this path. To my outside friends for providing welcome distractions. In particular I want to thank Mel, Nors, and Connie, who got me through when times were tough.

Finally thanks (I think) to Alan Williams, who planted the seed that I should do a PhD many years ago, and then once I had enrolled never failed to remind me that a PhD equals suffering.

Contents

List of Tables

List of Figures

1

Introduction

1.1 Overview

Bone is unique among the tissues of the body in that at the conclusion of successful healing the new tissue is identical to the old tissue in form and function. However within a clinical setting successful healing within a timely fashion does not always occur, leading to a delayed union. Of greater concern is that occasionally healing ceases altogether before completion leading to a non-union of the fracture. This non-union can be painful as well as physically disabling for a patient. The rate of non-union varies with different bones and is influenced by a range of factors but is generally estimated to be around 5–10%. There is a significant financial cost to treat non-unions (Tosounidis et al. 2009) and the standard approach to treatment is surgical intervention (Antonova et al. 2013, Kanakaris & Giannoudis 2007).

Traditionally the surgical intervention is aimed at stabilising the fracture site and often a bone graft is used to further induce bone formation (Antonova et al. 2013, Schoelles et al. 2005). Due to potential complications during the bone graft procedure alternative approaches have been developed. One alternative is the use of collagen sponges containing BMP-2 or -7. More recent research has been conducted into the use of bone scaffolds. A commonly researched scaffold material is a calcium-phosphate compound similar to bone mineral. Methods researched to increase the ability of these scaffolds to induce bone formation include seeding with stem cells and implantation of growth factors such as BMP (Bose et al. 2012).

Stability of the fracture site is undoubtedly an important factor in ensuring successful healing. However the roles played by growth factors and other signalling molecules cannot be overlooked, particularly as their potential role

in clinical settings increases. Whilst much is known about the actions of growth factors and other signalling molecules in the regulation of fracture healing there are still many gaps in the knowledge. In particular from a clinical point of view it is difficult to determine the optimal timing and dosage of application of a growth factor to ensure successful bone growth. Mathematical modelling can help to fill the gaps in the biological knowledge. These models act as another tool to help interpret experimental results or test hypothesises, these models may even raise new questions or give rise to a new hypothesis that can help guide experimental research (Pivonka & Dunstan 2012, Geris et al. 2010).

1.1.1 Intramembranous Bone Formation

Fracture healing is achieved through a complex series of events. The current generally accepted interpretation of bone healing considers a number of phases. The first phase is dominated by the inflammation response to the initial injury. The next stage is the reparative phase. During this stage two separate types of bone formation, intramembranous where new bone is formed directly and endochondral where bone formation is preceded by cartilage growth, occur to form a callus which bridges the fracture gap. Once the gap has been bridged with bony material the final remodelling phase begins. In the remodelling stage the callus is resorbed and the bone is restored to its original structure (Prendergast & van der Meulen 2001).

Generally, at the fracture gap, new bone is formed through endochondral bone formation. Here the fracture gap may first be bridged by a cartilaginous tissue which provides increased stabilisation. The cartilage is then converted to mineralised bone through a concerted process involving osteoblasts (bone forming cells) and chondrocytes (cartilage cells). At the periphery of the callus however new bone forms through a different mechanism.

Intramembranous bone formation (or intramembranous ossification) is when bone is formed directly without an intermediary cartilage matrix. In fracture healing it occurs during the early stages of repair and is typically associated with the new bone that forms in the regions some distance from the fracture gap, at the periphery of the callus. These regions are characterised as having high mechanical stability with little interfragmentary movement and deformation of tissue. Indeed, intramembranous bone formation has been shown to

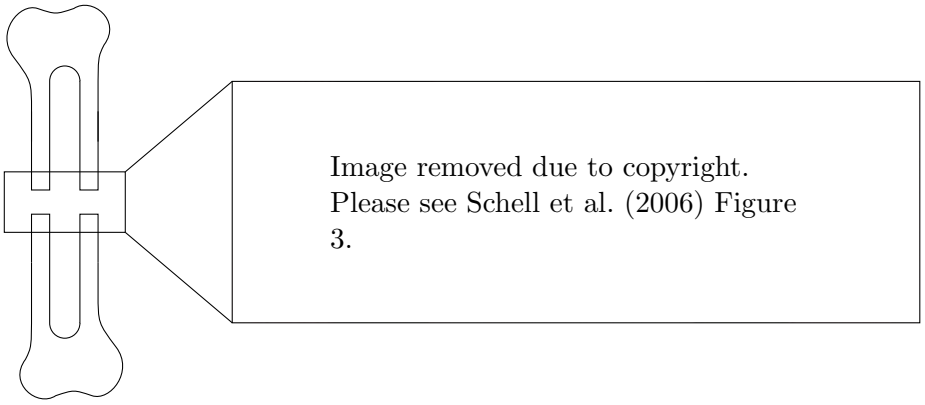

Figure 1.1: Histological section showing new intramembranous bone formation. The section is from a sheep, taken two weeks after a tibial osteotomy (Schell et al. 2006). The black rectangular regions are the pre-existing cortical bone, the irregularly patterned black material in the regions adjacent to the cortical bone is the new intramembranous bone. The white region is bone marrow and the pink regions are fibrous tissue.

be independent of overall fracture gap stability (Epari et al. 2006).

As intramembranous bone formation occurs in areas of high mechanical stability, it makes an ideal starting point for building a mathematical model to investigate bioregulatory effects on fracture healing. Also of interest is the specific structure that is apparent in newly formed intramembranous bone. This is illustrated in Figure 1.1 which shows a histological slice taken 2 weeks following a sheep osteotomy. Here the black rectangular regions are the pre-existing cortical bone, and the white region that they surround is the bone marrow. The new intramembranous bone can be seen adjacent to the pre-existing cortical bone, due to its appearance this new bone is sometimes referred to as spongy or woven bone. We note that there is a significant difference in the amount of bone formation on either side of the callus and that this may in part be due to spatial heterogeneities in the soft tissue surrounding the bone (Epari et al. 2006). Looking at the intramembranous bone on the left of the callus, we see that the new bone is not completely random in its appearance. Near the fracture gap the spicules of bone growth appear aligned perpendicular to the cortical bone surface, whereas the near the cortical bone surface the growth appears to be aligned with the bone surface.

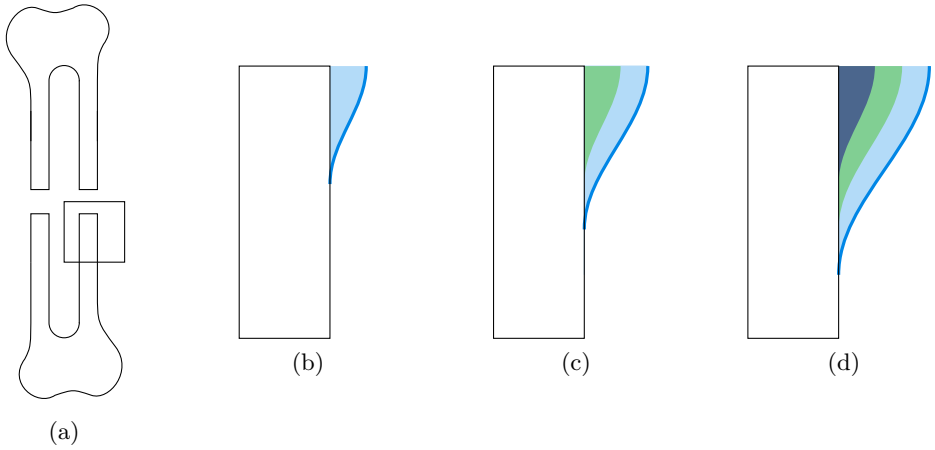

Figure 1.2: Schematic demonstrating the growth of a fracture callus. (a) represents a long section of a typical long bone with a mid shaft fracture. (b), (c) and (d) represent the growth of the callus in the region indicated in (a). The white area is existing cortical bone, the light blue is the region where cell proliferation is occurring, the green is the region of cellular differentiation and the dark blue is where new bone formation has occurred. As the callus grows the region of interest also changes shape.

1.1.2 Mathematical Modelling For Fracture Healing

Traditionally mathematical models of fracture healing have focused on the mechanical forces throughout the fracture callus. More recently models have been developed that consider bioregulatory factors. Even more recently these two approaches have been combined in the form of hybrid models. These models all work on a callus scale. They have success at predicting regions where intramembranous or endochondral formation will occur and in some cases model the new bone formation using simple relationships. However none of these models focus on the processes that are occurring during intramembranous bone formation in specific detail (for a more detailed review of the existing models of fracture healing please see Chapter 2).

Instead we take a different tack in building a model for fracture healing. We look specifically at intramembranous bone formation as it is occurring during callus formation, with the aim of adding to the knowledge of the effect of growth factors and other bioregulatory factors on fracture healing.

Intramembranous bone formation occurs during the early stages of fracture repair and at the periphery of the callus. A schematic of the stages in this process is illustrated in Figure 1.2. As the bone is fractured the periosteum, the

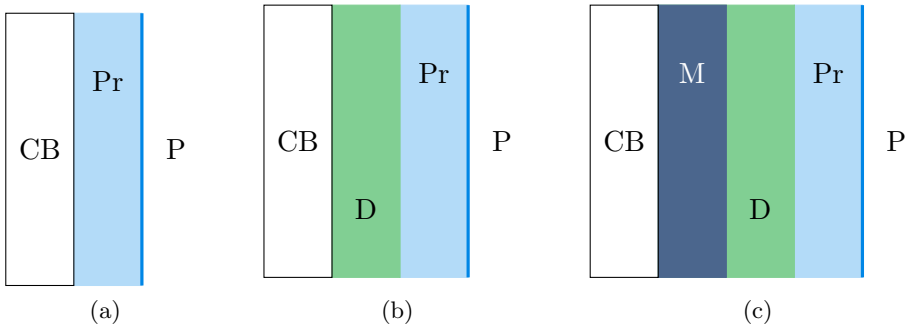

Figure 1.3: Simplified schematic of the region of the fracture callus where intramembranous bone formation is occurring. We consider the callus to be composed of three regions, the proliferative region where the stem cells from the periosteum are proliferating, a differentiation region where the stem cells differentiate to become osteoblasts, and a mineralisation region where the new bone is being formed. Legend: CB - cortical bone, M - zone of mineralisation, D - zone of cellular differentiation, Pr - zone of proliferation, P - periosteum.

membranous material that surrounds the bone, is also damaged. This triggers a response from the stem cells in the periosteum which begin to proliferate, with the subsequent increase in tissue volume driving the periosteum away from the cortical bone. In response to signals from growth factors these stem cells begin to differentiate to become osteoblasts, the bone forming cells. As pools of differentiated osteoblasts start to emerge the cells begin to operate to produce the new intramembranous bone. As the new bone is produced it also contributes to the callus growth.

We can further simplify this view and consider the callus region to be split into three separate regions, a proliferative region, a differentiation region and a mineralisation region. By dividing the callus into three distinct regions we can also consider the growth of the callus as the movement of three distinct fronts, the periosteum at the absolute boundary of the callus, a second front between the proliferating cells and the differentiating cells and a third front representing the formation of mineralised bone tissue. We illustrate these regions in Figure 1.3, here we have also assumed a further abstracted fracture geometry. The left side of the picture is the cortical bone and the right edge is the periosteum. At the onset of the fracture healing process the cells in the periosteum begin proliferating driving the periosteum away from the bone surface. Close to the bone surface the stem cells begin to differentiate to become osteoblasts, whilst those near the periosteum are still proliferating. As

the population of osteoblasts becomes established these cells then begin to produce the new bone tissue. The new bone further displaces the differentiating cells, driving the front of differentiation to the right, which further acts to drive the periosteum to the right.

1.2 Aims and Objectives

Currently there are aspects of the cellular and molecular interactions that occur during intramembranous bone formation (and fracture healing in general) that are not particularly well understood. Intramembranous bone formation takes place in areas of high mechanical stability making it ideal for investigating the cellular and molecular processes that are occurring. By building mathematical models that focus on the bio-regulatory mechanisms we aim to improve on the current knowledge of the involvement of growth factors and cells during healing.

Within this thesis we are aiming to build models to investigate bio-regulatory effects on intramembranous bone formation during fracture healing. Specifically we consider secondary healing of a mid-shaft long bone fracture. However we note that the models, or at the very least the insights gained from them, could be applied to other aspects of bone formation.

We focus our attention on two separate processes that must occur in order for intramembranous bone to form. These are the cellular differentiation of stem cells to osteoblasts that can form new bone, and the regulation of new bone formation by osteoblasts. The mathematical modelling of these processes gives rise to two key objectives, these are described below.

Cellular Differentiation The first objective is to develop a model that describes the cellular differentiation that occurs as a precursor to new intramembranous bone being formed. We hypothesise that the structural appearance of new intramembranous bone is a result of a spatially heterogeneous distribution of osteoblast cells, and that this distribution is due to a chemical pre-pattern. We focus the model on describing the relationship between the relevant cells and growth factors known to be present in the callus and implicated in the differentiation process. This model represents the processes that are occurring in the differentiation zone of our simplified view of the callus region.

As a first step to the completion of this objective we build a model for cellular differentiation of stem cells into osteoblasts as driven by a chemical pattern developed due to the interactions of BMP and noggin. The underlying kinetics between BMP and noggin can be reduced to a standard Turing pattern model, which creates an avenue for analysis of the patterning potential of the underlying model.

Having developed the base model, we aim to extend it to a more accurate representation of the callus which includes callus growth as illustrated in Figure 1.3 (however with no explicit inclusion of mineralisation the differentiation zone in effect reaches to the cortical bone surface). Our goal is to investigate the effect that domain growth has on the evolution of pattern in the cell differentiation.

Mineralisation The second objective is to build a model that describes the mineralisation of new bone tissue, a process that takes place in the mineralisation zone of our schematic of the callus. In many models of bone formation, the production of new bone is simply modelled as being proportional to the osteoblast population. We aim to build a model that investigates some additional regulatory effects on the production of new bone tissue. Bone tissue is comprised of a collagen matrix which has been mineralised. We focus building a model that examines the regulation of the mineralisation of the collagen matrix.

In particular the relationship between alkaline phosphatase and pyrophosphate has been identified as being key to the regulation of mineralisation. We build a mathematical model to investigate this relationship and the effect it has on the formation of new bone mineral.

The completion of these key objectives will give rise to two models that describe aspects of intramembranous bone formation. These models are novel mathematical interpretations of the current knowledge of factors affecting fracture healing. Thus it is hoped that these models will contribute to the current knowledge of bioregulatory processes that are occurring during fracture healing.

1.3 Outline of Thesis

In this section we present an outline of the content of the remainder of the thesis.

Chapter 2 – Background Information and Literature Review

Here we provide an overview of the current knowledge of the biology of fracture healing, as well as a review of the current mathematical models that exist for fracture healing. We also review other models for bone formation that are not directly related to fracture healing but still model processes that are similar to that which occurs during fracture repair.

Chapter 3 – A Regulatory Model for Osteoblast Progenitor Differentiation

In this chapter we present a model for the cellular differentiation of stem cells, present in the periosteum, to osteoblasts. We look at the role of two chemical species BMP and noggin in inducing this differentiation. These chemical species act in tandem to produce a chemical pre-pattern that then defines the pattern of cell differentiation seen across the domain. We reduce the relationship between BMP and noggin to a standard Turing pattern model, which allows for analysis of the pattern forming potential of the model. We also present simulations of the full model for both one and two dimensional domains.

Chapter 4 – Cellular Differentiation in a Growing Domain

Here we extend the model for cellular differentiation to more reasonably represent the callus. At first we investigate the effect of more realistic boundary conditions on the ability of our model to produce patterning in the cell species. We then simulate our model on a growing domain, and examine the effect that this has on the cellular differentiation process.

Chapter 5 – A Mathematical Model for the Mineralisation of New Bone Tissue

In this chapter we build a new model for the mineralisation that occurs as new bone forms, that examines the influence of the mineralisation inhibitor pyrophosphate. We begin by examining the relationship between alkaline phosphatase and pyrophosphate, and building a kinetic model

for this relationship. We then extend the model to a one dimensional domain and consider spatial effects. In this model we explicitly model the movement of the mineralisation front, caused by the deposition of new mineral. We then examine the effects of varying parameters on the speed of movement of this front.

Chapter 6 – Summary and Future Directions

We finish the thesis by providing a summary and discussion of the work presented. We also indicate some future directions to further improve upon the models presented in this thesis.

2

Background Information and Literature Review

It is difficult to observe fracture healing as it is occurring in an individual. X-rays and other imaging procedures can be used to view the growth of the callus over time, however observing the behaviour of cells and growth factors is a much more difficult task. Histological slices can be taken and examined but these observations are a 2D slice of a 3D callus taken at a single time point. Thus it can be difficult to observe changes in cell populations or growth factor expression over time and space. Mathematical modelling can be used to gain insights into these processes that are difficult or impossible to observed.

Many mathematical models for fracture healing have been developed. Traditionally these were based on the theory that mechanical forces, related to the stability of the fracture site, was the key regulating factor for successful fracture healing. As more evidence came to light about the role of growth factors in regulating fracture healing, a new series of bio-regulatory models were built. More recently hybrid models which consider both mechanical and biological factors have been developed.

In this chapter we provide a review of the existing models of fracture healing. We also examine some other models of bone formation that are not directly related to fracture healing, as it is likely that similar processes play a role across all types of bone formation. As part of this review we identify the contrasts between our methodology and existing models. We also identify aspects of the existing models that support our methodology.

2.1 Overview of Relevant Biology

We start with an overview of the the relevant biology underlying fracture healing and intramembranous bone formation. Particular attention is paid to the driving factors for the differentiation of stem cells to osteoblasts and the biology of new bone tissue formation. A more detailed description of some of the biology of bone is provided in Appendix A.

2.1.1 Fracture Healing

Classically fracture healing is described as occurring along two pathways, primary or secondary healing. Primary healing can only occur when the fracture gap is very small and stable. Under these circumstances the bone can regenerate through osteonal remodelling without a callus forming. Clinically primary healing is observed when rigid fixation techniques, such as compression plating, are used. The more common form of healing is secondary healing. Here the bone heals with the formation of a callus that bridges the fracture gap (Einhorn 1998, Prendergast & van der Meulen 2001). Both colloquially and in the literature the term fracture healing without specification can be assumed to refer to secondary healing and this practice is followed in this thesis.

Bone fracture healing is typically described as occurring in three phases, the reactive, reparative and remodelling phases. Each phase consists of distinct biological processes, however the timing of these phases may overlap.

The reactive phase is the body's initial response to a fracture. When a fracture occurs the tissue surrounding the bone is also damaged. The reactive phase is mostly the response of the soft tissue to the injury. As with all soft tissue injuries the first response is inflammation, which results in the formation of a haematoma at the fracture site. As part of this inflammation the cells required for healing, including mesenchymal stem cells (MSC)s, accumulate at the fracture site . There are many sources of MSCs but the largest source is believed to be the periosteum, a membrane material that covers the outside of the bone (Gerstenfeld et al. 2003). It is debatable whether the cells of the periosteum are true MSCs or more specialised osteoblast progenitor cells. In this thesis we generally use the term osteoblast progenitor cells to refer to cells specifically from the periosteum whereas we use MSC when talking about the general fracture healing process.

The reparative phase is when the new bone is created. There are two processes of bone formation, intramembranous and endochondral, that occur simultaneously to create a callus surrounding the fracture site. Intramembranous bone formation occurs at the periphery of the callus, in areas of high mechanical stability (Epari et al. 2006). The MSCs differentiate to become osteoblasts, the bone forming cells, which immediately start to form the woven intramembranous bone. Around the fracture gap a endochondral ossification occurs. This region is very mechanically unstable. The MSCs differentiate to become chondrocytes (cartilage cells) which begin to form cartilage. Eventually the cartilage bridges the fracture gap providing an increase in mechanical stability. The cartilage bridge can then be mineralised and turned into bone by osteoblasts. This phase is considered complete when the fracture gap is completely bridged by bone (Prendergast & van der Meulen 2001).

The final phase is remodelling. During this phase the original structure of the bone is restored. The unorganised bone that was created during the reparative phase is resorbed and new lamellar bone is laid down by the osteoblasts. This process is quite gradual and can take up to a year depending on the animal species (Doblaré et al. 2004).

Intramembranous Bone Formation

Intramembranous bone formation occurs during the reparative phase of bone healing. It occurs at the periphery of the fracture callus in areas of high mechanical stability (Schindeler et al. 2008). When the bone is fractured, the periosteum is also damaged. In response to this, MSCs from the periosteum proliferate and push the periosteum further away from the bone. These MSCs then differentiate to become osteoblasts. The osteoblasts are responsible for secreting the collagen and minerals which will form the new bone. The new bone starts to grow as a series of spicules, these eventually become interconnected and give the bone a woven appearance The osteoblasts continue to lay mineralised bone until the pores in the woven bone are filled (Jee 2001).

A study conducted on sheep (Epari et al. 2006) showed that early intramembranous bone formation was the same regardless of the level of external stabilisation that was applied to the fracture. The authors suggested that this indicates that intramembranous bone formation, at least in the early stages of healing, is independent of mechanical conditions. In this study there was

a difference in the amount of bone formation on the lateral and medial sides of the callus. The authors suggested that this disparity was due to a difference in the amount of soft tissue surrounding the bone which affects the biological capacity for healing. However a more recent examination of the same results hypothesises that the difference in bone formation was instead due to the different levels of mechanical stability of either side of the callus which resulted from the method of stabilisation of the fracture gap (Epari et al. 2013). Whilst mechanical factors could be affecting the extent of bone formation that occurs, it is widely assumed in mathematical models of fracture healing that intramembranous bone formation can only occur in regions of high mechanical stability, see for example (Gómez-Benito et al. 2005, Ament & Hofer 2000, Claes & Heigele 1999).

Focussing instead on bioregulatory factors influencing intramembranous bone formation during fracture healing we see that there are several different growth factors and inhibitors believed to affect this process. The bone morphogenetic family of proteins (BMP) is believed to control the differentiation of MSCs into osteoblasts (bone forming cells) or chondrocytes (cartilage cells). BMPs are produced by a wide variety of cell types including MSCs and osteoblasts (Bostrom 1998, Onishi et al. 1998, Spector et al. 2001) In the regions where intramembranous bone formation occurs it appears that BMP 2 and BMP 4 are activating the differentiation of MSCs into osteoblasts (Barnes et al. 1999). The effect of the BMPs is inhibited by several molecules including noggin and gremlin (Tsiridis et al. 2007).

Noggin inhibits BMP by binding with it (Zimmerman et al. 1996), which renders the BMP unable to bind with its receptors on cells. Thus the presence of noggin will reduce the effect of BMP on cell functions. Noggin and BMP have been shown to be present in the same areas of the callus (Yoshimura et al. 2001). Noggin is expressed by cells of an osteoblastic lineage with expression increasing as the cells mature (Abe et al. 2000, Wan et al. 2007). There is also evidence that the presence of BMP augments the expression of noggin by osteoblasts (Gazzerro et al. 1998, Krause et al. 2011). This has led to the belief that the interaction between BMP and noggin plays an important role in regulation of bone formation during fracture healing. More specifically excess noggin has been shown *in vivo* to reduce the amount of intramembranous bone formation in adult rats (Aspenberg et al. 2001).

Once the osteoblasts are present they begin to produce the new bone tissue. This process begins with the production of a collagen matrix. Some of these osteoblasts become embedded in the collagen and differentiate to become osteocytes. The osteocytes and osteoblasts then work in tandem to regulate the deposition of mineral onto the collagen matrix (Franz-Odendaal et al. 2006). This is a complex process that is not well understood.. The new bone mineral is typically described as an impure form of hydroxyapatite ($Ca_5(PO_4)_3(OH)$). Many growth factors and other chemicals present in the interstitial fluid are thought to influence the the production of collagen and its subsequent mineralisation, including members of the BMP family (Cho et al. 2002, Barnes et al. 1999). Other proteins that affect mineralisation include osteopontin, osteonectin and osteocalcin (Hirakawa et al. 1994, Einhorn 1998, Thompson et al. 2002).

One key requirement for the deposition of mineral is removal of mineralisation inhibitor pyrophosphate (PP_i). PP_i is produced as a by-product of cellular respiration and hence is present throughout the body (Fleisch & Bisaz 1962, Russell et al. 1971). Osteoblasts produce a protein alkaline phosphatase (TNAP), which cleaves PP_i. The presence of TNAP and hence the removal of PP_i is known to be critical in allowing mineralisation of new bone tissue to occur (Murshed et al. 2005).

Another factor that affects the mineralisation process is the amount of vascularisation that has occurred. Angiogenisis, the process by which new blood vessels are created, is regulated during fracture healing by vascular-endothelial growth factor (VEGF). VEGF is expressed by osteoblasts, and the rate of expression is stimulated by the presence of BMPs (Tsiridis et al. 2007). The inhibition of VEGF has been shown to slow the process of intramembranous bone formation (Street et al. 2002).

2.2 Existing Mathematical Models for Fracture Healing

There exists many mathematical models for fracture healing. Traditionally these models are mechanoregulatory, that is they are based on the assumption that cell differentiation during fracture healing occurs as a response to mechanical stimulus. More recently, as the effect of growth factors during

fracture healing becomes more clear, new bioregulatory models have been developed where cell differentiation is assumed to be driven by growth factor concentrations. There also exists hybrid models which consider both mechano- and bioregulatory effects.

In the following section we provide a brief review of the existing mathematical models. We acknowledge that there exists a number of review papers on mathematical modelling of fracture healing including, (Geris et al. 2009, Isaksson 2012, Boccaccio et al. 2011), and direct the interested reader towards them.

2.2.1 Mechanoregulatory Models

Mechanoregulatory models assume that fracture healing is driven entirely by mechanical stimuli, such as the stresses and strains placed on the bone or interstitial fluid flow. These models are usually solved computationally using a finite element framework. Generally these models are only solved at discrete time points, i.e. 1 week, 2 weeks, 3 weeks and at a given time point a fracture geometry is assumed. This means that in many of these models the temporal evolution of the callus is unable to be observed.

Pauwels (1980) first proposed that tissue differentiation was stimulated by physical deformation of the MSCs. Pauwels proposed that exposure to shear stress changed the shape of MSCs and caused differentiation into fibroblasts, whereas hydrostatic pressure changed the volume and caused differentiation into chondrocytes. A combination of both sheer and hydrostatic pressure resulted in fibrocartilage. This theory also predicted the need for a stable mechanical environment for bone formation to occur. The concepts of Pauwels theory of tissue differentiation have guided many computational models of fracture healing, some of which are discussed below.

Another early theory proposed for mechanoregulation of tissue differentiation is interfragmentary strain theory (Perren 1979). When a fracture is loaded the fragments displace relative to each other. If the original fracture gap width is L and the gap changes width by ΔL when loading is applied then the longitudinal interfragmentary strain is given by

$$IFS = \frac{\Delta L}{L}. \tag{2.1}$$

Interfragmentary strain theory states that tissue can only be formed in the

fracture gap if that tissue type is capable of withstanding the interfragmentary strain without rupturing. Granulation tissue has the highest strain tolerance followed by cartilage and lowest is bone. Thus if the gap has high interfragmentary strain cartilage cannot form until granulation tissue has formed and stabilised the gap. Similarly bone cannot form until the cartilage has further stabilised the gap.

The first computational models of fracture healing were proposed by Carter et al. (1988). Based on the concepts of Pauwels' theory they proposed that MSC differentiation was decided by the local strain history. Using a finite element model they calculated the load history at each point of the fracture callus. Based on the calculated load history they hypothesised a series of tissue differentiation rules. Using these rules they were able to qualitatively match their results to histological results.

Claes & Heigele (1999) proposed that ossification could only occur along the surface of existing bone and that the magnitude of local stress and strain determined whether intramembranous or endochondral ossification occurred. A finite element analysis was conducted at different stages during the fracture healing process to calculate local stress and strain. By comparing these results to histology from animal fracture models they were able to quantify the levels of stress and strain required for different types of tissue formation to occur.

A different approach which was based on interfragmentary strain theory was used by Gardner et al. (2000). They created a finite element model using geometry from a left tibial fracture in a human patient. They calibrated the model by measuring the forces applied to the leg when the patient was standing and adjusting the model parameters until the force distributions were matched. Using the calibrated model they found the stresses throughout the callus when a walking load was applied. This allowed them to identify regions where callus breakdown was likely to occur due to high levels of stress which the new tissue was unable to withstand.

The previous models discussed were only evaluated at a few discrete time steps. This meant that the temporal evolution of the callus could not be observed. This problem was addressed by Lacroix & Prendergast (2002). They used a series of tissue differentiation rules based on tissue shear strain and interstitial fluid flow as proposed by Prendergast et al. (1997). Using these rules they were able to create a model for fracture healing that was able to track the

temporal evolution of the callus. Given an initial callus size they were able to use their model to predict the resorption of the callus. However one issue with this model is that it does not predict the resorption of the callus within the medullary cavity. A behaviour which is physiologically unrealistic.

An variation of this model was presented in Isaksson et al. (2008). In this model they used the same tissue differentiation rules from Prendergast et al. (1997), however they explicitly modelled the different cell species and their production of new tissue. This model did not include the resorption of the callus so it can not be said whether the inclusion of the differing cell species removed the physiologically unrealistic behaviour observed in Lacroix & Prendergast (2002).

Another model to address temporal evolution was proposed by Ament & Hofer (2000) in the form of a fuzzy logic model. They developed a series of fuzzy rules based on strain energy density, which they calculated from a finite element model. They also tried to incorporate some of the biology of bone healing in the model by assuming that ossification could only occur next to an existing bone surface. They modelled this by including an osteogenic factor, which they defined as the spatial gradient of the amount of bone tissue. Regions where this factor was high were considered to be lying on the surface of existing bone and ossification could occur. Using this model they were able to predict both the growth of the callus during the early stages of healing as well as the resorption of the callus during the later stages.

2.2.2 Bioregulatory Models

For the most part biological effects are ignored in the above models. In particular the effect of growth factors on tissue differentiation has not been addressed. Their is now plenty of research that suggests that growth factors have a large effect on initiating and regulating cell differentiation, migration and proliferation. This has led to the development of a series of bioregulatory models.

Bailón-Plaza & van der Meulen (2001) proposed the first model for fracture healing that had no dependence on mechanical conditions. Instead they created a 2D continuum model based on cell density, extracellular matrix density and growth factor distribution. They considered two generic growth factors, one chondrogenic and the other osteogenic. The chondrogenic growth factor

produced by chondrocytes, with an initial source at the fracture gap. The osteogenic growth factor was produced by osteoblasts, with an initial source along the existing bone removed from the fracture gap. The model was solved on a static 2D domain so was not able to track the growth of the callus over time. This model has been corroborated by Geris et al. (2006) who compared simulated results to experimental results obtained from tibial fractures in mice.

The model has been further extended in different ways. Geris et al. (2008) included the effects of angiogenesis on the healing process. This provided a quantitative improvement on the model by Bailón-Plaza & van der Meulen (2001), by more accurately predicting the fractional amount of different tissue types in the callus.

2.2.3 Hybrid Models

There has also been a series of hybrid models which consider both mechano- and bioregulatory effects. In these models the rates at which biological processes occur, such as cell differentiation or proliferation, is affected by the local mechanical conditions.

An example of this is an extension of the Bailón-Plaza & van der Meulen (2001) model to include mechanical influences on fracture healing (Bailón-Plaza & van der Meulen 2003). In this modified model the authors used a finite element model to calculate the local mechanical strain present in the callus. The parameters of the original model controlling cell differentiation and tissue production were modified to instead become functions of the calculated strain. By doing this the authors were able to observe the effect that different loading conditions had on the formation of new tissue in the callus.

Another hybrid model was presented in Gómez-Benito et al. (2005) which allowed the authors to observe callus growth. They considered the rates of cellular proliferation and differentiation and of tissue production to be regulated by the local stresses and strains as calculated from a finite element model, however they did not include effects of growth factors. They assumed that callus growth occurred due to cell proliferation and hypertrophy of chondrocytes and used these assumptions to incorporate callus growth into the model.

The use of bioregulatory models for fracture healing is a useful tool to gain insights into the effects of growth factors on new bone formation. This is of particular interest as new clinical approaches to treatment of bone non-union have emerged using these growth factors. We note that all of the bioregulatory models focus on the entire callus. This is a complex domain where many differing processes are occurring in different spatial and temporal locations. These models are quite successful at providing an overall view of the development of new tissue in the callus over time. However by focusing on the entire callus they are unable to provide detailed analysis of or insight into the factors controlling specific aspects of fracture healing. We also note that none of the existing bioregulatory models model the growth of the callus over time.

We aim to use a methodology that is in contrast to these existing models. Instead of taking an overall callus view we focus on building models that provide insight into the effect of growth factors and other molecules on specific processes that occur during intramembranous bone formation. We investigate two processes, cellular differentiation and mineralisation.

In the existing bioregulatory models cell differentiation is controlled in response to a single osteogenic or chondrogenic growth factor. We also consider a model where cellular differentiation is controlled by a osteogenic growth factor BMP but we also consider the influence of the BMP inhibitor noggin on the cellular differentiation. Additionally we consider the effect that a growing domain has on the appearance of the differentiation.

We also focus on the processes that regulate new bone tissue formation, specifically the mineralisation. In the existing models bone tissue formation is simply a function of osteoblast cell population. We would like to provide additional insight into the regulatory processes that occur. In particular the effect of the presence of PP_i and TNAP on this process. Mineralisation has also been considered in other bone formation contexts and we review these models in the following section.

2.3 Mathematical Models of Bone Mineralisation

A common approach used in the bioregulatory models of fracture healing described above is to model the rate of formation of new mineralised bone tissue as being proportional to the osteoblast population density. This approach fails

to identify any external regulatory factors that affect the formation and mineralisation of bone. However there does exist other models of bone formation which examine some of these regulating factors.

Several models have been built to examine the behaviour of the bone multicellular unit (BMU) during bone remodelling. In bone remodelling a group of cells referred to as the BMU travels along the bone and replaces the old bone with new bone. At the head of the group are osteoclasts that dissolve the old bone, leaving a hollow channel. Trailing these is a population of osteoblasts, which replace the bone, filling in the channel. This process gives rise to the osteon structure observed in cortical bone. Like the models of fracture healing in these models the rate of bone formation is taken as simply being proportional to the osteoblast cell density (Ryser et al. 2009, Pivonka et al. 2008). In more recent models this has been taken a step further and geometric considerations have been taken into account with the rate of bone formation decreasing as the radius of the channel decreases (Buenzli et al. 2011).

Other models that deal with bone formation include those built for the osseointegration of implants into bone. In this case the new bone forms intramembranously and similarities can be drawn between the bone formed surrounding the implants and the woven bone observable in fracture healing (Davies 2003). In one of these models (Moreo et al. 2009) they model tissue formation using volume fractions and consider the new bone formation to be proportional to the number of osteoblasts as well as dependent on two unspecified growth factors.

A more interesting approach to modelling implant osseointegration was presented in Prokharau et al. (2012). They considered the domain to consist of two separate regions, one filled with bone tissue the other soft tissue, and explicitly model the boundary between the two using the level set method. As new bone is deposited onto the existing bone the region of bone tissue grows. However, like many of the other models discussed, they model new bone deposition as proportional to the osteoblast cell density with no other regulatory factors considered. Another interesting aspect of this model is that it models the degree of cellular maturity as an extra dimension of the model, with only fully mature osteoblasts capable of producing new bone. In this article the authors only solved the system on a 1D domain, however the inclusion of an extra dimension for cellular maturity could introduce complexities

in the numerics when solving the system in a 2D or 3D domain. This is in addition to the increased complexity of implementing the level set method in higher dimensions.

Another differing model for bone formation is presented in Carlier et al. (2011), where they give a model for bone formation on a calcium-phosphate scaffold. Using a reduced version of the bioregulatory model of Geris et al. (2008) as a starting point they also included the effect of calcium concentration on mineral deposition. In this model they only considered the temporal changes in the modelled species, however the authors indicate that this is an area under future investigation.

Whilst none of these models are explicitly related to intramembranous bone formation during fracture healing there are concepts and ideas that can be applied to this context. In particular the modelling of the mineralisation front explicitly as in (Prokharau et al. 2012) and the dependence of new mineral formation on mineral concentration as in (Carlier et al. 2011) are ideas that warrant further investigation. We also note that none of these models investigate the effect of the regulatory loop between TNAP and PP_i on mineralisation.

2.4 Turing Patterns in Models of Bone Growth

During intramembranous bone formation there appears to be some pattern in the structure of the newly formed bone. As indicated in the literature (Tsiridis et al. 2007, Barnes et al. 1999) intramembranous bone formation during fracture healing is influenced by growth factor concentrations. It is therefore possible that the patterning apparent in new intramembranous bone is due to an underlying chemical pre-pattern

The emergence of pattern or form in an organism is termed morphogenesis. The earliest attempt at providing a mathematical description of morphogenesis was done by Turing (1952) in his seminal paper 'The chemical basis of morphogenesis'. Turing proposed that morphogenesis was the result of cells responding to chemical stimuli. These chemical species, termed morphogens, were free to diffuse and react across the domain. When there are 2 or more morphogens, a variety of behaviours can arise. Of most interest in morphogenesis is the evolution of a stable spatial pattern from an (almost) spatially homogeneous initial state. Turing described the conditions under which this

and other states would arise. One essential element that was identified by Turing was that for stable patterns to evolve the interacting morphogens must both be diffusing at different rates. The idea that diffusion is required for spatial patterning to occur is counter intuitive as diffusion is usually seen as a smoothing process.

Turing patterns are well studied and have been used for many different applications. Analysis has been conducted on standard Turing patterns and many variations on this type of model. Some of these variations include the effect of spatially nonuniform parameters (Maini et al. 1992, Page et al. 2003) and the evolution of pattern on a growing domain (Crampin et al. 2002). Additionally this Turing models have been used to model many different biological phenomena. Perhaps the most famous example is of modelling animal coat patterns, here Turing models have been able to reproduce patterns that resemble the stripes on a tiger or the spots on a leopard (Koch & Meinhardt 1994, Murray 2003). Other well studied examples include stripe formation in zebrafish (Kondo & Asai 1995) and the regular spatial distribution of feather buds in a developing chick (Jung et al. 1998).

Whilst it is easy to write down a model of pattern formation, and for this to qualitatively match expected patterns in biology it is much harder to experimentally verify that the pattern is indeed due to the mechanism described by Turing. The complexity of biological systems means that morphogens are difficult to identify and measure. There are also other mechanisms by which morphogenesis can occur and it can be difficult to distinguish which mechanism gave rise to the observed structure.

An exciting, recent breakthrough in this area was made by Economou et al. (2012). They were able to demonstrate that in a developing mice embryo the patterning of the rugal (the ridges on the top of the mouth) matched that predicted by a Turing model, and importantly could not have been explained by any other known pattern formation process.

2.4.1 Local Self Enhancement, Long Range Inhibition

Following on from Turing's work, two other important properties were identified as required for the evolution of a temporally stable spatial pattern. Gierer & Meinhardt (1972) and independently Segel & Jackson (1972) both demonstrated that for stable spatial patterns to evolve there must be local self

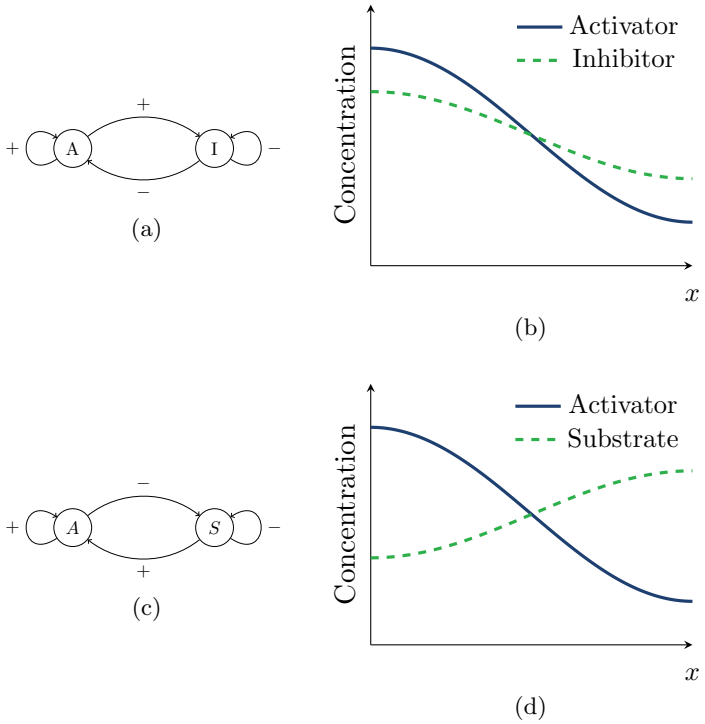

Figure 2.1: Schematic diagrams and typical solutions for activator-inhibitor and activator-substrate systems. (a), (b) are for an activator-inhibitor system where the self-activating A also activates the production of the inhibitor I. (a) Shows a schematic of this behaviour and (b) the qualitative behaviour of the solution for an activator-inhibitor system. (c),(d) are for a activator-substrate system where the self - activating A consumes the substrate S.

enhancement and long range inhibition. Local self enhancement means that any small perturbations in the concentration of an activator are amplified. In the absence of an inhibitory substance then this amplification would spread across the entire domain. For patterns to arise a fast diffusing antagonist must exist. This antagonist acts over a much wider range then the activator and whilst it is not strong enough to suppress the original spike it will suppress any activator spikes from evolving in the neighbourhood of the original spike.

In a two species system there are two ways that local self activation and long range inhibition can occur. An activator-inhibitor system or an activator-substrate system. These systems have differing underlying mechanisms and have qualitatively different results. Figure 2.1 provides an illustration of the different systems along with an example of their qualitative results.

In what is classically known as an activator-inhibitor system the activator self activates and induces the production of the inhibitor. The inhibitor however inhibits the production of the activator. Patterns evolve because an area of high activator concentration induces a high production of inhibitor. The inhibitor acts over a wider range than the activator and hence suppresses activator production in the local neighbourhood of the region of high activator. In these systems we see patterns arise where the activator and inhibitor are in phase with one another.

Long range inhibition can be achieved in another fashion typically described as a activator-substrate or positive-feedback system. Here rather then inhibiting the activator, the "inhibitor" is a substrate that is required for the production of the activator. As the activator is produced the substrate is consumed. The inhibition exists because as the amount of substrate available decreases so does the rate at which new activator can be formed. In these systems the resultant patterns have the activator and substrate 180° out of phase.

2.4.2 Use of Turing Patterns for Bone Growth Modelling

Recently Turing models have been developed for different aspects of bone growth. Whilst none of these models focus on intramembranous bone formation, they do provide some evidence that Turing models can be used to describe some of the patterns that arise during bone growth.

Courtin et al. (1995) created a Turing instability type model for bone mineral metabolism based on a previously derived compartment model for calcium metabolism (Staub et al. 1988). This original compartment model was developed to capture the cyclical circadian nature of calcium concentration in the blood plasma. Two of the components accounted for this cyclic behaviour and a new reduced system consisting of just these two species was created. This reduced system is given in non-dimensional form by

$$\frac{\partial Y}{\partial t} = \nabla^2 Y + \gamma\big((k + Y^2)X - (1 + k_2)Y\big), \tag{2.2}$$

$$\frac{\partial X}{\partial t} = D\nabla^2 X + \gamma\big(A - (k_1 + k + Y^2)X + k_2 Y\big). \tag{2.3}$$

The variables X and Y are proposed by the authors to represent diffusible mineral precursors amalgams of calcium and phosphate. The parameters A, k, k_1 and k_2 are all positive rate constants which were determined as part of the

original compartment model. The parameter $D > 1$ represents the ratio of the diffusion coefficients of X and Y.

For suitably large values of D, the resultant stable patterns are similar to those exhibited by other Turing pattern forming systems. As D increases the patterns formed transform from hexagonal to striped and return to an inverse hexagonal pattern.

One interesting aspect of the model is that for the given parameters, in the absence of diffusion the kinetics do not give rise to a stable steady state. Instead the steady sate is unstable and is surrounded by an associated stable limit cycle. This limit cycle means that for small (or no) diffusion coefficients the behaviour will be a temporally oscillating spatially homogeneous steady state. As D increases the behaviour in the solutions transitions from the temporally oscillating yet spatially homogeneous to become temporally steady and spatially heterogeneous. In this transition zone the numerical solutions exhibited complex spatio-temporal behaviour. When this behaviour was plotted in 3D by including time as the third dimension the results resembled the structure of new woven bone as shown in Figure 2.2. This complex behaviour was further explored by the authors in a later paper (Courtin et al. 1997). Here the authors used a circular domain, which gave a cylindrical 3D image in order to more accurately represent a growing embryonic long bone.

Within the context of bone formation, the paper interprets X and Y as precrystalline calcium-phosphate associations. These associations are free to diffuse throughout the bone extracellular fluid where calcium and phosphate is super saturated. However a more detailed physical interpretation of these species is lacking. The link between the patterning in these species and the resultant bone pattern is hypothesised to be that the difference in chemical species could result in differences in the rates at which mineral is deposited. They propose that this effect could either be a direct or indirect response to the concentration levels, as it is known that cell species respond to the levels of ionic species.

A different use for Turing models was to identify the location of secondary ossification centres (Garzón-Alvarado et al. 2009*b*). This is a process that occurs during developmental bone growth. When endochondral ossification occurs in a new bone it starts in the middle of the shaft and advances towards the heads. Postnatally as this ossification front approaches the head

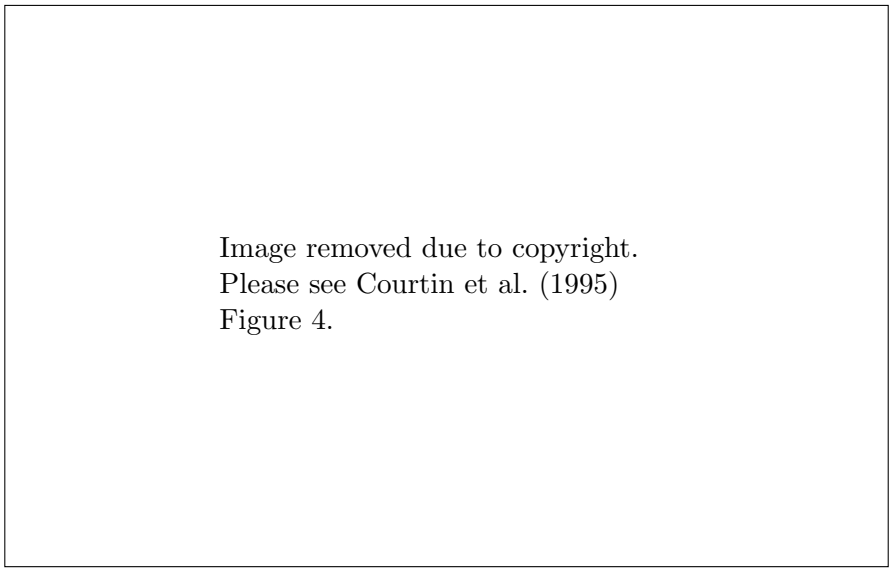

Figure 2.2: 3D plot of complex spatio-temporal behaviour. Here time is used as the third dimension and the 2D images found are combined to form a structure that resembles woven bone (Courtin et al. 1995).

a secondary ossification centre is formed in the head. The authors modelled this by considering cell differentiation of chondrocytes to be driven due to the concentrations of parathyroid hormone-related peptide (PTHrP) and Indian hedgehog (Ihh). They used Schnackenberg kinetics to model the relationship between PTHrP and Ihh. This model was able to identify regions where secondary ossification was likely to occur for different animals based on bone head shape.

A similar model from the same authors was used to model long bone growth (Garzón-Alvarado et al. 2009*a*). This model had more complicated cellular dynamics but the underlying reaction kinetics of PTHrH and Ihh were the same. This model was used to simulate the growth of a long bone during fetal development, due to endochondral ossification. Due to the similarities between these models and the next model to be discussed (Garzón-Alvarado 2013) we provide only a detailed review of the next model as it specifically relates to intramembranous bone formation.

Another model proposed by Garzón-Alvarado (2013) is for the formation of primary ossification centres in the membranous neurocranium (part of the embryonic skull). The primary ossification centres are where the first sites of ossification occur during the embryonic development of what will become the

flat bones of the skull. These flat bones form via intramembranous ossification. The authors identify BMP-2 and noggin as the key regulators of the differentiation of MSCs to osteoblasts. Based on this they propose a model for the differentiation of osteoblasts as a process regulated by BMP concentrations, where BMP is itself regulated by its interactions with noggin.

The model used in the paper is described below. They assume that BMP and noggin have a relationship capable of producing Turing patterns and hence model their interactions using the well known Schnackenberg kinetics. Little justification is provided for this choice of kinetics. Additionally Schnackenberg kinetics are of the type activator-substrate, which seems at odds with the descriptions of BMP-noggin interactions found in the biological literature. The equations for BMP and noggin are given by

$$\frac{\partial S_B}{\partial t} = C(\alpha_1 - \mu S_B + \gamma_0 S_B^2 S_N) + D_B \nabla^2 S_B, \tag{2.4}$$

$$\frac{\partial S_N}{\partial t} = C(\alpha_2 - \gamma_0 S_B^2 S_N) + D_N \nabla^2 S_N, \tag{2.5}$$

Here S_B and S_N are the concentrations of BMP and noggin respectively, C is a constant representing the concentration of MSCs, $\alpha_1, \alpha_2, \mu, \gamma_0$ are positive rate constants and D_B and D_N are the diffusion coefficients for BMP and noggin.

The paper also provides an equation for the change in osteoblast concentration due to cellular differentiation. However no simulation results or discussion is provided for this equation, nor are any parameters provided. The model assumes that cell differentiation is dependent on both the BMP concentration and the maturity of cells, with only the more mature cells able to differentiate. The cell maturation is implemented in the model as a spatial effect, with cells closer to boundary of the domain representing the Rostral crest assumed to be more mature then cells further away. This equation for the cells is given by

$$\frac{\partial c_0}{\partial t} = \eta \frac{S_B^n}{S_B^n + S_T^n} \frac{T_a^r}{T_a^r + t^r} f(x_{\text{rel}}), \tag{2.6}$$

where c_0 is the cell concentration of osteoblasts, η is a rate constant, S_T is a threshold value for BMP, T_a is the time required to perform the differentiation and t^r is the time limit of action of the BMP-2.The function $f(x_{\text{rel}})$ is used to define the cell maturation as a function of the distance of a point to the

boundary of the domain, labelled x_{rel}. It is defined as

$$f(x_{rel}) = \begin{cases} 1 & x_{\text{rel}} \leq r, \\ 0 & x_{\text{rel}} > r. \end{cases} \tag{2.7}$$

The equations for BMP and noggin are simulated on the surface of a partial curved ellipsoidal shape, with the spatial dimensions determined from experimental measurements. Several questions arise from the parameters used in these simulations. Firstly, the parameters reported as being used in the simulations for D_B and D_N are incapable of giving Turing patterns. Some of the parameters for the model were able to be determined from sources in the literature, however, like in many other mathematical models of biological phenomenon, this was not possible for all parameters. In this case the authors chose their parameters such that suitable patterns emerged. A consequence of this is that the pattern forming process has a characteristic time of 65 weeks. Clearly this value is unrealistic given that the biological process examined here is the development of the embryonic skull.

Our approach to building a model for the cellular differentiation bears some resemblance to the model presented in Garzón-Alvarado (2013), however there are some key differences between the models which address some of the aforementioned problems with the model in Garzón-Alvarado (2013). Firstly there is a difference in the kinetics used in the two models. In our model we build the kinetics based on the behaviour of the cells and growth factors described in the literature, as opposed to Garzón-Alvarado (2013) where the kinetics used did not seem appropriate given the biological context. Another feature of our work presented in this document is that we consider the effect of a growing domain on the pattern forming ability of the model. This is important as during the early stages of fracture healing, the callus grows larger and it is possible that this callus growth is influencing the pattern formation that occurs.

2.5 Summary

There is strong evidence that intramembranous bone formation is influenced by bioregulatory factors such as growth factor concentration. Despite this most traditional models of fracture healing tend to focus on healing as driven

by mechanical factors. There does exist some bioregulatory models of fracture healing. These models are phenomenological and act on the entire callus scale. As such they do not provide much insight into specific processes that are occurring during intramembranous bone formation or how these processes give rise to the structure of the new bone that is observed.

Instead we take the approach of building mathematical models that aim to provide a more mechanistic understanding of specific processes that occur during intramembranous bone formation. We focus of two processes, cellular differentiation and mineralisation of new bone tissue. The differentiation of stem cells to osteoblasts is controlled by the presence of various growth factors, which can either increase or decrease the differentiation rate. These growth factors establish a chemical pre-pattern which then drives the cellular differentiation

Turing like models have had some success when applied to other aspects of bone growth and healing. We propose that a Turing like model can be used to establish a chemical pre-pattern which then drives the cellular differentiation and mineralisation processes. This will be the basis of a new model for cellular differentiation as it occurs during intramembranous bone formation in fracture healing.

We also aim to build a model for mineralisation of new bone tissue. Typically models of fracture healing consider the production of bone matrix to simply be a function of the osteoblast population, with no regulation by other growth factors or molecules. We have identified a regulatory effect of PP_i and TNAP on bone mineralisation that is well established in the literature. However this regulatory effect has not yet been applied to a mathematical model of new bone formation in any context. Thus we aim to build a model that investigates this effect.

3

A Regulatory Model for Osteoblast Progenitor Differentiation

One of the first processes that must occur during the intramembranous bone formation component of fracture healing is the differentiation of osteoblast progenitors, present in the expanded periosteum, into mature osteoblasts that can create mineralised bone. Many existing mathematical models of fracture healing propose that this differentiation is regulated by the amount of mechanical stress or strain that is experienced by the cells (see for example Lacroix & Prendergast (2002) or Claes & Heigele (1999)) or as a response to a single chemical species present in the tissue, in and around the fracture site (Bailón-Plaza & van der Meulen 2001, Geris et al. 2006). These models all focus on the entire fracture callus and demonstrate varying levels of success at predicting regions in which intramembranous bone formation will occur.

Within the context of intramembranous bone formation we are particularly interested in the semi-regular pattern that often appears in the newly formed bone. None of the classical models of fracture healing provide any insight into how the structure of new intramembranous bone arises. As a first approach to constructing a model to reproduce this structure we present here a model that gives rise to a non-uniform distribution of osteoblasts. Whilst not demonstrated explicitly in this chapter it is expected that regions where a high concentration of osteoblasts exist will become focal points for new bone formation. The expectation is then that as time evolves this non-uniform distribution of nodes of bone formation will give rise to the structure observed in new intramembranous bone.

In our model we take the approach of considering the differentiation of the osteoblast progenitors to osteoblasts to be driven by two interacting chemical

species, bone morphogenetic protein (BMP) known to promote cellular differentiation and its inhibitor, noggin. This approach is similar to that presented in Garzón-Alvarado (2013), however there is a key difference in the underlying reaction diffusion relationship between BMP and noggin. In their paper Garzón-Alvarado (2013) assume that BMP and noggin have an activator-substrate type of relationship and use the well studied Schnackenberg kinetics to describe this. The use of these kinetics seems a poor choice when compared to the current understanding of the interactions of BMP and noggin described in the biological literature (see (Krause et al. 2011) for example). Furthermore the authors do not provide any reasoning for the biological relevance of the chosen kinetics. In contrast as we build a model in which all of the terms are biologically relevant. This leads to a system where the underlying relationship between BMP and noggin is of the activator-inhibitor type.

3.1 The Role of BMP and Noggin in Inducing Cellular Differentiation

During fracture healing most intramembranous bone is formed in regions of high mechanical stability, directly between the periosteum and the existing bone. The progenitor cells present in the periosteum proliferate and differentiate to become mature osteoblasts capable of producing bone tissue. Members of the BMP family have been shown to induce this differentiation.

Much research has been conducted on the role of BMP in regulating this differentiation process. BMPs were first identified for the role they play in inducing new bone formation (Urist 1965, Wozney et al. 1988) but it has since been shown that they play a role in the development and function of other organs in the body (Chen et al. 2004). Of the many different BMPs only some induce differentiation of cells to osteoblasts. BMPs 2, 4, 6 and 9 have been shown to have the strongest effect on inducing osteoblastic differentiation (Cheng et al. 2003). However of these only BMP 2 and 4 are located within intramembranous bone (Krause et al. 2011). Also of importance is that both BMP 2 and 4 have been shown to have a short range of activity (Jones et al. 1996, Ohkawara et al. 2002).

BMP 2 and 4 have both been shown to be expressed during fracture healing by cells across the osteoblastic linage, from periosteum derived osteoblast

precursors, to mature matrix producing osteoblasts (Bostrom 1998, Onishi et al. 1998, Spector et al. 2001). Additionally BMPs are also found within the extracellular matrix of bone tissue (Yang et al. 1990). It is believed that when the bone is damaged during fracture healing BMPs are released, subsequently initiating the response of the cells present in the periosteum (Barnes et al. 1999, Tsiridis et al. 2007).

Like all biological signalling systems, many other proteins can influence the effect that BMPs have on cellular differentiation. Some proteins like Sonic Hedgehog (SHH) have a positive effect on BMP signalling (Warzecha et al. 2013), whereas others can inhibit its signalling ability. These BMP inhibitors can interfere with the signalling on several levels. At the extracellular level, proteins like noggin, gremlin and chordin can all bind with BMP molecules preventing them from interacting with cell receptors (Zimmerman et al. 1996, Hsu et al. 1998, Piccolo et al. 1996). At a receptor level, BMP is inhibited by BAMBI (BMP and activin membrane bound inhibitor). BAMBI is a pseudoreceptor located on the cell membrane. To BMPs located in the extracellular space it appears as a normal cell receptor, however it lacks any intracellular component so the BMP signalling pathway is interrupted (Onichtchouk et al. 1999). Finally BMP can also be inhibited at an intracellular level. These intracellular proteins interfere with the signalling pathway within the cell and includes some smads and Smurf (smad ubiquitin regulatory factor) (Dimitriou et al. 2006, Balemans & Hul 2002).

The BMP inhibitor noggin has been shown to reduce intramembranous bone formation (Aspenberg et al. 2001, Krause et al. 2011). Noggin was first discovered in the frog species *xenopus* and is so named because embryos in which excess noggin synthesis was induced developed large heads (Smith & Harland 1992). Noggin is an extracellular inhibitor and it inhibits BMP by binding with it, preventing the BMP from binding with receptors on the cell (Zimmerman et al. 1996). By doing this, noggin reduces the effect of BMP present in the system. In osteoblasts, noggin production is induced by BMP (Gazzerro et al. 1998). This natural feedback loop, where BMP induces noggin which reduces the amount of BMP, is believed to be an important regulatory mechanism for bone growth. There is histological evidence that BMP and noggin are colocalised during fracture healing (Yoshimura et al. 2001). Additionally noggin has been shown to have a long spatial range of inhibition

(Jones & Smith 1998).

The above description provides good evidence that the interactions between BMP and noggin could be modelled using a activator-inhibitor type of reaction kinetics. Here BMP induces the production of noggin by osteoblasts but the presence of noggin reduces the amount of BMP expressed by the osteoblasts. We also note that a key requirement for Turing pattern formation, as described in the preceding chapter, the presence of a long range inhibitor and a short range activator, is met by both BMP and noggin (Jones & Smith 1998, Jones et al. 1996, Ohkawara et al. 2002)

3.2 Model Formation

We illustrate the previous description of the roles of BMP and noggin on the regulation of cellular differentiation as a schematic in Figure 3.1. Here we consider four key components of the cellular differentiation process, two cell species defined as progenitor cells and osteoblasts and the two proteins BMP and noggin. At this point it should be mentioned that cellular differentiation is not a discrete process, that is, a cell is not one type in one moment and a different type the next. Instead the classification of different cell types is murky, and there is no set definition for the boundaries for where one cell stage ends and another begins. In our model we consider the cellular populations as distinct, as is done in other models of fracture healing (Bailón-Plaza & van der Meulen 2003, Geris et al. 2006). In our classification of relevant cell types we use the terms progenitor cells and osteoblasts to distinguish the cell populations. The term progenitor refers to cells derived from the periosteum. These cells are free to proliferate and are not expressing any of the markers of osteoblastic differentiation such as alkaline phosphatase (ALP). The cells referred to as osteoblasts in this model could perhaps be better described as pre-osteoblasts, at the very least they are not fully mature osteoblasts. These are cells that are showing signs of osteoblastic differentiation such as increased expression of ALP, however they are not producing mineralised matrix.

The key feature of the coupled cell and regulatory process to be considered here is that the progenitor cells differentiate to become osteoblasts, where the rate of differentiation is increased by the presence of BMP and reduced by the presence of noggin. We embed this feature into a mathematical model con-

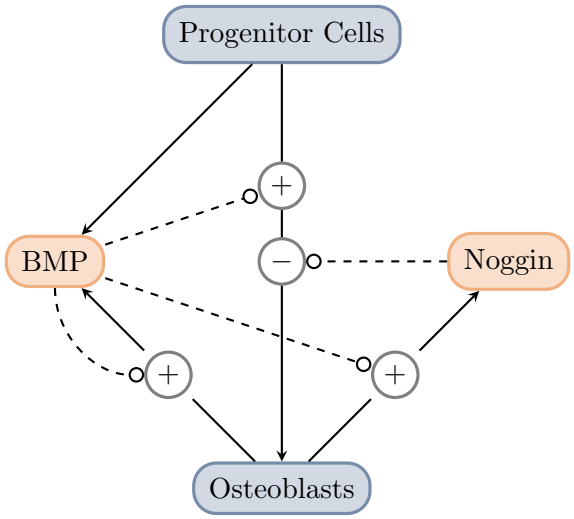

Figure 3.1: Schematic of the regulation of progenitor cell differentiation to osteoblasts by BMP and noggin. Solid lines represent a transformation, or production, dashed lines represent a regulatory effect on the rate of transformation or production. Differentiation of progenitor cells to osteoblasts increases (+) in the presence of BMP and is reduced (−) in the presence of noggin. BMP is produced by both progenitors and osteoblasts, and has an autocatalytic effect on its production by the latter. Noggin is produced by osteoblasts and the production rate is upregulated by the presence of BMP.

structed as a system of partial differential equations describing the interaction and dispersion of progenitor cells ($P(\mathbf{x},t)$), osteoblast cells ($O(\mathbf{x},t)$), BMP 2 or BMP 4 ($B(\mathbf{x},t)$) and noggin ($N(\mathbf{x},t)$).

The proliferation of the progenitor cell population is modelled as a logistic growth behaviour. Both progenitors and osteoblasts influence the proliferation rate and as cell numbers increase the rate of proliferation decreases. The progenitor cells differentiate to become osteoblasts, the rate at which this occurs is increased in the presence of BMP and decreased in the presence of noggin (see Figure 3.1). We note that we do not consider the effect of the limited lifespan of the progenitor cells as in humans the average lifespan of progenitor cells is much greater than the time span observed in our simulations (Stenderup et al. 2003). From this we write the following equation for the rate of change of the progenitor cells,

$$\frac{\partial P}{\partial t} = \lambda_1 P(1 - \lambda_2 P - \lambda_3 O) - \frac{\zeta BP}{\epsilon + N} + D_P \nabla^2 P, \tag{3.1}$$

where all of the parameters $\lambda_1, \lambda_2, \lambda_3, \zeta, \epsilon$ and D_P are assumed to be positive and constant. We can introduce new parameters, $\xi = \lambda_1/\lambda_2$ which represents

the intrinsic growth rate of the progenitor cell population, and $P_c = 1/\lambda_2$ which represents the carrying capacity. We then rewrite the equation as

$$\frac{\partial P}{\partial t} = \xi P\left(P_c - P - \frac{\lambda_3}{\lambda_2}O\right) - \frac{\zeta BP}{\epsilon + N} + D_P\nabla^2 P. \tag{3.2}$$

We assume that all progenitor cells are the same size and similarly that all osteoblasts are that same size, meaning that we can equally think of the carrying capacity as a number or density. We then make the further assumption that osteoblasts and progenitor cells are of the same size as each other, which implies that $\lambda_3 \approx \lambda_2$ and our equation reduces to

$$\frac{\partial P}{\partial t} = \xi P(P_c - P - O) - \frac{\zeta BP}{\epsilon + N} + D_P\nabla^2 P. \tag{3.3}$$

The constant ζ is the rate of progenitor cell differentiation enhanced by the concentration of BMP present and diminished by the concentration of noggin. The parameter ϵ may be interpreted as a measure of the sensitivity of the retardation of the differentiation process to the presence of noggin. We choose to model the dispersion of the progenitor cell population as a Fickian diffusion process as a first approximation, recognising that directed migration processes such as chemotaxis may also play a role here.

The osteoblast population is assumed to only increase due to the differentiation of the progenitor cells. This assumption is made based on the fact that the proliferation rate of mature osteoblasts is very slow compared to the time scale of days which is the time scale of interest (Jee 2001). The death of osteoblasts is modelled as a simple exponential decay, again as a first approximation. This results in the following equation for the rate of change of the osteoblasts,

$$\frac{\partial O}{\partial t} = -\delta O + \frac{\zeta BP}{\epsilon + N} + D_O\nabla^2 O, \tag{3.4}$$

where the constant δ is the death rate and the central term on the right hand side represents the differentiation of progenitor cells to osteoblasts as described previously. As with the progenitor cells we model cell movement as a Fickian diffusion process, with diffusion coefficient D_O, as a first approximation. Although osteoblasts are generally considered to remain stationary after differentiation has occurred, we include a diffusion term in order to increase the stability of our numerical scheme.

We now turn our attention to the modelling of the two chemical species, BMP and noggin. BMP is produced by both osteoblasts and progenitor cells. It

is assumed that there is a constant rate of production by the progenitor cells but that the rate of production by osteoblasts is increased in the presence of BMP (Chen et al. 1997), and decreased in the presence of noggin (Gazzerro et al. 1998). Additionally we assume a constant rate of decay for BMP. We write the equation for BMP as

$$\frac{\partial B}{\partial t} = \alpha P + \frac{\beta B^2 O}{\sigma + N} - \rho B + D_B \nabla^2 B. \tag{3.5}$$

Here the constant α represents the production rate of BMP by the progenitor cells and the constant β is the rate of production of BMP by osteoblasts enhanced by the concentration of BMP present and reduced by the concentration of noggin. As is the case for ϵ, the parameter σ can be interpreted as a measure of the sensitivity of the inhibition of BMP production by the presence of noggin. The parameter ρ is the decay rate for BMP. BMPs are considered diffusible within the extracellular space (Umulis et al. 2009) and we model this as Fickian diffusion with diffusion coefficient D_B.

We assume that the BMP inhibitor noggin is produced only by osteoblasts and this rate of production is increased by the presence of BMP (Gazzerro et al. 1998). We also assume a constant rate of decay for noggin. We write the final equation for our model as

$$\frac{\partial N}{\partial t} = \eta B^2 O - \mu N + D_N \nabla^2 N, \tag{3.6}$$

where η is the rate of production of noggin by the osteoblasts enhanced by the presence of BMP and μ is the constant decay rate of noggin. Like BMP, noggin is diffusible in the extracellular space which we model as Fickian diffusion with diffusion coefficient D_N.

Equations (3.3)-(3.6) represent our full system of equations for our model cellular differentiation. We rewrite the full system of equations here for completeness,

$$\frac{\partial P}{\partial t} = \xi(P(P_c - P - O)) - \frac{\zeta B P}{\epsilon + N} + D_P \nabla^2 P, \tag{3.7}$$

$$\frac{\partial O}{\partial t} = -\delta O + \frac{\zeta B P}{\epsilon + N} + D_O \nabla^2 O, \tag{3.8}$$

$$\frac{\partial B}{\partial t} = \alpha P + \frac{\beta B^2 O}{\sigma + N} - \rho B + D_B \nabla^2 B, \tag{3.9}$$

$$\frac{\partial N}{\partial t} = \eta B^2 O - \mu N + D_N \nabla^2 N. \tag{3.10}$$

With initial conditions

$$P(\mathbf{x},0) = P_0(\mathbf{x}), \qquad O(\mathbf{x},0) = O_0(\mathbf{x}), \tag{3.11}$$

$$B(\mathbf{x},0) = B_0(\mathbf{x}), \qquad N(\mathbf{x},0) = N_0(\mathbf{x}), \tag{3.12}$$

and appropriate boundary conditions, to be specified later.

As we are considering cellular differentiation as a precursor to intramembranous bone formation during fracture healing the domain of interest is only a fraction of the entire fracture callus. To determine the appropriate temporal and spatial domains for our simulations we used the temporal progression and geometry of a callus that develops following an ovine (sheep) osteotomy (Manjubala et al. 2009). Within 2 weeks postoperatively new intramembranous bone has formed. For this new bone to form the progenitor cells must differentiate to become osteoblasts, and then the osteoblasts can create the new bone by first producing a collagen matrix and then proceeding to mineralise this matrix. The production of a mineralised matrix is not a quick process and thus it is reasonable to assume that the cellular differentiation is occurring quickly to allow the other processes to occur. Because of this we used a time domain of 5 days, and at the completion of this time period we expect to see a patterning in the cell species. For the chemical concentrations we expect to see the patterning evolve in an even shorter time frame as the chemical pre-pattern must be first established before patterning can be observed in the cell populations. For the spatial domain we use a domain that measures 2 mm in length for the 1D simulations and is 2 mm $\times$ 2 mm for the 2D simulations. This domain size was determined from the geometry of a sheep's fracture callus and represents a portion of the callus where intramembranous bone formation is taking place.

For the initial series of simulations in this chapter, the initial conditions used for the cell species are a homogeneous distribution of cells across the domain,

$$P(\mathbf{x},0) = P_0, \qquad O(\mathbf{x},0) = O_0. \tag{3.13}$$

The initial conditions for the chemical species are then set to their steady state values, which correspond to the initial cell density. However to initiate pattern formation a small amount of additive white Gaussian noise is added to the concentration for BMP,

$$B(\mathbf{x},0) = B_0 + \text{noise}, \qquad N(\mathbf{x},0) = N_0. \tag{3.14}$$

In this chapter we use zero-flux boundary conditions for all species as a starting point for analysis of the model. In Chapter 4 we incorporate more physically realistic boundary conditions.

3.2.1 Non-Dimensionalisation

To non-dimensionalise the system we introduce dimensionless variables

$$\bar{P} = \frac{P}{\hat{P}}, \quad \bar{O} = \frac{O}{\hat{O}}, \quad \bar{B} = \frac{B}{\hat{B}}, \quad \bar{N} = \frac{N}{\hat{N}}, \quad \bar{t} = \frac{t}{\hat{t}}, \quad \bar{x} = \frac{x}{\hat{x}}, \tag{3.15}$$

where the hatted values, $\hat{P}, \hat{O}$ etc., are to be determined. We substitute these variables to give,

$$\frac{\partial \bar{P}}{\partial \bar{t}} = \left(\xi \hat{t} \hat{P}\right) \bar{P} \left(\left(\frac{P_c}{\hat{P}} \right) - \bar{P} - \frac{\hat{O}}{\hat{P}} \bar{O} \right) - \left(\frac{\zeta \hat{t} \hat{B}}{\hat{N}} \right) \frac{\bar{B}\bar{P}}{\left(\frac{\epsilon}{\hat{N}}\right) + \bar{N}} + \left(\frac{D_P \hat{t}}{\hat{x}^2} \right) \frac{\partial^2 \bar{P}}{\partial \bar{x}^2}, \tag{3.16}$$

$$\frac{\partial \bar{O}}{\partial \bar{t}} = -\left(\delta \hat{t}\right) \bar{O} + \left(\frac{\zeta \hat{B} \hat{P} \hat{t}}{\hat{O} \hat{N}} \right) \frac{\bar{B}\bar{P}}{\left(\frac{\epsilon}{\hat{N}}\right) + \bar{N}} + \left(\frac{D_O \hat{t}}{\hat{x}^2} \right) \frac{\partial^2 \bar{O}}{\partial \bar{x}^2}, \tag{3.17}$$

$$\frac{\partial \bar{B}}{\partial \bar{t}} = \left(\frac{\alpha \hat{P} \hat{t}}{\hat{B}} \right) \bar{P} + \left(\frac{\beta \hat{B} \hat{O} \hat{t}}{\hat{N}} \right) \frac{\bar{B}^2 \bar{O}}{\left(\frac{\sigma}{\hat{N}}\right) + \bar{N}} - \left(\rho \hat{t}\right) \bar{B} + \left(\frac{D_B \hat{t}}{\hat{x}^2} \right) \frac{\partial^2 \bar{B}}{\partial \bar{x}^2}, \tag{3.18}$$

$$\frac{\partial \bar{N}}{\partial \bar{t}} = \left(\frac{\eta \hat{B}^2 \hat{O} \hat{t}}{\hat{N}} \right) \bar{B}^2 \bar{O} - \left(\mu \hat{t}\right) \bar{N} + \left(\frac{D_N \hat{t}}{\hat{x}^2} \right) \frac{\partial^2 \bar{N}}{\partial \bar{x}^2}. \tag{3.19}$$

Further, we let $\hat{P} = P_c$, $\hat{O} = P_c$, $\hat{t} = 1/(\xi P_c)$ and $\hat{x}^2 = \hat{t} D_P$, and let $\hat{B} = B_c$ and $\hat{N} = \zeta B_c/(\xi P_c)$ where B_c is some value representing the expected magnitude of the concentration of B (Geris et al. 2008). We introduce dimensionless parameters

$$\begin{gathered} \bar{\epsilon} = \frac{\epsilon \xi P_c}{\zeta B_c}, \quad \hat{\delta} = \frac{\delta}{\xi P_c}, \quad \bar{\alpha} = \frac{\alpha}{\xi B_c}, \quad \bar{\beta} = \frac{\beta P_c}{\zeta} \\ \bar{\sigma} = \frac{\sigma \xi P_c}{\zeta B_c}, \quad \bar{\rho} = \frac{\rho}{\xi P_c}, \quad \bar{\eta} = \frac{\eta B_c P_c}{\zeta}, \quad \bar{\mu} = \frac{\mu}{\xi P_c}, \\ \bar{D}_O = \frac{D_O}{D_P}, \quad \bar{D}_B = \frac{D_B}{D_P}, \quad \bar{D}_N = \frac{D_N}{D_P}, \end{gathered} \tag{3.20}$$

Parameter	Dimensional Value	Units	Dimensionless Value
P_c	10^6	$\text{cells}\,\text{ml}^{-1}$	
B_c	10^{-7}	$\text{g}\,\text{ml}^{-1}$	
ξ	10^{-7}	$\text{ml}\,\text{cell}^{-1}\,\text{day}^{-1}$	
ζ	0.1	day^{-1}	
ϵ	10^{-10}	$\text{g}\,\text{ml}^{-1}$	10^{-3}
δ	6×10^{-3}	day^{-1}	6×10^{-2}
α	10^{-11}	$\text{g}\,\text{cell}^{-1}\,\text{day}^{-1}$	1000
β	2×10^{-4}	$\text{ml}\,\text{cell}^{-1}\,\text{day}^{-1}$	2000
σ	10^{-10}	$\text{g}\,\text{ml}^{-1}$	10^{-3}
ρ	100	day^{-1}	1000
η	10^3	$\text{ml}^2\,\text{g}^{-1}\,\text{cell}^{-1}\,\text{day}^{-1}$	1000
μ	100	day^{-1}	1000
D_P	4×10^{-8}	$\text{cm}^2\,\text{day}^{-1}$	
D_O	4×10^{-8}	$\text{cm}^2\,\text{day}^{-1}$	1
D_B	7×10^{-4}	$\text{cm}^2\,\text{day}^{-1}$	2×10^4
D_N	2.1×10^{-2}	$\text{cm}^2\,\text{day}^{-1}$	6×10^5

Table 3.1: Table of parameter values used to simulate Equations (3.21)-(3.24). See text for derivations and references. Non-dimensional values were found using the relationships presented in Equation (3.20).

and apply these to obtain

$$\frac{\partial \bar{P}}{\partial \bar{t}} = \bar{P}\big(1 - \bar{P} - \bar{O}\big) - \frac{\bar{B}\bar{P}}{\bar{\epsilon} + \bar{N}} + \frac{\partial^2 \bar{P}}{\partial \bar{x}^2}, \tag{3.21}$$

$$\frac{\partial \bar{O}}{\partial \bar{t}} = -\bar{\delta}\bar{O} + \frac{\bar{B}\bar{P}}{\bar{\epsilon} + \bar{N}} + \bar{D}_O \frac{\partial^2 \bar{O}}{\partial \bar{x}^2}, \tag{3.22}$$

$$\frac{\partial \bar{B}}{\partial \bar{t}} = \bar{\alpha}\bar{P} + \bar{\beta}\frac{\bar{B}^2\bar{O}}{\bar{\sigma} + \bar{N}} - \bar{\rho}\bar{B} + \bar{D}_B \frac{\partial^2 \bar{B}}{\partial \bar{x}^2}, \tag{3.23}$$

$$\frac{\partial \bar{N}}{\partial \bar{t}} = \bar{\eta}\bar{B}^2\bar{O} - \bar{\mu}\bar{N} + \bar{D}_N \frac{\partial^2 \bar{N}}{\partial \bar{x}^2}. \tag{3.24}$$

3.2.2 Parameters

The parameters used are listed in Table 3.1. Where possible the parameters have been based on information from experimental evidence or other mathematical models of fracture healing. However for many of the parameters where suitable values in the literature are not available the values used are based on order of magnitude estimates.

The limiting cell density, $P_c = 10^6\,\text{cells}\,\text{ml}^{-1}$, was determined based on an

assumption of a cell volume of 10^{-6} ml as used in Bailón-Plaza & van der Meulen (2001). To determine the proliferation rate of the progenitor cells we fitted a logistic growth curve to the data presented in Pratap et al. (2003) to get $\xi = 10^{-7}\,\mathrm{ml\,cell^{-1}\ day^{-1}}$. As it is difficult to quantify the rate of differentiation of progenitor cells to osteoblasts, $\zeta = 0.1\,\mathrm{day^{-1}}$ was chosen as an order of magnitude estimate.

Reported values for the active lifespan of osteoblasts vary between species, from 12 days in mice (Jilka et al. 1998) to 3 months in humans (Manolagas 2000). However these numbers account for changes in cell numbers due to differentiation of osteoblasts into osteocytes and bone lining cells, as well as cell death due to apoptosis. Since our model is focused on the early stages of intramembranous bone formation, before mineralisation has begun, it is unlikely that osteoblasts will be lost due to further differentiation. It has, however, been shown that apoptosis occurs in the periosteal callus during the early stages of fracture healing (Li et al. 2002), so we assume that all cell losses are due to apoptosis. To calculate the rate of apoptosis, we use the prevalence rates observed in histological slices. These prevalence rates are 0.6% in mice and 0.05% in humans (Jilka et al. 2007). The duration of apoptosis is approximately 2 hrs, so we take $\delta = 2.5 \times 10^{-4}\,\mathrm{hr^{-1}}$ for humans.

One of the key features of this model is that heterogeneities in cellular distributions can arise due to a difference in the rate of cellular differentiation at different spatial locations and are not due to cell migration effects such as chemotaxis. Thus we assume for the purposes of this model that both cell species move at the same rate and that this cell movement is occurring slowly with $D_P = D_O = 4 \times 10^{-8}\,\mathrm{cm^2\,day^{-1}}$

The typical concentrations of growth factors, like BMP, in serum are around $100 \times 10^{-9}\,\mathrm{g\,ml^{-1}}$ (Geris et al. 2008). Based on this we take $B_c = 10^{-7}\,\mathrm{g\,ml^{-1}}$. The half-life for growth factors like BMP are typically short, around 10 mins (Zhao et al. 2006, Kirsch, Nickel & Sebald 2000), giving $\rho = 100\,\mathrm{day^{-1}}$. The half-life for noggin is similarly short (reported < 30 mins (Glaser et al. 2003)) so we assume that it also has a decay rate of $\mu = 100\,\mathrm{day^{-1}}$. There are no reported quantified rates of BMP or noggin production by cells. So we determine these rate parameters for the chemical species as order of magnitude estimates. We take $\alpha = 10^{-11}\,\mathrm{g\,cell^{-1}\ day^{-1}}$ and $\beta = 2 \times 10^{-4}\,\mathrm{ml\,cell^{-1}\ day^{-1}}$.

The diffusion coefficients for the chemical species BMP and noggin *in vivo* are

not well known. Young et al. (1980) adapted the Stokes-Einstein equation so that diffusion coefficients of a protein in water could be related to the mass of that protein. BMP has a molecular mass of 26 kDa, using their formula a value of $D_B = 7{\times}10^{-2}\,\mathrm{cm}^2\,\mathrm{day}^{-1}$ was obtained. However diffusion through the extracellular space is much slower then diffusion through water. Additionally experimental evidence indicates that BMP 4 has only a short range of action, within a few cell widths, so we decrease the diffusion coefficient by 2 orders of magnitude and use $D_B = 7 \times 10^{-4}\,\mathrm{cm}^2\,\mathrm{day}^{-1}$. The short range of BMP is due to its molecular structure which allows it to bind to the ECM restricting its diffusion through the extracellular space. Noggin has a similar molecular weight of 25 kDa, however it has been shown to act over a much longer range than BMP (Jones & Smith 1998). Based on the larger range of action we make the diffusion coefficient 30 times larger then that for BMP, giving $D_N = 2.1 \times 10^{-3}\,\mathrm{cm}^2\,\mathrm{day}^{-1}$.

3.3 Fast Time Scales

One of our underlying hypothesises of this model is that cellular differentiation is driven by a chemical pre-pattern. For spatial patterning in the cell population it must be that a spatial pattern evolves in the chemical species. As described in Appendix B, for a Turing pattern to evolve certain conditions must be satisfied. It is difficult to analyse the full system of four coupled PDEs, however we observe that the parameters relating to the chemical species are 3 orders of magnitude larger than those for the cellular species. This suggests that there are two time scales for this problem. A fast time scale that the chemicals are reacting on and a slow time scale for the cells. From a biological perspective it would also be reasonable to expect this two time scale behaviour to exist. Cellular processes such as proliferation and differentiation take place over days, whereas proteins such as BMP and noggin have half-lives measured in minutes.

By applying a time rescaling to obtain the fast time system, we can effectively reduce our system to two coupled PDEs for the chemical species, BMP and noggin, making it much easier to analyse the pattern forming abilities of our model. Indeed our reduced system bears resemblance to the well-studied Gierer-Meinhardt kinetics, which are known to produce Turing patterns.

We perform the time rescaling by letting $\bar{t} = \tau t^*$ with

$$\tau = \frac{\zeta}{\beta P_c} = \frac{1}{\bar{\beta}}. \tag{3.25}$$

Noting that $\tau = \mathcal{O}(10^{-3})$, and further that $\bar{\delta} = \mathcal{O}(10^1)$, $\bar{D}_O = \mathcal{O}(10^0)$, $\bar{\alpha}$, $\bar{\beta}$, $\bar{\rho}$, $\bar{\eta}$, $\bar{\mu} = \mathcal{O}(10^3)$, $\bar{D}_B = \mathcal{O}(10^4)$ and $\bar{D}_N = \mathcal{O}(10^6)$. By applying this rescaling to the non-dimensionalised equations and taking the limit as $\tau \to 0$ we get

$$\frac{\partial \bar{P}}{\partial t^*} = 0, \tag{3.26}$$

$$\frac{\partial \bar{O}}{\partial t^*} = 0, \tag{3.27}$$

$$\frac{\partial \bar{B}}{\partial t^*} = \tau\left(\bar{\alpha}\bar{P} + \bar{\beta}\frac{\bar{B}^2\bar{O}}{\bar{\sigma} + \bar{N}} - \bar{\rho}\bar{B} + \bar{D}_B\frac{\partial^2 \bar{B}}{\partial \bar{x}^2}\right), \tag{3.28}$$

$$\frac{\partial \bar{N}}{\partial t^*} = \tau\left(\bar{\eta}\bar{B}^2\bar{O} - \bar{\mu}\bar{N} + \bar{D}_N\frac{\partial^2 \bar{N}}{\partial \bar{x}^2}\right). \tag{3.29}$$

In this reduced fast time system the cell species appear to be at steady state, however the chemical species are still diffusing and reacting which could lead to possible pattern formation.

3.3.1 Fast Time Results

We can take the reduced fast time system and solve it numerically to show that spatial patterns can arise in the chemical concentrations. For these simulations we used the parameters as listed in Table 3.1. We assumed that the cell densities of the progenitor cells and the osteoblasts were spatially homogeneous. The boundary conditions used were zero flux for all boundaries. By using these boundary conditions we can isolate the domain from other external factors which are typically present and instead focus on understanding the underlying processes that are occurring. For the initial conditions the steady state solution to the kinetics without diffusion and with $\bar{\sigma} = 0$ was used. These initial conditions were used as they are easy to find analytically, furthermore because $\bar{\sigma}$ is small compared to $\bar{N}$ the error introduced by the assumption that $\bar{\sigma} = 0$ is small. To initiate the pattern formation a small amount of additive white Gaussian noise was added to the initial BMP concentration. The simulations were carried out on a 1D domain using the MATLAB (Release 2012b) function `pdepe` with 200 spatial mesh points.

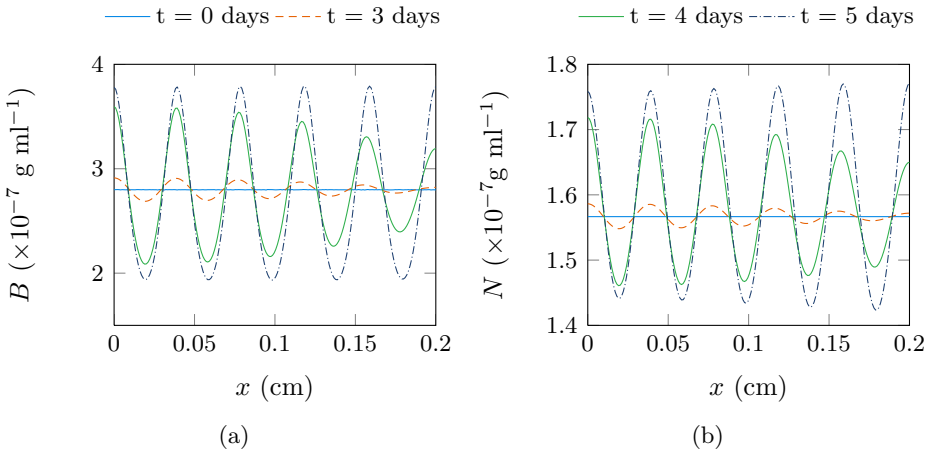

Figure 3.2: Concentration profiles of (a) BMP and (b) noggin as the solutions to the fast time system in Equations (3.28) and (3.29). For these simulations the cell density of progenitor cells and osteoblasts were held constant at $\bar{P}(x,t) = 0.8$, $\bar{O}(x,t) = 0.2$ and all other parameters were as in Table 3.1. Initially (light blue) the concentrations were almost spatially homogeneous, with $\bar{B}(x,0) = 2.8$+noise and $\bar{N}(x,0) = 1.56$. After 3 days (orange dashes) a pattern with a dominant wave length of 0.4 mm has become apparent. By 4 days (green solid) the amplitude of the pattern has increased however the dominant wave length has not changed. By 5 days (dark blue dot dashed) the pattern appears to have become steady.

The first simulation conducted was with $\bar{P}(x,t) = 0.8$ and $\bar{O}(x,t) = 0.2$ chosen as the steady state values. This gave initial conditions for the concentrations of BMP and noggin as $\bar{B}(x,0) = 2.8 + \text{noise}$ and $\bar{N}(x,0) = 1.56$. The results for this simulation are shown in Figure 3.2. We observe that by day 3 a regular pattern has begun to appear in the concentration levels of BMP and noggin. The patterns for BMP and noggin are in phase, which is an expected result of the Gierer-Meinhardt equations (Murray 2003). As time progresses the amplitude of the pattern increases, and after 5 days appears to have become steady, which is illustrated below. We see that the final pattern has a wavelength of $400\,\mu$m.

To demonstrate the stability of this steady state we calculated the absolute change in the solution from time step to time step as

$$\Delta_B = \sum_i |\bar{B}(x_i, t_{n+1}) - \bar{B}(x_i, t_n)|, \tag{3.30}$$

$$\Delta_N = \sum_i |\bar{N}(x_i, t_{n+1}) - \bar{N}(x_i, t_n)|. \tag{3.31}$$

A plot of these changes over time is shown in Figure 3.3. We see that after

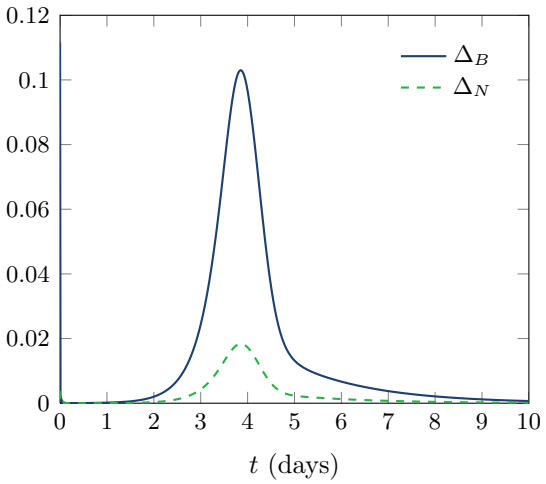

Figure 3.3: Plot showing the total absolute difference between solutions at each time step for the solution shown in Figure 3.2. The large spike indicates the period in which the pattern is evolving and hence there is a large change in the solution at every time step. We see that once this spike has diminished the amount of change continues to decrease indicating the the steady state found is stable.

the establishment of the pattern, the amount of change in B and N continues to decrease over time indicating the stability of the pattern.

3.3.2 Turing Parameter Analysis

We can see that our fast time model produces Turing patterns. In Appendix B we derived a set of conditions that must be satisfied for Turing patterns to evolve. In this section we use these conditions to provide some analysis on the range of parameters that will give rise to patterns for the fast time system in Equations (3.28) and (3.29).

To begin with we briefly repeat the conditions here. For a non-dimensional reaction-diffusion equation

$$\frac{\partial u}{\partial t} = \gamma f(u,v) + \frac{\partial^2 u}{\partial x^2}, \tag{3.32}$$

$$\frac{\partial v}{\partial t} = \gamma g(u,v) + d\frac{\partial^2 v}{\partial x^2}, \tag{3.33}$$

with $d > 1$, it is possible for Turing patterns to evolve if the following condi-

tions are true

$$f_u(\bar{u},\bar{v}) + g_v(\bar{u},\bar{v}) < 0, \tag{3.34}$$

$$f_u(\bar{u},\bar{v})g_v(\bar{u},\bar{v}) - f_v(\bar{u},\bar{v})g_u(\bar{u},\bar{v}) > 0, \tag{3.35}$$

$$df_u(\bar{u},\bar{v}) + g_v(\bar{u},\bar{v}) > 0, \tag{3.36}$$

$$(df_u(\bar{u},\bar{v}) + g_v(\bar{u},\bar{v}))^2 > 4d(f_u(\bar{u},\bar{v})g_v(\bar{u},\bar{v}) - f_v(\bar{u},\bar{v})g_u(\bar{u},\bar{v})), \tag{3.37}$$

where $\bar{u},\bar{v}$ are the steady state values of u, v for the reaction terms in the absence of diffusion, i.e. $f(\bar{u},\bar{v}) = 0,\ g(\bar{u},\bar{v}) = 0$. In addition for physically realistic solutions to exist the kinetics f and g must have a confined set in the positive domain.

In our analysis of the pattern forming capabilities of Equations (3.28) and (3.29) we make some simplifying assumptions. Firstly we assume that the cell populations are constant with $\bar{P}(x,t) = \bar{P}_0$ and $\bar{O}(x,t) = \bar{O}_0$. The second assumption is that $\bar{\sigma} = 0$, since $\bar{\sigma}$ is much less then the value of $\bar{N}$ at the steady state.

In order to apply the conditions above (Equations (3.34)–(3.35)) we need to further non-dimensionalise Equations (3.28) and (3.29) to reduce the number of variables. To do this we rescale the variables as

$$u = \frac{\bar{\eta}}{\bar{\beta}}\bar{B}, \quad v = \frac{\bar{\mu}\bar{\eta}}{\bar{\beta}^2\bar{O}_0}\bar{N}, \quad \tilde{t} = \frac{\tau\bar{D}_B}{L^2}t^*, \quad \tilde{x} = \frac{x}{L}, \tag{3.38}$$

where L is the length of the domain. We introduce new parameters

$$a = \frac{\bar{\alpha}\bar{\eta}\bar{P}_0}{\bar{\mu}\bar{\beta}}, \quad b = \frac{\bar{\rho}}{\bar{\mu}}, \quad \gamma = \frac{\bar{\mu}L^2}{\bar{D}_B}, \quad d = \frac{\bar{D}_N}{\bar{D}_B}. \tag{3.39}$$

Using these we can rewrite Equations (3.28) and (3.29) as

$$\frac{\partial u}{\partial \tilde{t}} = \gamma\left(a - bu + \frac{u^2}{v}\right) + \frac{\partial^2 u}{\partial \tilde{x}^2}, \tag{3.40}$$

$$\frac{\partial v}{\partial \tilde{t}} = \gamma(u^2 - v) + d\frac{\partial^2 v}{\partial \tilde{x}^2}. \tag{3.41}$$

This is the non-dimensional form identical to that in Equations (3.32) and (3.33), with

$$f(u,v) = a - bu + \frac{u^2}{v}, \tag{3.42}$$

$$g(u,v) = u^2 - v, \tag{3.43}$$

and it should be noted that this is a non-dimensional form of the standard Gierer-Meinhardt activator-inhibitor system (Gierer & Meinhardt 1972).

We find the steady state to be

$$(\bar{u}, \bar{v}) = \left(\frac{a+1}{b}, \frac{(a+1)^2}{b^2} \right), \tag{3.44}$$

and evaluate the partial derivatives of the kinetics at this steady state to give

$$\begin{aligned} f_u(\bar{u}, \bar{v}) &= \frac{b(1-a)}{a+1}, \quad f_v(\bar{u}, \bar{v}) = -\frac{b^2}{(a+1)^2}, \\ g_u(\bar{u}, \bar{v}) &= \frac{2(a+1)}{b}, \quad g_v(\bar{u}, \bar{v}) = -1. \end{aligned} \tag{3.45}$$

Since by definition u is the activator of the system and must be self-activating, it must be that $f_u(\bar{u}, \bar{v}) > 0$ and hence that $0 < a < 1$. We can substitute these partial derivatives into Equations (3.34)–(3.37). The first condition gives the constraint

$$b < \frac{a+1}{1-a}. \tag{3.46}$$

Applying the second condition yields $b > 0$ which must always be true since both $\bar{\rho}$ and $\bar{\mu}$ are positive constants. Applying the third condition gives

$$b > \frac{a+1}{d(1-a)}. \tag{3.47}$$

Applying the fourth condition results in the following quadratic in b

$$d^2(1-a)^2 b^2 - 2d(1+a)(3+a)b + (1-a)^2 > 0, \tag{3.48}$$

with roots given by

$$b_1, b_2 = \frac{1+a}{d(1-a)^2} \Big(a + 3 \pm \sqrt{8(a+1)} \Big). \tag{3.49}$$

For Equation (3.48) to be true, it must be that $b > b_1$ and $b > b_2$, or $b < b_1$ and $b < b_2$. If we consider the latter case then

$$b < \frac{1+a}{d(1-a)^2} \Big(a + 3 - \sqrt{8(a+1)} \Big), \tag{3.50}$$

which combined with Equation (3.47) gives

$$\frac{a+1}{d(1-a)} < \frac{1+a}{d(1-a)^2} \Big(a + 3 - \sqrt{8(a+1)} \Big), \tag{3.51}$$

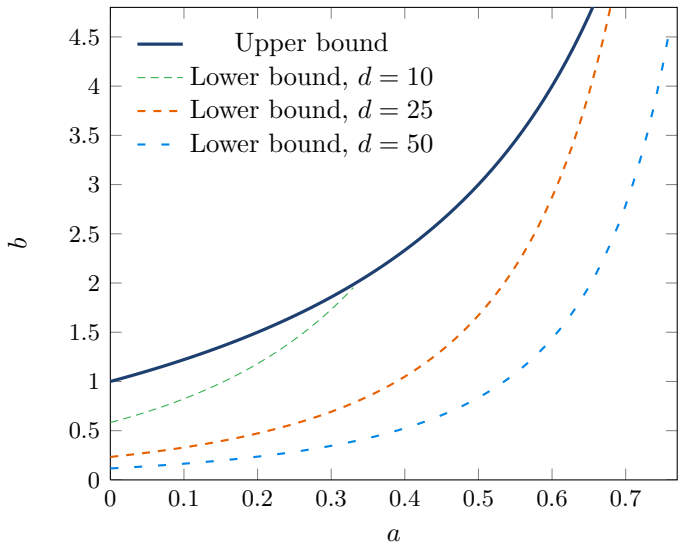

Figure 3.4: Parameter space for the possible evolution of patterns for the kinetics given by Equations (3.32) and (3.33). For it to be possible for patterns to evolve our parameter choices must lie in a region below the thick solid line and above the dashed line for the known parameter d.

which can be rearranged and simplified to

$$1 + a > 2. \tag{3.52}$$

Clearly this cannot be the case when $0 < a < 1$ so it must be that to satisfy the fourth condition

$$b > \frac{1+a}{d(1-a)^2}\Big(a + 3 + \sqrt{8(a+1)}\Big), \tag{3.53}$$

and we can see that if this condition is satisfied then the condition given in Equation (3.47) will also be satisfied.

Thus for it to be possible for a Turing pattern to evolve the following constraints on parameters a, b and d must be satisfied

$$0 < a < 1, \tag{3.54}$$

$$\frac{1+a}{d(1-a)^2}\Big(a + 3 + \sqrt{8(a+1)}\Big) < b < \frac{a+1}{1-a}. \tag{3.55}$$

This parameter space is illustrated in Figure 3.4 for different values of d.

The existence of a confined set in the positive quadrant $(u > 0, v > 0)$ for generalised Gierer-Meinhardt kinetics was proven in Huang et al. (2007). Since

a confined set for the kinetics without diffusion is also a confined set once diffusion has been included (Smoller 1994), this ensures that our solutions for u and v will remain physically realistic.

Influence of Cell Population Levels

We can also examine how changing the assumed value of the cell populations influences the pattern formation process. This is of interest as when we consider the full system of equations we expect the cell populations to be changing due to differentiation. Interestingly, when we perform the further nondimensionalisation to give rise to Equations (3.40) and (3.41), the new parameters a, b, γ and d have no dependence on the size of the osteoblast population $\bar{O}_0$. Furthermore, since only the parameter a depends on $\bar{P}_0$ it is possible to construct a bound on $\bar{P}_0$ such that patterns can arise. From Equation (3.54) and the parameters in Table 3.1 we get a bound of $0 < \bar{P}_0 < 2$. Given these parameters Equation (3.48) yields a tighter upper bound to give $0 < \bar{P}_0 < 0.86$ and we call $\bar{P}_0 = 0.86$ the critical value of $\bar{P}_0$ for patterns to arise. Since a value of $\bar{P}_0 = 1$ corresponds to the progenitor cells being at full carrying capacity, this bound shows that patterns can arise for most physically realistic values of $\bar{P}_0$.

Whilst the value of $\bar{O}_0$ has no effect on the pattern forming ability of the system it will have an effect on the final pattern obtained. The inclusion of $\bar{O}_0$ in the scaling of $\bar{N}$ (Equation (3.38)) means that changes in $\bar{O}_0$ will change both the magnitude and average value of the concentration profile of $\bar{N}$ when returning to the original system of equations.

Since $\bar{P}_0$ influences the pattern forming ability of the system it is also of interest to see if changing $\bar{P}_0$ has an influence on the dominant spatial frequency ν of the final pattern. As shown in Appendix B the solution to the linearised system is given by

$$\mathbf{w} = \sum_k c_k e^{\lambda(k)t} \cos(kx), \tag{3.56}$$

where $\mathbf{w} = (u - \bar{u}, v - \bar{v})^T$, k is the wavenumber and corresponds to spatial frequency ν as $k = 2\pi\nu$ and $\lambda(k)$ is the eigenvalue associated with wavenumber k and is related to temporal growth. A mode with wavenumber k is unstable if $\mathrm{Re}\{\lambda\} > 0$, and the larger λ is, the faster the instability will grow. This means that the expected dominant frequency of a Turing pattern corresponds

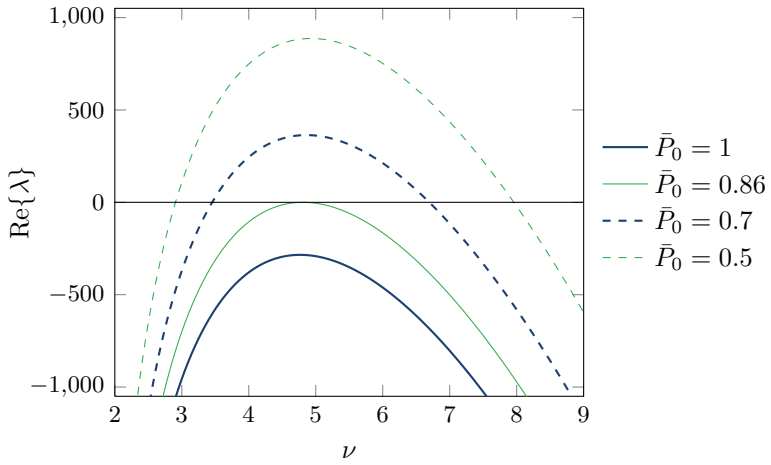

Figure 3.5: Re$\{\lambda\}$ versus spatial frequency ν for different values of $\bar{P}_0$. For the parameters $b = 1, \gamma = 5000, d = 30$ the value $\bar{P}_0 = 0.86$ represents a critical value, values of $\bar{P}_0$ above this point will never give rise to patterns, whereas values of $\bar{P}_0$ below this could give rise to patterns. As $\bar{P}_0$ decreases the dispersion curves rise and a larger range of frequencies become unstable. However we note that for each of the curves the frequency at which the maximum value of λ occurs does not change substantially, meaning that the predicted dominant frequency of the final pattern will be the same.

to the wavenumber for which $\lambda(k)$ is a maximum, as it will grow the fastest. In Figure 3.5 we plot the Re$\{\lambda\}$ versus the spatial frequency ν for varying values of $\bar{P}_0$ using the parameters in Table 3.1. We see that as $\bar{P}_0$ decreases, the range of unstable modes increases, however the frequency at which the maximum value of Re$\{\lambda\}$ occurs does not change significantly.

This is important when considered in the context of the full model. As progenitor cells differentiate the progenitor density decreases. The fact that this decrease in density is not likely to induce a change in the pattern frequency allows the frequency of the chemical pattern to remain stable for longer, thus allowing the chemical patterning to have a greater effect on the cellular populations.

Another factor to consider for the full model is that when the progenitor density is high i.e. greater than the critical value of $\bar{P}_0$ then cellular differentiation will occur en masse across the domain. As the progenitor cell population decreases due to this differentiation it will eventually become low enough to allow patterning in the chemical species to occur, which in turn will result in pattering visible in the cell populations.

3.4 Full System

Observing that it is possible for patterns to evolve in the fast time system and providing some analysis on the conditions under which this will occur, we turn our attention to solving the full system as given by Equations (3.7)-(3.10). As before the parameters used are those given in Table 3.1. We solve this full system in 1D and then in 2D.

3.4.1 1D Results

For the 1D simulations the boundary conditions used were zero flux for all species and the initial conditions used were $\bar{P} = 0.8$, $\bar{O} = 0.2$, $\bar{B} = 2.8$+noise and $\bar{N} = 1.568$. A typical solution is shown in Figure 3.6. The 1D system was solved numerically using the inbuilt MATLAB (Release 2012b) solver `pdepe` with 200 spatial mesh points.

After one day the concentration levels for BMP and noggin start to show a regular pattern, with a very small magnitude. The population levels of the progenitor cells have decreased due to differentiation and the osteoblasts numbers have increased. However the cell populations are still spatially homogeneous.

After two days the magnitude of the pattern observed in the concentration of BMP and noggin has grown substantially. By this stage the profile for BMP appears to have almost reached steady state. For the cellular populations a regular pattern has started to develop in response to the chemical pattern. The peaks of BMP increase the differentiation rate, so the profile for the osteoblasts is in phase with the chemical pattern. Correspondingly, the population of progenitor cells is out of phase with the chemical pattern.

The spatial heterogeneity continues to grow in the cellular species and we see that after 5 days the patterning has become much more pronounced. Also as differentiation is still occurring across the entire domain, albeit at differing rates we still see a decrease in the average value of progenitor cells and a corresponding increase in the average value of the osteoblasts.

Despite the changes in the cellular populations we observe that the BMP concentration profile appears to be approximately stable. Importantly, as predicted by the Turing pattern analysis, the frequency of the pattern is not changing so that the peaks and troughs remain in the same location. This allows the slower reacting cellular species to have time to react and differentiate

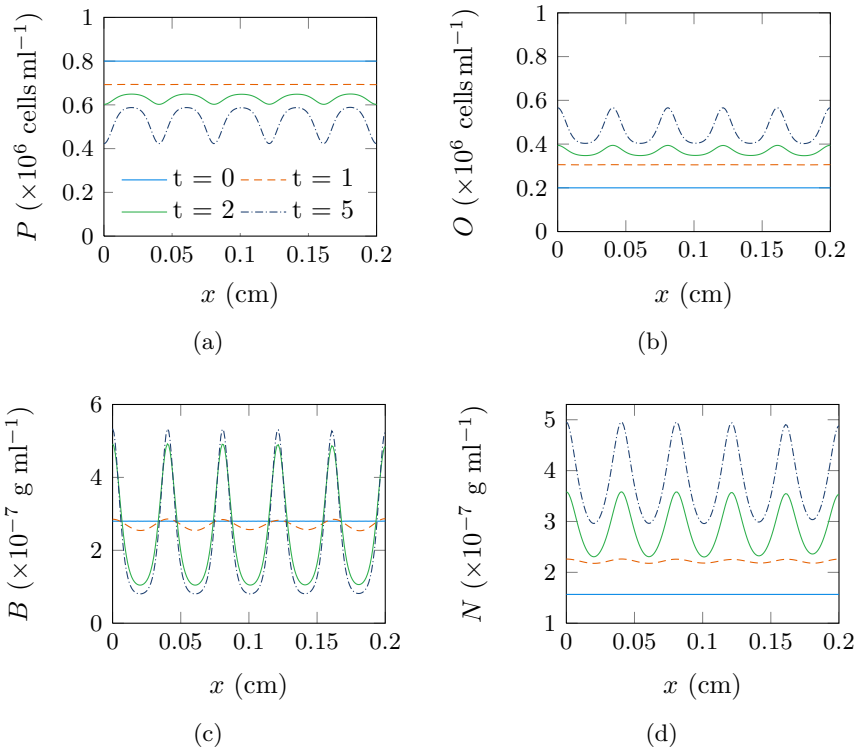

Figure 3.6: Results of numerical simulation for the full system in 1D. We see that after 1 day a pattern is starting to evolve in the chemical concentrations however the cell populations remain spatially homogeneous. By 2 days the BMP concentration has almost stabilised, and the cell populations have begun to respond to the chemical patterning. As time progresses the spatial heterogeneity in the cell populations becomes more pronounced.

according to the BMP pattern.

In contrast the noggin concentration profile is both increasing in magnitude and in average value. Again this is consistent with the Turing parameter analysis. Where an increase in osteoblast numbers was predicted to result in an increase in both average value and magnitude of the noggin concentration.

We can compare these simulation results to results reported in biological literature. These simulations were conducted on a domain that is 2 mm long. This gives a wave length of our pattern of 0.4 mm. This appears to be consistent with the periodicity of the mineralisation observed in histology (Manjubala et al. 2009). Whilst our model is not for the mineralisation we would expect the pattern of cellular differentiation to match the periodicity of the mineralisation.

It is difficult to find experimental data on fracture healing for the very short time periods for which we are interested. *In vitro* studies on the effects of BMP on progenitor cell differentiation show that 3 days after the application of BMP-2,-6 and -9 there had been a substantial amount of cellular differentiation to osteoblasts (Cheng et al. 2003). Histology of rat fractures show that cellular differentiation has occurred by day 2 (Yoshimura et al. 2001). The exact speed of cellular differentiation in response to BMP signalling is unknown but it would appear that the results of our model are consistent with the time frames observed experimentally. Additionally, if we consider the sheep osteotomy model (see for example (Manjubala et al. 2009)) after 2 weeks mineralised callus is observable. Cellular differentiation is the first process to occur and is followed by other processes to give rise to mineralised bone. This means that for the BMP pre-pattern to be responsible for a cellular pattern, which then influences the appearance of the new mineralised bone, it must be that the cellular species are responding to the chemical pre-pattern quickly. Thus the appearance of patterning in the cell species after 2 days, and growing stronger quickly as time goes on, supports our hypothesis that an underlying chemical pre-pattern gives rise to patterning in the cellular species which in turn effects the structure of new intramembranous bone.

3.4.2 2D Results

Using the same kinetics we also solved the full system on a 2D domain. To find the 2D numerical solutions a finite volume approach was used for the spatial discretisation. The time integration was done using the MATLAB (Release 2012b) function `ode15s`. The results presented in Figure 3.6 were obtained using 100 mesh points in each dimension. As in the above simulations, zero flux boundary conditions were used and the initial conditions were $\bar{P} = 0.8$, $\bar{O} = 0.2$, $\bar{B} = 2.8$+noise and $\bar{N} = 1.568$.

There are two noticeable difference between the 1D and 2D results. The first difference is that in 1D the concentration levels formed a uniform pattern across the domain, however in the 2D results the peaks are more randomly scattered rather then forming a uniform pattern. There is still a degree of patterning in the 2D results. There appears to be a maximum and minimum distance between peaks, as usually occurs in spot forming Turing patterns. The final distribution of these peaks is determined by the initial conditions

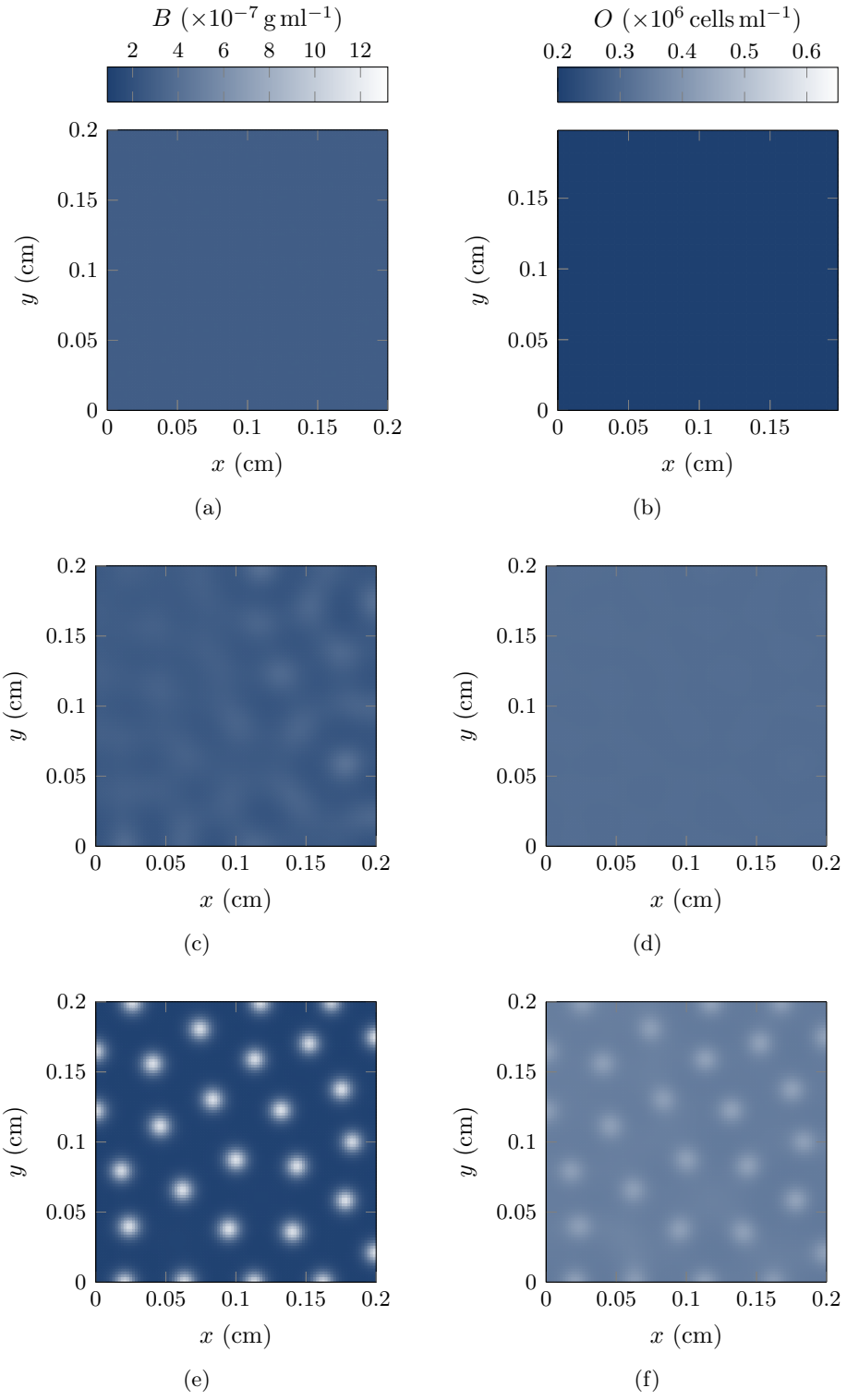

Figure 3.7: Continued on next page.

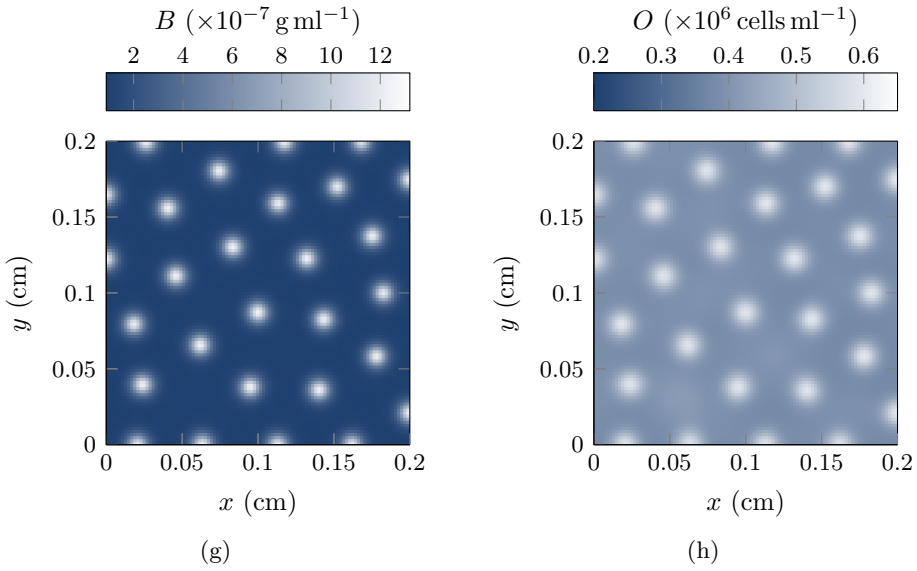

Figure 3.6: 2D simulation results showing concentration and cell population profiles for BMP and osteoblasts. The left column shows the evolution of the BMP concentration profile and the right column shows the osteoblast profile. The profiles are shown for $t = 0$ (top row, previous page), $t = 1$ day (2nd row, previous page), $t = 2$ days (3rd row, previous page) and $t = 4$ days (this page).

and parameters used. The other major difference between the 1D and 2D results is the magnitude of the peaks for both BMP and noggin, with the 2D simulations producing results where the peaks are much larger.

The temporal progression occurs in much the same fashion as for the 1D case. After 1 day the beginnings of a pattern is detectable in the concentration levels of BMP and noggin, however at this point the pattern appears to have a more labyrinth like appearance compared to the spotted patterns apparent at the later time steps. The cell species appear to have mostly changed homogeneously to this point.

By 2 days the BMP concentration levels appear to have almost reached steady state and there is a distinct spotted pattern. By this stage the cell population levels have started to react to the chemical patterning giving rise to an obvious spatial heterogeneity to the cell populations. As before, the regions of high BMP, have a faster differentiation rate of cells which gives rise to regions of high numbers of osteoblasts.

We see that as time continues the overall numbers of osteoblasts continues

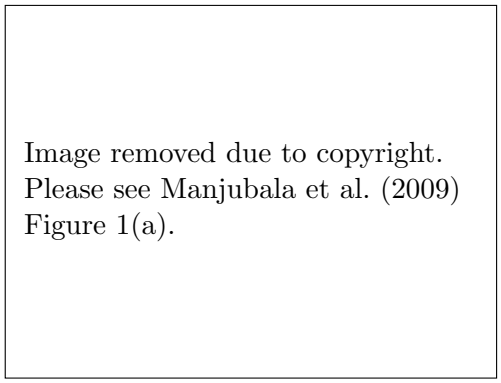

Figure 3.7: Histological section of an ovine tibial osteotomy 2 weeks post surgery showing the structure of newly formed intramembranous bone (Manjubala et al. 2009). The black rectangular regions are the pre-existing cortical bone, the irregularly patterned black material in the regions adjacent to the cortical bone is the new intramembranous bone. The white region is bone marrow and the pink regions are fibrous tissue. The spatial frequency of the structure of the new intramembranous bone is consistent with the spatial frequency of our simulation results.

to increase, as well as this the difference between the values at the top of the peaks and the bottom of the troughs is increasing. Like the 1D results the BMP concentration profile seems to reach a steady state, but the noggin concentration levels continue to grow due to the changes in the osteoblast population.

Though difficult, we can make some comparisons between the spatial and temporal appearance of our results and the appearance of new intramembranous bone seen in histology (see for example Figure 3.7 taken from Manjubala et al. (2009) or the histological images in Epari et al. (2006)). Our hypothesis is that the spatially heterogeneous distribution of osteoblasts across the domain is a contributing factor to the appearance of the new intramembranous bone. The spatial frequency observed in our simulation results is consistent with the spatial frequency observed in the histological sections, supporting this hypothesis. We also note that like the 1D case the temporal development of the heterogeneity would appear to be consistent with the experimental results, with rapid evolution of the spatial patterning allowing time for slower processes like mineralisation to occur.

We note that our model is only capable of forming spotted patterns and not the labyrinth like patterns that are sometimes observed in Turing patterns. This is due to the underlying kinetics of BMP and noggin. The Gierer-Meinhardt

kinetics will only give rise to labyrinth patterns when activator saturation is included in the model (Koch & Meinhardt 1994). For our purposes the spotted formation is sufficient evidence that cellular differentiation could be caused due to an underlying pattern in BMP and noggin and that the spatial and temporal appearance of the spots are consistent with histological observations. However, it may be of interest in future models to include saturation to obtain labyrinth patterns which may better replicate the structure of new bone.

If we consider the extension of the model to a 3D domain, we would expect that the spotted pattern observed in 2D would become a pattern of spheres in 3D. This is in agreement with numerical results obtained for Turing pattern formation using different kinetics (Leppänen et al. 2002). Again if we wished to recover a interconnected labyrinth like arrangement of osteoblasts then a change needs to be made to the kinetics of our model. As discussed above the inclusion of BMP (activator) saturation gives rise to labyrinth patterns in 2D and it would be expected that upon extension to 3D the labyrinth like behaviour would persist.

The use of the finite volume method and the lack of advection in our model means that the implementation of the model in 3D should be a relatively straightforward task. However the introduction of an additional dimension will substantially increase the number of nodes in the simulation. This means that care will need to be taken to ensure that the numerical scheme is efficient and that memory is managed appropriately.

3.5 Summary

In this chapter we have presented a new model for cellular differentiation as it occurs during intramembranous bone formation in fracture healing. We began with the hypothesis that cellular differentiation is guided by a chemical pre-pattern. From this starting point we built a model with biologically relevant terms for cellular differentiation of osteoblast progenitor cells to osteoblasts, where differentiation was dependent on a chemical pre-pattern established through the kinetics of BMP and noggin.

When considering the fast time dynamics of our system of equations, we demonstrated that a simplified version of our kinetics for BMP and noggin is the same as the well studied Gierer-Meinhardt kinetics. In this form it is

easy to apply standard analysis of Turing patterning processes to define ranges of parameters for patterning to evolve. This analysis also allowed us some insight into the expected patterning that will result. An important result from this analysis was that the frequency of patterns in BMP and noggin is not strongly dependent on the cell density of progenitor or osteoblast cells. This means that the chemical pattern will be stable even as the cell populations are changing.

When we consider the full problem we achieved results that appeared to be consistent with our interpretation of the relevant biology, both spatially and temporally. Our 2D model indicated that patterning in the cellular species was apparent after 2 days and a strong pattern was observable after 4 days. Within the biological context it is important that the cells react quickly to the chemical pre-pattern, as this would then allow time for the other processes required for mineralised bone to form. Spatially the distribution of pools of osteoblasts appeared consistent the spatial frequency observed in the structure of new intramembranous bone. Thus, our model appears to support our hypothesis that a chemical pre-pattern gives rise to a heterogeneous distribution of differentiated osteoblasts and that this distribution could give rise to the structural appearance of new intramembranous bone.

4

Cellular Differentiation in a Growing Domain

Previously we built a model for cellular differentiation of osteoblast progenitor cells into osteoblasts. We modelled this differentiation process as being dependent on the concentration of two diffusible agents, BMP and its inhibitor noggin. The underlying reactions of BMP and noggin, along with diffusion, allowed the evolution of temporally stable, spatially non-homogeneous patterns in their concentration. These patterns in the chemical species induced a spatial structure in the distribution of cellular differentiation events. Our proceeding work with this model was confined to a fixed 2D domain. This allowed us to determine some of the critical reaction parameters, given the appropriate length and time scales. However the simplified domain and boundary conditions do not provide a good representation of the growing callus during fracture repair.

During fracture healing the callus grows in a outward direction from the existing cortical bone. Thus in order for our model to more accurately represent a fracture healing context we must consider the model on a growing domain. It is well known that pattern forming mechanisms can be influenced by length (and time) scales. It is therefore possible that the growth of the callus (and hence the domain of our model) will have an impact on the pattern forming ability of our model. Changes in the chemical pre-patterns would influence the predicted distribution of osteoblasts, which, whilst not part of our model, would influence the subsequent mineralisation.

As a first step towards simulating our model on a growing domain, we impose boundary conditions that are more consistent with the context of fracture repair whilst considering a non-growing domain. In this context one boundary represents the intact cortical bone and the opposite boundary represents the periosteum. Within this set-up we can observe a moving front of pattern for-

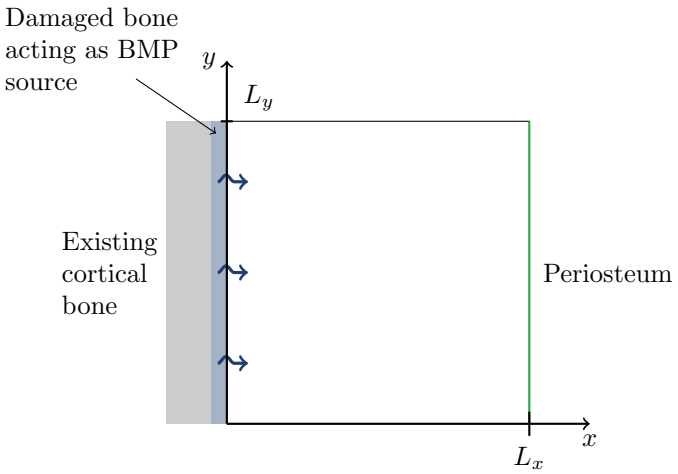

Figure 4.1: Schematic of the domain between $x = 0$ and $x = L_x$, and $y = 0$ and $y = L_y$. The left boundary is adjacent to the pre-existing cortical bone and the right boundary represents the periosteum. There is a source of BMP released by the damaged bone surface.

mation, and it is possible to determine the speed of the front of differentiation.

Having established a speed of propagation of the patterning front we then consider a growing domain. To create a growing domain we then let the boundary representing the periosteum expand away from the cortical bone, to simulate the growth of the callus during fracture healing. This allows us to explore the effect of the domain growth on the cellular differentiation.

4.1 Determining the Wave Speed of Cellular Differentiation

We begin our exploration of the model on a non-growing domain, however we introduce boundary conditions which are relevant to the fracture healing context. We now consider a domain such as that illustrated in Figure 4.1, where one boundary of the domain represents the intact cortical bone and the opposite boundary represents the periosteum. It is believed that when the bone is damaged, BMP stored in the extracellular matrix is released, and that this release of BMP from the bone helps initiate the fracture healing cascade.

In these simulations we observe that cellular differentiation first begins at the existing bone surface, and then as time progresses differentiation begins to occur further and further away from the bone surface. This could be viewed

as a wave of cellular differentiation across the domain. These simulations, where the domain is non-growing, allow us to view the natural wave speed of this front of differentiation. Knowing this wave speed will provide additional information about the time and length scales involved as we move towards a model with callus growth.

In this section we continue to use the model described in Chapter 3, however make appropriate changes to the boundary conditions to better represent the fracture callus region. For completeness we repeat the non-dimensional form of the equations here,

$$\frac{\partial \bar{P}}{\partial \bar{t}} = \bar{P}\big(1 - \bar{P} - \bar{O}\big) - \frac{\bar{B}\bar{P}}{\bar{\epsilon} + \bar{N}} + \nabla^2 \bar{P}, \tag{4.1}$$

$$\frac{\partial \bar{O}}{\partial \bar{t}} = -\bar{\delta}\bar{O} + \frac{\bar{B}\bar{P}}{\bar{\epsilon} + \bar{N}} + \bar{D}_O \nabla^2 \bar{O}, \tag{4.2}$$

$$\frac{\partial \bar{B}}{\partial \bar{t}} = \bar{\alpha}\bar{P} + \bar{\beta}\frac{\bar{B}^2\bar{O}}{\bar{\sigma} + \bar{N}} - \bar{\rho}\bar{B} + \bar{D}_B \nabla^2 \bar{B}, \tag{4.3}$$

$$\frac{\partial \bar{N}}{\partial \bar{t}} = \bar{\eta}\bar{B}^2\bar{O} - \bar{\mu}\bar{N} + \bar{D}_N \nabla^2 \bar{N}. \tag{4.4}$$

Our domain now describes a region which is bounded by the existing bone surface on the left and the periosteum on the right. When bone is damaged it triggers a release of BMP. We model this as a source of BMP at the left boundary. In addition, we assume that the existing bone is a solid and that cells cannot migrate into this region nor can noggin diffuse across this boundary. The right boundary represents the periosteum, a membranous material that normally lies on the surface of bone, however during fracture healing the periosteum separates from the bone and healing occurs in the region between it and the bone surface. We assume that cells cannot cross the periosteum and that it is impermeable to BMP and noggin. We make this choice to highlight the interior process. It may indeed be possible for these species to cross the periosteum, however we assume that such flux is not significant. By setting these boundaries to be no flux we remove any potential exterior influences on our theoretical study. Similarly, on the top and bottom boundaries we also use zero flux conditions. We are mostly interested in the behaviour in the direction of the callus growth and by using these zero flux conditions we can isolate our domain from further external influences. We assume that the domain represents a region that is somewhat removed from the fracture gap and hence ignore the influence of chemical signals that may be diffusing from the

haematoma. Thus the boundary conditions used are zero flux for all species on all boundaries with the exception of

$$B(0, y, t) = 5 \times 10^{-7}\,\mathrm{g\,ml^{-1}}, \tag{4.5}$$

on the left boundary $x = 0$. This concentration of BMP at the boundary was chosen as it represented a value greater than the initial concentration of BMP, yet was still within the range of BMP values obtained in the simulations in Chapter 3. We also note that these boundary conditions are identical to those used in Chapter 3, with the exception of this source of BMP at the bone surface.

The initial conditions include a uniform distribution of progenitors across the domain, with no differentiated osteoblasts. This gives the initial condition for the cells as

$$P(x, y, 0) = 0.8 \times 10^{6}\,\mathrm{cells\,ml^{-1}}, \qquad O(x, y, 0) = 0\,\mathrm{cells\,ml^{-1}}. \tag{4.6}$$

Previously to find the initial conditions for the chemical species we used the steady state value for the concentrations given the cell density of progenitor cells and osteoblasts. However there is a degeneracy in Equations (4.3) and (4.4) when $O = 0$. To overcome this we take to initial condition for the chemical species to be the steady state when $P = 0.8 \times 10^{6}\,\mathrm{cells\,ml^{-1}}$ and $O = 0.01\,\mathrm{cells\,ml^{-1}}$. This gives the following uniform initial conditions for the chemical species

$$B(x, y, 0) = 2.77 \times 10^{-7}\,\mathrm{g\,ml^{-1}}, \qquad N(x, y, 0) = 0.077 \times 10^{-7}\,\mathrm{g\,ml^{-1}}. \tag{4.7}$$

We note that unlike in the previous simulations in Chapter 3 we include no noise in our initial condition. Instead the BMP source on the left boundary is sufficient to initiate pattern formation.

4.1.1 Finding the Wave speed in 1D

In the first instance we attempted to measure the wave speed for a 1D domain. We solved Equations (4.1)-(4.4) with zero flux boundaries for all species except for BMP, where we introduced a source on the left boundary $\bar{B}(0, t) = 5$. The initial conditions were as in Equations (4.6) and (4.7) and all other parameters used were as listed in table Table 3.1. In order to view the propagation of the wave over a longer time period, so that the wave speed could be more

accurately measured, we extended the spatial domain to a length of $L_x = 1\,\text{cm}$. As in Chapter 3, the numerical approach used to solve these equations was the MATLAB (Release 2012b) function `pdepe`, a numerical solver for parabolic or elliptical PDEs in one spatial dimension.

In this chapter we consider a specific set of parameters that we have previously shown could give rise to patterns across the domain. This is not the only parameter choice that could give rise to patterning, and in Chapter 3 we discussed some of the factors relating to the parameter space for pattern formation and the implications of this parameter space on our model. It is reasonable to expect that a different choice of parameters will give rise to a pattern formation front with a different wave speed. However we are not interested in establishing the wave speed as a function of these parameters or in conducting a sensitivity analysis. Rather we wish to determine the wave speed as a precursor to establishing the phenomenological effect of a growing domain on our model.

Figure 4.2 shows the evolution of the pattern for the BMP concentration and osteoblast populations. Initially there is a spatially homogeneous distribution of all species. The source of BMP at the boundary $x = 0$ initiates the formation of a Turing patterning process in the chemical species. As time progresses the patterning spreads across the domain. We observe that individual peaks and troughs remain static and are not moving across the domain, rather the propagating front represents the division of the domain between a region where patterning has occurred and a spatially homogeneous region. In Figure 4.2(b) we see the evolution of the pattern for BMP across space and time. We see that the velocity of the front appears to remain at a relatively constant speed of $0.37\,\text{cm}\,\text{day}^{-1}$, and that the frequency of the evolved pattern appears to remain constant. We note that after about 2 days the front of pattern formation disappears and the pattern evolves uniformly across the remainder of the domain. We remind ourselves that the spatially homogeneous initial conditions are unstable, due to the Turing-like kinetics for BMP and noggin. The timing of the appearance of patterning in this region is consistent with the timing of the evolution of pattern observed in the case of zero flux boundary conditions and spatially homogeneous initial conditions, such as the simulations in the previous chapter. Thus the patterning in this region does not evolve as part of the patterning front, rather in this region the patterns

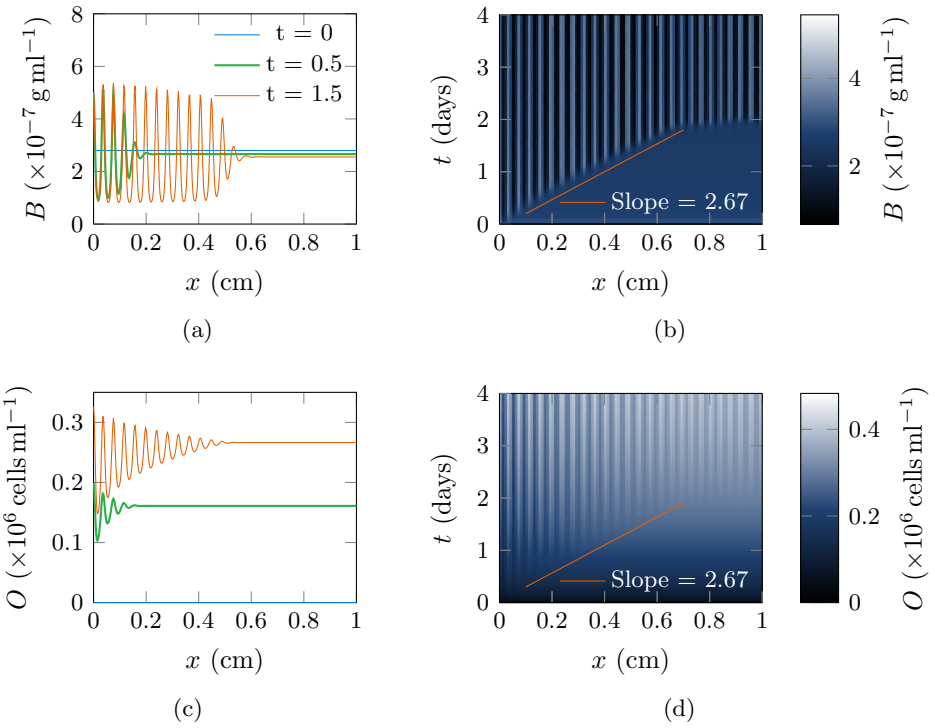

Figure 4.2: Concentration and cell density over time for BMP and osteoblasts showing the front of pattern initiation. (a) Concentration profiles for BMP over time. (b) Space-time evolution of BMP concentration, the orange line represents the position of a front moving with speed 0.37 cm day^{-1}. (c) Cell Density profiles for the osteoblast population over time, as expected we see that osteoblast differentiation lags the BMP patterning process. (d) Space-time evolution of osteoblast cell density, the orange line represents the position of a front moving with speed 0.37 cm day^{-1}.

simply emerge due to the instability of the initial conditions.

We see that the differentiation of the progenitor cells into osteoblasts follows the chemical pre-pattern. As expected, the appearance of patterning in the cells lags that of the chemical species. As the cellular species differentiate at a slower speed compared to the chemical reactions the front is less defined, however it seems to travel at a similar speed to the chemical pattern front. We see that the magnitude of the pattern is larger and that the troughs are lower near the left hand boundary then near the wave front. Indeed this effect is apparent even after the patterning has evolved across the entire domain. There are two causes for this. Firstly, the cells on the left have been exposed to the chemical pre-pattern for longer, resulting in the larger magnitude. The second,

is that over time the osteoblast population is increasing due to differentiation, even in the non-patterned region. The longer it takes for the chemical pre-pattern to reach a point, the higher the osteoblast population will be at the commencement of patterning. This, in particular, affects the height of the trough. Over the course of the simulation the differentiation of progenitors to osteoblasts always exceeds the death of osteoblasts, thus even in the troughs the population is still increasing. This means that in regions where there is a higher level of osteoblasts at the onset of patterning the troughs will naturally start at a greater height then those to the left.

4.1.2 Finding the Wave Speed in 2D

Having determined the wave speed for the 1D case we now turn to a 2D domain as illustrated in Figure 4.1. As in Chapter 3 we used the finite volume method to solve Equations (4.1)–(4.4) numerically. The boundary conditions used are zero flux for all species on all boundaries except for BMP on the left boundary, where the condition was $B(0, y, t) = 5 \times 10^{-7}\,\mathrm{g\,ml^{-1}}$ and the initial conditions were as in Equations (4.6) and (4.7). A domain size of $L_x = 0.2\,\mathrm{cm}$ and $L_y = 0.2\,\mathrm{cm}$ was used.

In Figure 4.3 we show the distribution of BMP concentration and osteoblast density at times $t = 0.5, 1.2$ and $2\,\mathrm{days}$. Looking first at BMP we see that there are now two fronts of patterning. Initially the BMP source across the left boundary drives the emergent pattern to appear in vertical stripes. However these stripes are unstable and over time further evolve to become spots, giving a second front of patterning. This effect is much more apparent in the profiles for BMP, however we see for the osteoblasts that by day 2 the stripes are starting to evolve into spots. We see that this progression from stripes to spots results in a final pattern where the spots are aligned vertically and staggered horizontally in adjacent columns.

To determine the wave speed we use a similar approach as for the 1D results. We took a cross-section of the solution across $y = 0.1\,\mathrm{cm}$ and used this to form the images shown in Figure 4.4. This image allows us to clearly see both the front of the stripe pattern formation as well as the front for the development of spots in the BMP concentration. We see that the stripe formation spreads quickly across the domain at a speed similar to that of the 1D case. The spot formation lags the stripe formation by about a day but the front appears to

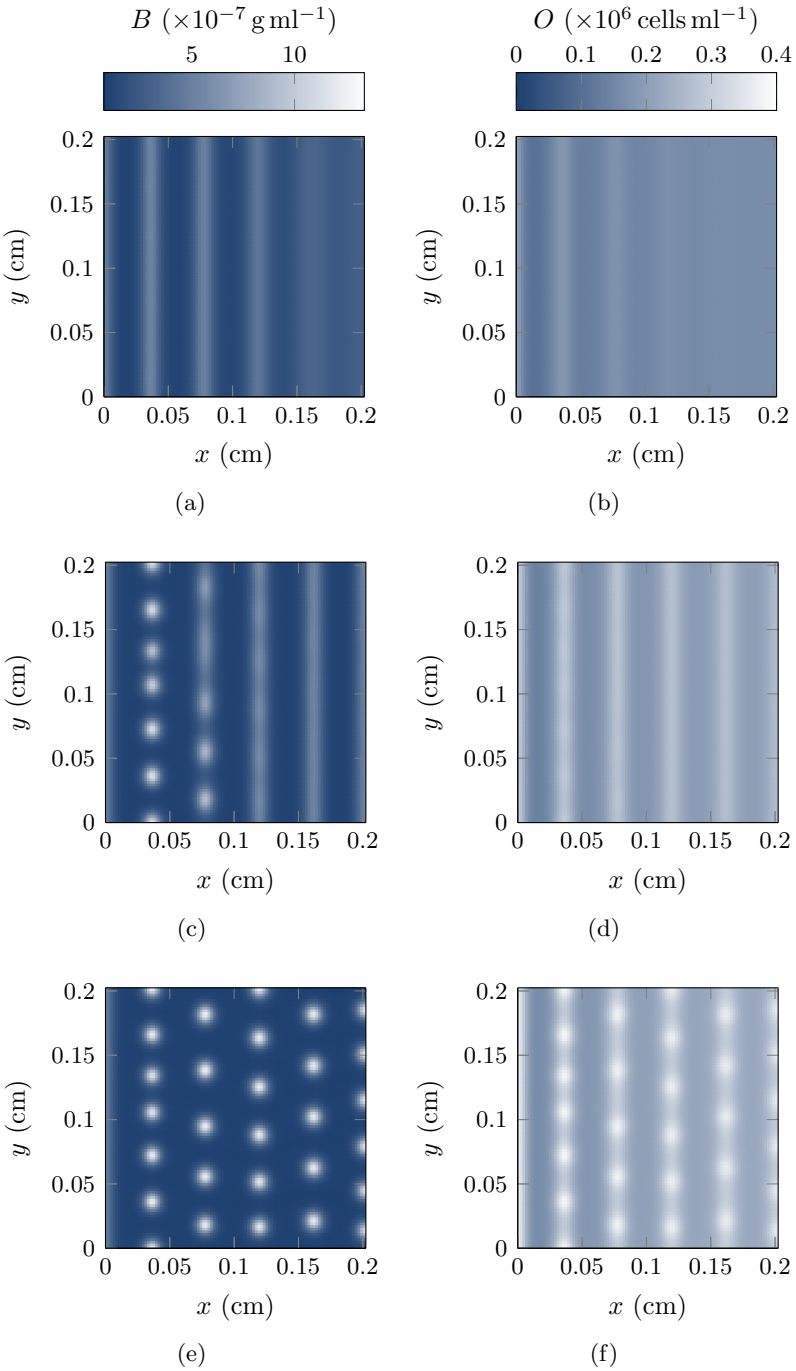

Figure 4.3: Concentration profiles for BMP (left column) and osteoblasts (right column) showing propagation of the differentiation front. Profiles are shown at times $t = 0.5$ days (top row), $t = 1.2$ days (middle row) and $t = 2$ days (bottom row). The pattern first spreads across the domain as a series of stripes, and then further evolves to a spotted pattern.

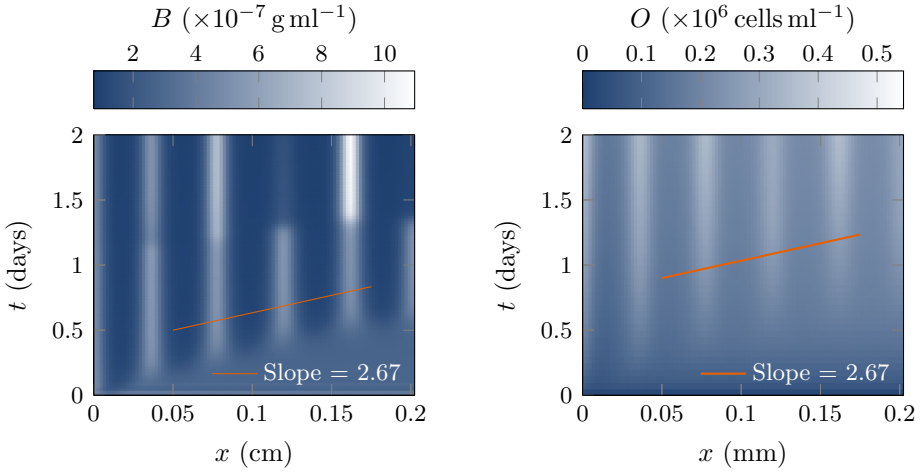

Figure 4.4: Space-time evolution along the line $y = 0.1\,\text{cm}$ for (a) BMP and (b) osteoblasts. The orange line indicates the position of a front corresponding to a speed of $0.37\,\text{cm}\,\text{day}^{-1}$. For BMP we see that both fronts appear to travel at this speed. For the osteoblasts the fronts are less clear, however they appear to also be travelling at the this speed.

travel at the same speed. For the osteoblasts the stripe formation is clearly apparent, however the subsequent development of spots is less clear. As was the case with the 1D simulations the front of cellular differentiation lags the mineralisation front but still appears to move at roughly the same speed.

Both the 1D and 2D simulations have predicted a speed of the front of differentiation of around $0.37\,\text{cm}\,\text{day}^{-1}$. Based on the measurements of an ovine fracture callus after 2 weeks the callus has grown to a width of approximately 0.5 cm (Manjubala et al. 2009). Thus the speed of the differentiation front is much faster then the speed at which the callus is growing.

4.1.3 Effect of Partial BMP Source at the Bone Surface

Having established an approximate wave speed of pattern formation we take a slight detour and turn our attention to a variation of the previous 2D simulations. When bone is damaged BMP is released from the bone extra cellular matrix into the fracture callus. It is likely that only the bone nearest the fracture gap sustains enough damage to act as a BMP source.

To include this effect in our model we designate the top of our domain to

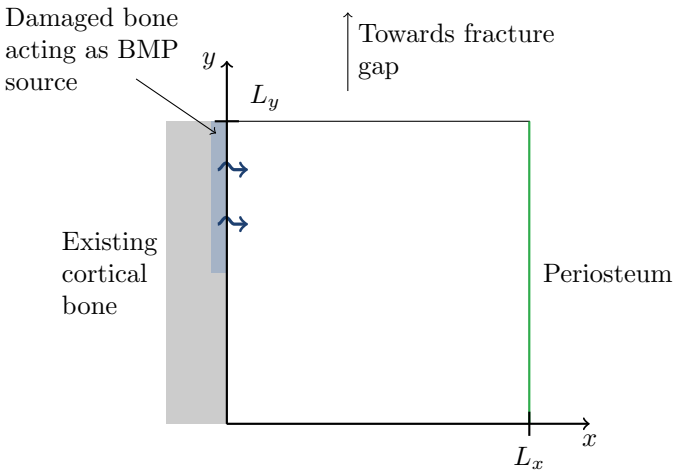

Figure 4.5: Schematic of the domain with a BMP source on the top half of the left boundary.

be nearest to the fracture gap, such that our domain could be considered a simplified view of the fracture callus as shown in Figure 1.2. We then change the left hand boundary condition so that only the top half of the boundary acts as a BMP source, as illustrated in Figure 4.5. The boundary condition for BMP on the left boundary can be written as

$$\begin{aligned} B(0,y,t) &= 5\times10^{-7}\,\mathrm{g\,ml^{-1}}, && y > 0.1\,\mathrm{cm},\\ \frac{\partial B(0,y,t)}{\partial x} &= 0\,\mathrm{g\,ml^{-1}\,cm^{-1}}, && y \le 0.1\,\mathrm{cm}. \end{aligned} \tag{4.8}$$

All other boundary and initial conditions were as in Section 4.1.2.

The results for these simulations are seen in Figure 4.6. We see that the initial front has a stripe like appearance but that this very quickly evolves into a spotted pattern. The initial stripes propagate horizontally along the top half of the domain but spread in a radial fashion in the bottom half of the domain. This affects the eventual pattern of the spots. In the top half of the domain the spots appear to be more regularly distributed in the horizontal direction, whereas in the lower half the spots are less aligned. The spots of high osteoblastic differentiation are sites where new bone would be expected to appear, and the distribution of these spots would influence the spicule growth that occurs in new intramembranous bone. The distribution of spots that emerges reflects an aspect of the appearance of new intramembranous bone in the fracture callus, such as that seen in Figure 4.7. In the regions of the callus closest to the fracture gap many of the bony spicules appear to be

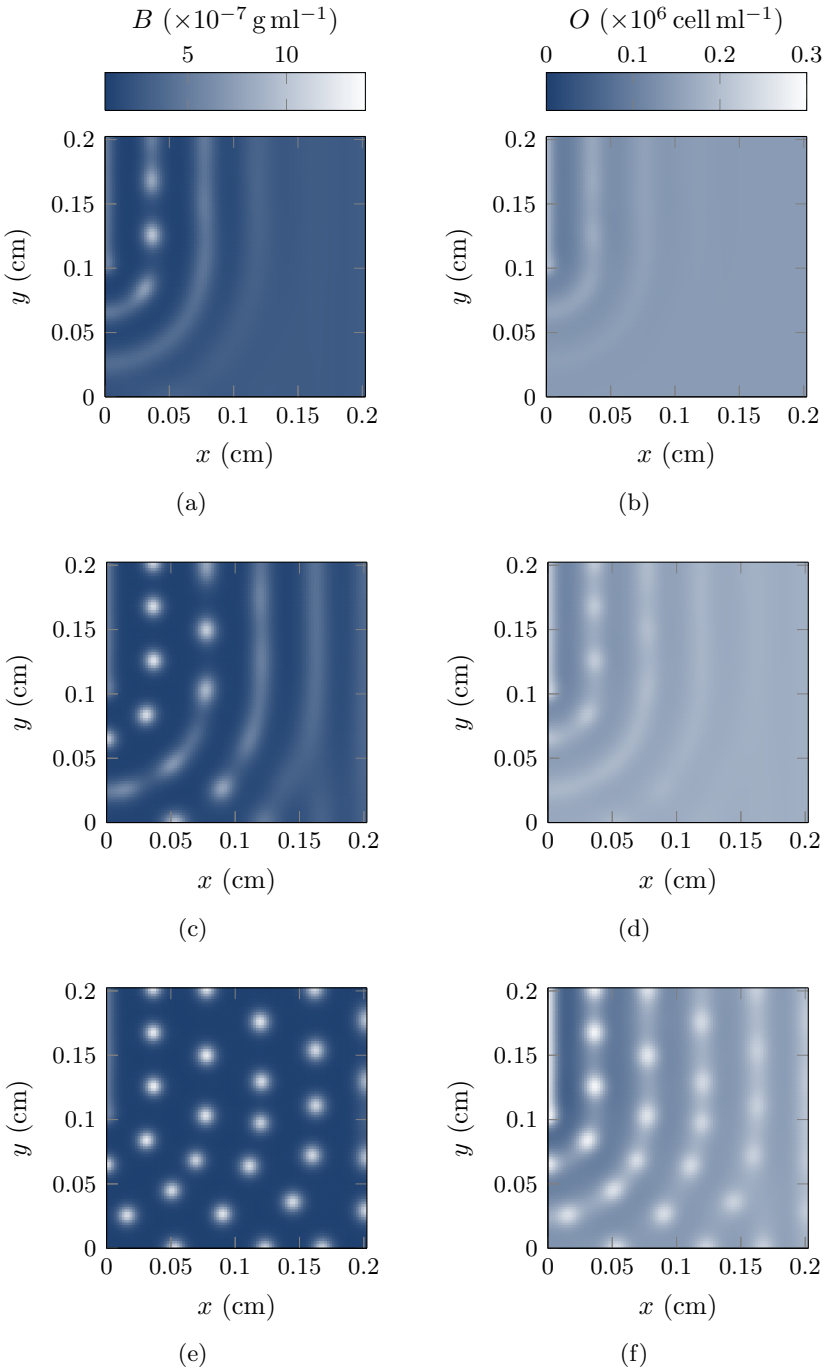

Figure 4.6: Concentration profiles for BMP (left column) and osteoblasts (right column) showing the effect of a source of BMP across the top half of the left boundary. Profiles are shown at times $t = 0.4$ days (top row), $t = 0.6$ days (middle row) and $t = 1$ days (bottom row). The pattern no longer emerges with an initial stripe formation.

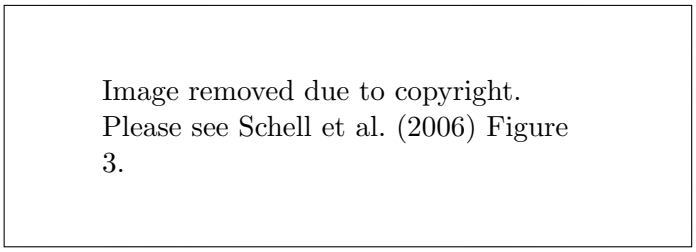

Figure 4.7: Histological section showing new intramembranous bone formation. The section is from a sheep, taken two weeks after a tibial osteotomy (Schell et al. 2006). The black rectangular regions are the pre-existing cortical bone, the irregularly patterned black material in the regions adjacent to the cortical bone is the new intramembranous bone. The white region is bone marrow and the pink regions are fibrous tissue. We can observe that near the fracture gap the spicules are aligned perpendicular to the existing cortical bone surface, but removed from the gap they appear to be aligned parallel to the bone surface.

aligned perpendicular to the existing bone surface. Removed from the gap the spicules align parallel with the bone surface. In between there is a transition zone where the spicules are not so clearly aligned.

4.2 Extension to Growing Domain

During fracture healing the callus region grows. We now incorporate this callus growth into the model. In this section we consider that the growth of the domain is solely due to the proliferation of progenitor cells located at the periosteum. Our new growing domain is illustrated in Figure 4.8. As a first approximation we assume that the cells present in the periosteum on the boundary of the callus are proliferating at a constant rate. Following this assumption, we model the growth of the callus as occurring at a constant rate as,

$$\frac{\mathrm{d}L_x}{\mathrm{d}t} = \rho. \tag{4.9}$$

As before on the left boundary, we have a source of BMP and all other species are zero-flux. On the top and bottom boundaries we have zero flux for all species. However on the right boundary we change the conditions to reflect that this boundary represents the periosteum. We assume that at the periosteum there is a constant density of progenitor cells, and that there are no osteoblasts. We also assume that the periosteum is impermeable to BMP and noggin and model this as zero-flux and the specific form of these boundary conditions is derived from a conservation of mass argument. This gives the

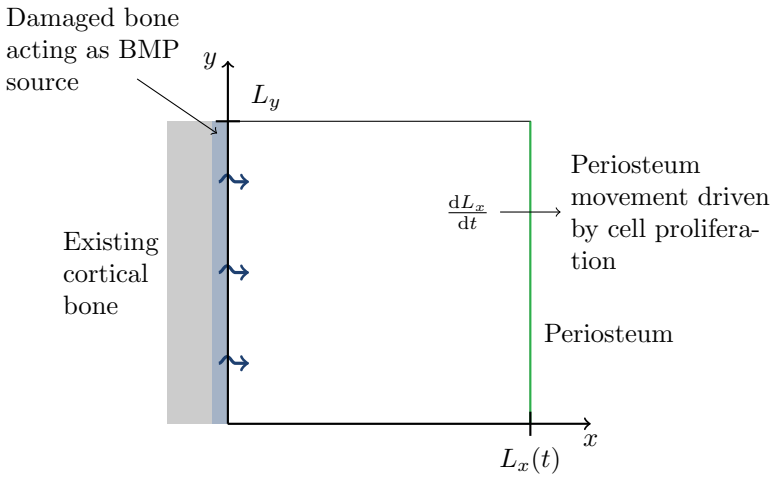

Figure 4.8: Schematic of the domain when a moving boundary is considered. The right boundary at $L_x(t)$, representing the periosteum, moves to the right due to the proliferation of progenitor cells present at the periosteum.

boundary condition at $x = L_x$ as

$$\begin{aligned} P &= 0.8 \times 10^6, & O &= 0, \\ \frac{\partial B}{\partial x} &= -\frac{\rho}{D_B} B, & \frac{\partial N}{\partial x} &= -\frac{\rho}{D_N} N. \end{aligned} \tag{4.10}$$

Converting these boundary conditions to non-dimensional forms using the relationships in Chapter 3 gives

$$\begin{aligned} \bar{P} &= 0.8, & \bar{O} &= 0, \\ \frac{\partial \bar{B}}{\partial \bar{x}} &= \frac{\bar{\rho}}{\bar{D}_B} \bar{B}, & \frac{\partial \bar{N}}{\partial \bar{x}} &= \frac{\bar{\rho}}{\bar{D}_N} \bar{N}, \end{aligned} \tag{4.11}$$

and the speed of the boundary becomes

$$\frac{\mathrm{d}\bar{L}_x}{\mathrm{d}\bar{t}} = \bar{\rho}, \tag{4.12}$$

where $\bar{\rho} = \hat{t}\rho/\hat{x}$.

We use initial conditions as in Equations (4.6) and (4.7) and take an initial domain width of $L_x(0) = 0.02\,\mathrm{cm}$.

4.2.1 Numerical Methods

The inclusion of a moving boundary introduces new challenges in obtaining a numerical solution. The full details of the numerical scheme are provided

in Appendix C, but we will provide a short description here. The domain is rescaled spatially to transform it to a static domain. We then take the rescaled equations and rewrite them in conservative form. This allows us to use the finite volume method to perform the spatial discretisation. We note that the rescaling introduces an advective flux into our system of equations and we use van Leer flux-limiting to compute the advective terms. We then use the inbuilt MATLAB (Release 2012b) solver `ode15i` to perform the time integration.

4.2.2 Results

The speed of the front of differentiation was previously computed as approximately $0.37\,\mathrm{cm\,day^{-1}}$, which is much faster than the rate of callus growth. We initially took the callus growth rate to be a tenth of the speed of the differentiation front $\rho = 0.037\,\mathrm{cm\,day^{-1}}$. This would result in a total callus width $0.518\,\mathrm{cm}$ after 2 weeks which would seem reasonably consistent with callus geometry observed in sheep at this time point (Manjubala et al. 2009).

We show the profiles for BMP concentration and osteoblast density at times $t = 1$, 3, and 5 days in Figure 4.9. We observe that a Turing pattern does indeed evolve over time as the domain grows and the resulting pattern features rows of spots that are roughly vertically aligned, and that the spots are staggered in adjacent rows. In Turing patterning processes the domain size has an influence on the final pattern achieved and in our results we see that the domain length is the key determinant in the number of rows of spots apparent.

As usual the patterning in the osteoblasts lags the patterning in the BMP. This allows the spotted pattern in the BMP to become well established before significant cellular differentiation can occur. The result of this is that the spots of high osteoblastic differentiation are well defined, compared to our previous results with a BMP source on a static domain. This well defined spotted patterning may help define the form of the new intramembranous bone. New bone is produced by osteoblasts, so it would be expected that patterning in the osteoblast population would affect the location and direction of new bony spicule growth, and hence define the appearance of the new woven bone.

Observing the progression of the BMP concentration we see that in the early stages the domain is not large enough in the horizontal direction to accommo-

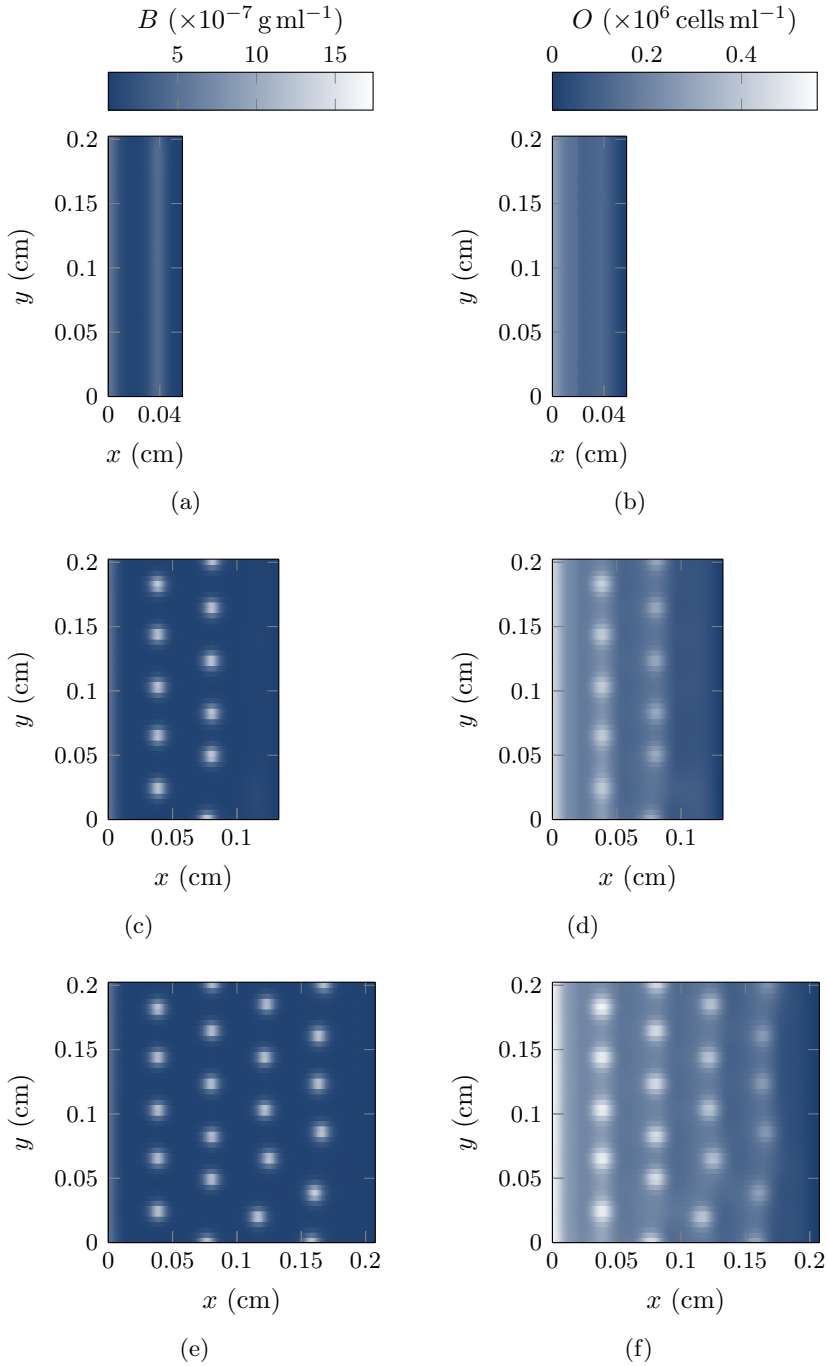

Figure 4.9: Concentration profiles for BMP (left column) and osteoblasts (right column) showing the effect of domain growth on cellular differentiation. Profiles are shown at times $t = 1$ days (top row), $t = 3$ days (middle row) and $t = 5$ days (bottom row). We see the emergence of well defined spots of osteoblastic differentiation.

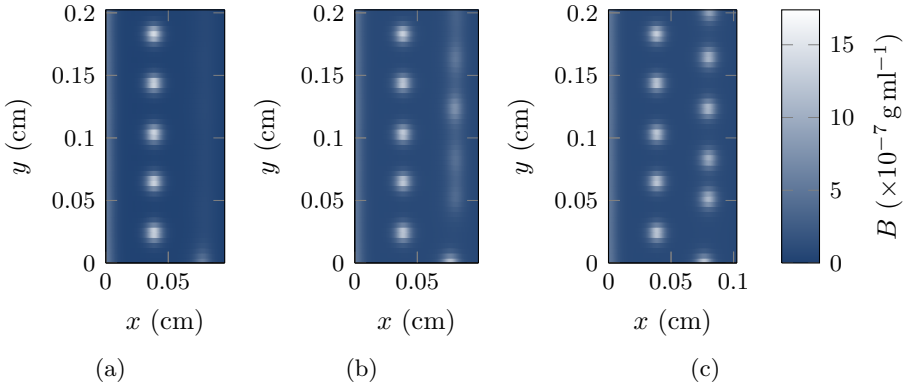

Figure 4.10: Concentration of BMP at times t= 2, 2.1 and 2.2 days demonstrating the evolution of the second column of spots. We see the transient stripe-like structure which quickly breaks down into individual spots.

date any patterning. Once the domain grows to a sufficient size we see the first signs of a pattern evolve. As before, the initial patterning appears as a transient vertical stripe, before evolving into a series of spots. It would perhaps be reasonable to expect that this is how the rest of the pattern evolution occurred, with a new stripe appearing as the domain grows long enough for it to fit before further breaking into spots, however this is not what occurs. Instead the spatial conditions have a further influence of the form of the patterning. We turn our attention to how the second row of spots evolves, illustrated in Figure 4.10. Examining the progression along the lower boundary, we note that the first row of spots does not have a spot on the boundary. As the domain grows there becomes enough room for a spot to begin to appear in the lower right corner, before the domain becomes long enough to fit another stripe. This prevents a second stripe from evolving, instead the second row of spots forms with the appearance of some shortened stripe-like structures that are highly unstable and quickly become spots.

As the domain continues to grow each new row of spots evolves in a similar fashion. An individual spot may evolve if the patterning in the previous row provides a suitable gap or short stripe-like structures appear and quickly evolve to become spots. As the stripe like structures are only apparent for a short period of time, they have little effect on the observed cell differentiation. This gives rise to the well defined spots in Figure 4.9.

Effect of Increasing the Rate of Growth of the Domain

Within our modelling framework the growth rate of the domain is related to the rate of proliferation of the progenitor cells present in the periosteum. It is of interest to determine how a faster domain growth, due to say increased cell proliferation would influence the patterning of our model.

To do this we take an extreme case, increasing the rate of domain growth to match the approximate speed of the patterning front. We set the rate of domain growth to $\rho = 0.37\,\mathrm{cm\,day^{-1}}$ and all parameters, boundary and initial conditions were kept the same as in the previous simulations. The results are shown in Figure 4.11. We observe that with the faster speed of domain growth the initial pattern again becomes a stripe formation, with the evolution of spots following. Comparing the final form of the pattern with that observed in the previous simulations we observe that the horizontal frequency of the spots appears to be slightly increased with the increased growth rate. We also observe that with the greater growth rate the spots are now aligned horizontally rather then the staggered nature seen with the slower growth rate.

4.3 Summary

We have presented a model of cellular differentiation in which we assumed that the differentiation was due to a underlying chemical pre-pattern. This pre-pattern was generated through a Turing pattern mechanism. It is well known that domain size and boundary conditions have a strong influence on the appearance of Turing patterns, and hence it was of interest to determine the influence of more physically realistic domain information had on the evolution of patterning in the cellular species.

By first introducing a source of BMP on the left boundary representing a release of BMP from the damaged bone we determined that the speed of the front of differentiation was around $0.37\,\mathrm{cm\,day^{-1}}$. This speed is much faster then the expected growth of the callus region.

When our model was then simulated on a growing domain with a growth rate consistent to that observed experimentally, we observed that a well defined pattern of spots evolved in the osteoblast population. This was due to the fast speed of pattern propagation compared to the domain growth rate. As the chemical patterning spreads quickly throughout the domain it allows for well

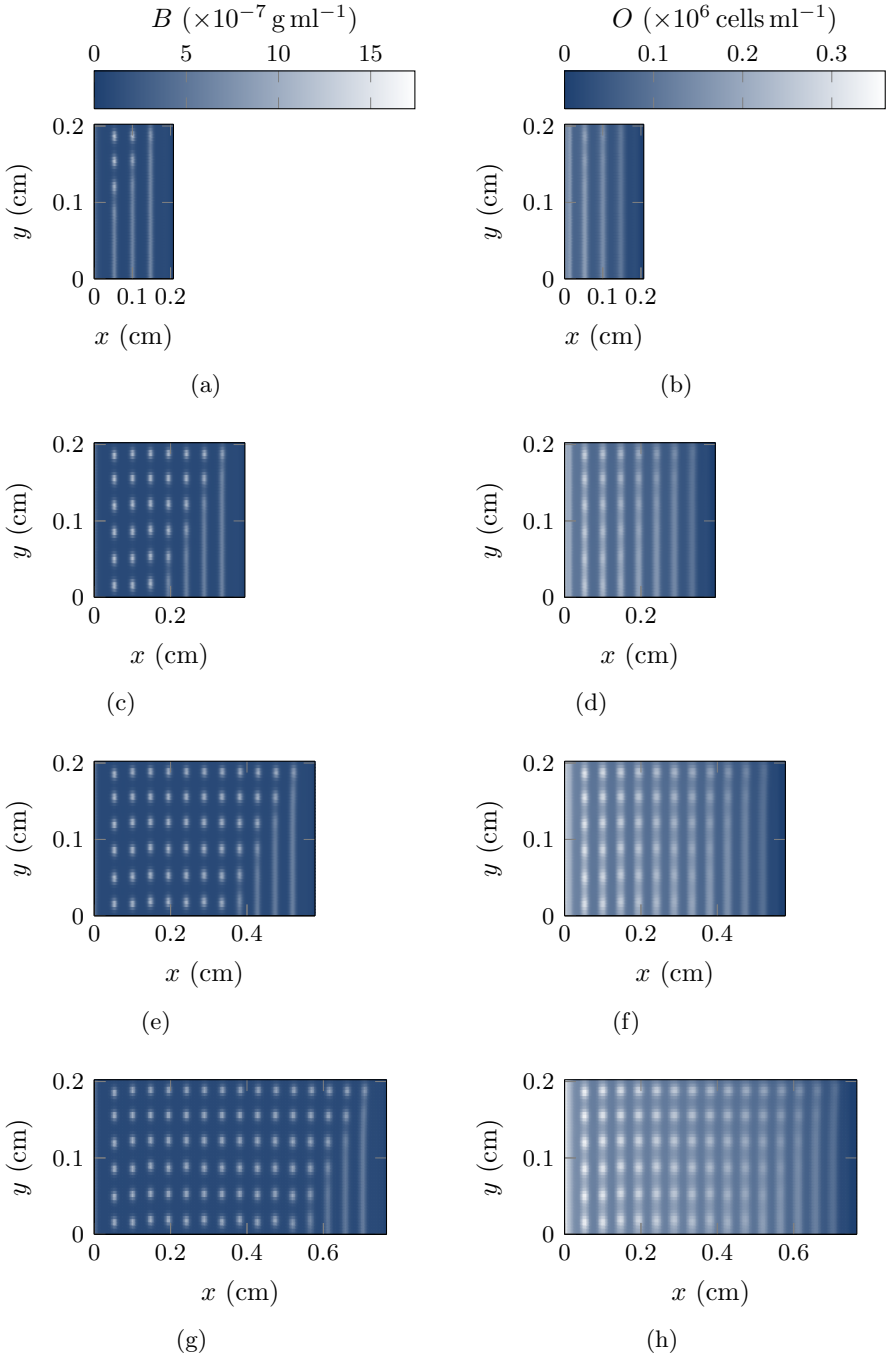

Figure 4.11: Concentration profiles for BMP (left column) and osteoblasts (right column) showing the effect of an increased rate of domain growth on cellular differentiation. Profiles are shown at times $t = 0.5$ days (top row), $t = 1$ days (second row), $t = 1.5$ days (third row) and $t = 2$ days (bottom row). We see that the stripe formation is again apparent and that the spots are aligned horizontally, as opposed to the slower domain growth where the spots where staggered.

defined patterning in the osteoblast population. As osteoblasts are directly responsible for creating new bone tissue, this patterning in the osteoblast population could have an effect on the resultant structure of the newly formed intramembranous bone.

Another interesting result was observed when a source of BMP was only applied to half of the left boundary. The resultant distribution of the spotted patterning in the cellular species was in some ways similar to the structural patterning observed in the new intramembranous bone. This indicates that the chemical signals released from the bone during trauma, as well as signals originating from the fracture gap may play an important role in the heterogeneity of the structure of the new intramembranous bone.

5

A Mathematical Model for the Mineralisation of New Bone Tissue

In our overall view of the process of intramembranous bone formation during fracture healing we consider three separate regions: a proliferative region near the periosteum were new osteoblast progenitor cells proliferate; a region of cellular differentiation where the progenitor cells differentiate to become mature osteoblasts in response to a chemical signal; and a mineralisation region where the newly differentiated osteoblasts act to produce new mineralised bone. In the previous chapters we have created a model for the cellular differentiation region and included the impact of the proliferative region, modelled as domain growth. This model led to a patterned distribution of pools of differentiated osteoblasts amongst less differentiated cells. The underlying assumption was that in regions with a high osteoblast population density mineralisation will occur, and that the spatial distribution of these pools of osteoblasts would influence the structural form of the new intramembranous bone in the callus. We now turn our attention to building a mathematical model to examine how this mineralisation process is regulated.

A common approach used in the bioregulatory models of fracture healing by Bailón-Plaza & van der Meulen (2001) and Geris et al. (2006) is that the rate of formation of new mineralised bone tissue is modelled as being proportional to the osteoblast population density, with the rate decreasing as the local tissue density increases. A similar concept is used in a model of the bone multicellular unit (BMU) during remodelling, where the rate of bone formation decreases as the radius of the osteon (Buenzli et al. 2014). Other similar models take an even simpler approach and model the rate of bone formation as simply proportional to the osteoblast cell density (Ryser et al. 2009, Pivonka et al. 2008).

In our modelling of the new bone formation process we aim to take a different approach. We aim to explore what additional factors may act to be regulating osteoblast production of new bone. In a model by Moreo et al. (2009) for bone ingrowth into implants new bone formation was influenced by the presence of two generic growth factors. They also explicitly tracked the movement of the bone surface. We take this approach of explicitly modelling the bone surface, but instead create a mathematical model for bone mineralisation that considers the influence of the regulatory loop between alkaline phosphatase and pyrophosphate on mineralisation.

In our model for mineralisation we assume a homogeneous distribution of cells across the domain. This is in contrast to our previous models for cell differentiation where we demonstrated the potential for heterogenous cell populations to develop. In this work we simplify to a homogeneous cell population in order to decouple the development and analysis of the mineralisation model from the additional complexities that would arise from the inclusion of a heterogeneous domain. We recognise that a heterogeneos cell population would be more physically realistic and discuss some of the difficulties that could arise and potential approaches to solve them in the Future Work section of this thesis (Section 6.2).

5.1 Mineralisation of Bone Tissue

Mineralised tissues such as bone and teeth consist of an organic matrix, mostly formed from collagen, and inorganic mineral crystals which form around the collagen fibrils. The deposition of the minerals onto the collagen matrix is known as mineralisation, or sometimes as calcification, because of the high content of calcium in the mineral. In healthy individuals mineralisation is confined to bone and teeth and this desired mineralisation is referred to as being physiological. It is also possible for pathological mineralisation to occur in other soft tissues such as osteoarthritis where the cartilage present in joints calcifies, or the calcification of arterial walls. Whilst the mechanisms that control physiological and pathological mineralisations may not be identical it is likely that there are some common processes that allow mineralisation to occur. Thus insights into physiological mineralisation could also provide insights to pathological mineralisation and vice versa. Whilst we focus on the mineralisation of bone during fracture healing, many of the ideas discussed

could be applied to mineralisation as it occurs during bone remodelling or tooth formation, or even pathological mineralisation.

Bone tissue consists of an organic matrix of mostly collagen that has been mineralised with crystalline hydroxyapatite. As a composite material bone is both rigid, due to the presence of mineral, and resistant to fracture, due to the collagen matrix which increases the toughness (Fratzl et al. 2004). The organic component of bone is about 90% collagen I, and the rest is other non-collagenous proteins. These non-collagenous proteins play many roles, including assisting in the regulation of the deposition of mineral onto the matrix (Boskey & Robey 2013). Hydroxyapatite ($Ca_{10}(PO_4)_6(OH)_2$) crystals form the mineral component of bone however it contains many mineral impurities such as magnesium, fluoride and carbonate. As well as providing the stiffness of the bone, it provides the body with a store of calcium and phosphate that can be accessed if required (Boskey 2001).

In humans, mineralisation is restricted to bone and teeth. It is commonly stated that mineral concentrations of calcium and inorganic phosphate (P_i) are sufficiently high in the extracellular fluid for mineral crystals to form. This helps explain why bone and teeth don't spontaneously dissolve but it raises another question about why our bodies aren't calcified statues. One contributing factor to this, that is supported by both *in vivo* and *in vitro* experiments, is that the presence of mineralisation inhibitors prevent pathological mineralisation from occurring. For example in mice models, mice without the genes associated with known mineralisation inhibitors exhibit excessive pathological mineralisation, often with fatal results (Murshed et al. 2005). It has also been observed in humans that mutations in genes related to known inhibitors can lead to arterial calcification (Rutsch et al. 2003) and osteoarthritis (Suk et al. 2005). The presence of these mineralisation inhibitors throughout the extracellular space means that mineral forming cells such as osteoblasts and odontoblasts (tooth forming cells) must possess mechanisms for removing the inhibitors from the local environment.

5.1.1 The Role of Osteoblasts in Mineralisation

Osteoblasts, and the osteoblast derived cell type osteocytes, play many important roles in the initiation and regulation of bone tissue formation and mineralisation. These include producing the collagen matrix, producing ma-

trix vesicles to initiate crystal formation and producing enzymes that can remove mineralisation inhibitors.

Osteoblasts produce and arrange the extracellular collagen matrix of bone. As the collagen matrix is formed some of the osteoblasts become trapped in the matrix and become osteocytes. Osteocytes help control and regulate the subsequent mineralisation of the collagen (Franz-Odendaal et al. 2006).

As the collagen fibres are produced they are arranged in a staggered array. This array structure is particularly conducive to mineralisation. The gaps between fibres, known as the hole zones, contain proteins that help attract and bind mineral ions to the matrix. These hole zones are the first sites where mineralisation appears, and from here it propagates along the fibres (Nudelman et al. 2010, Mann 2001).

The deposition of hydroxyapatite crystals in the hole zones of the collagen matrix is facilitated by extracellular organelles known as matrix vesicles, although the precise nature by which this occurs is unknown. Matrix vesicles are produced by osteoblasts and immature osteocytes by a budding process of the plasma membrane (Xiao et al. 2007, Golub 2009). The membrane of the vesicle contains a high number of calcium pumps, such as annexin II,V,VI (Kirsch, Harrison, Golub & Nah 2000), which act to increase the local calcium concentration inside the vesicle. At the same time the concentration of phosphate ions is also increased inside the vesicle via sodium/phosphate cotransporters (Montessuit et al. 1991, Kirsch 2006). The high concentrations of calcium and P_i ions inside the vesicle allow small hydroxyapatite crystals to nucleate and quickly grow. As the crystals grow even larger they eventually protrude from the vesicle into the extracellular space and continue to propagate there.

How the hydroxyapatite crystals contained within the vesicles become attached to the collagen matrix is still unknown. One theory is that when the vesicles break down, the crystal dissolves and the local extracellular concentration of ions is increased. These ions bind at specific points on the collagen fibres which creates new nucleation points for mineral crystal formation (Mann 2001). Another hypothesis is that when the crystals are released from the vesicle they get stuck in the grooves in the collagen fibres, and that proteins present in the collagen and on the vesicle membrane help facilitate this process (Golub 2010).

5.1.2 Inhibition of Mineralisation

There is good evidence to suggest that mineralisation throughout the entire body is prevented by mineralisation inhibitors. In murine studies it has been shown that the removal of the genes related to known inhibitors results in excessive pathological mineralisation. Similarly, mice where the osteoblasts lack the ability to remove these inhibitors have insufficient mineralisation of bone tissue (Hessle et al. 2002, Harmey et al. 2004).

Two known strong mineralisation inhibitors are pyrophosphate (PP_i) and Matrix GLA protein (MGP). MGP is produced by vascular smooth muscle cells and chondrocytes. It has been shown that mice lacking MGP develop excessive arterial calcification and mineralisation of cartilage tissues shortly after birth leading to their death (Luo et al. 1997). MGP is not expressed by osteoblasts and hence is not likely to be influencing the mineralisation that occurs during intramembranous bone formation.

The potent mineralisation inhibitor PP_i is present in the extracellular fluid throughout the body (Fleisch & Bisaz 1962, Russell et al. 1971). The proteins related to the production of PP_i are produced by virtually every cell type in the body, but it is interesting to note that osteoblasts express high levels of these proteins (Murshed et al. 2005). PP_i inhibits mineralisation via at least 2 different mechanisms. One mechanism is that PP_i induces osteoblasts to express osteopontin, a late stage mineralisation inhibitor (Cowles et al. 1998, Harmey et al. 2004, Johnson et al. 2003, Addison et al. 2007). The other mechanism is that it binds to sites in the crystal lattice of the hydroxyapatite that should be occupied by an phosphate ion, which prevents further crystal growth (Addison et al. 2007). It is for this reason that it is believed that the ratio of PP_i to P_i is a more important determinant of whether mineralisation will occur rather then the absolute concentrations of either species (Murshed et al. 2005, Sapir-Koren & Livshits 2011, Terkeltaub 2001). This hypothesis is further supported by murine models which demonstrate that mice missing both the genes for PP_i expression and proper phosphate regulation have an almost normal level of mineralisation, whereas mice missing just one of these genes suffer severe mineralisation defects (Murshed et al. 2005).

5.1.3 Alkaline Phosphatase

Alkaline Phosphatase (ALP) is an enzyme that removes the phosphate group from molecules (Millán 2006). As the name suggests ALP is most effective in an alkaline environment (Fernley & Walker 1967, Holtz & Kantrowitz 1999). Substrates of ALP include adenosine triphosphate (ATP) and PP_i, although there are many others (Rezende et al. 1994). In humans there are four isozymes of ALP, however only one of these is relevant to bone repair. Osteoblasts produce the tissue non-specific form of ALP. Tissue non-specific ALP (TNAP) is also expressed in other tissues including the liver and kidneys (Millán 2006). TNAP exists in forms that are either bound to cell membranes or freely circulating. During bone formation the majority of TNAP is bound to the cell membrane of osteoblasts (and mineralising chondrocytes) and their matrix vesicles. Whilst free circulating TNAP will be present during bone repair, in healthy individuals the membrane bound TNAP is the main influence on mineralisation (Murshed et al. 2005).

The role of TNAP in mineralisation is to remove the mineralisation inhibitor PP_i. It has been demonstrated that osteoblasts that have been exposed to PP_i express higher levels of TNAP indicating a regulatory loop exists to keep PP_i levels in check (Addison et al. 2007). A beneficial side effect of this is that when TNAP acts on PP_i, it also raises the local P_i concentration. This new P_i can then be incorporated into the growing HA crystals.

5.2 A Model for Mineralisation

The regulatory loop between TNAP and PP_i during the mineralisation of tissue has been well studied in both *in vitro* cell assays and *in vivo* animal models. This has led to widely stated theory that the removal of PP_i by TNAP is a large contributing factor to bone mineralisation occurring. Furthermore to the best of our knowledge there has been no mathematical modelling of this system. For this reason we choose to build a mathematical model that examines the relationship between TNAP and PP_i. It has also been indicated that the concentration of PP_i in the extracellular fluid is of a lesser importance than its ratio with P_i. Thus we have included the concentration of P_i in our model as well.

The model that we present focuses on a particular aspect of new bone forma-

tion specifically how TNAP, PP_i and P_i interact to form an environment that is conducive to new mineral formation. At this stage in the development of the model we choose to ignore changes in cell populations, including the differentiation of osteoblasts to osteocytes, but are aware that these populations would have an effect on the speed at which mineralisation occurs, following from this we refer to all mineralising cells as osteoblasts for simplicity. In addition, we ignore the production of the collagen matrix and instead assume that the osteoblasts have produced a suitable collagen matrix that can be mineralised.

Furthermore, we ignore the effects of calcium in driving mineralisation. Calcium forms a major part of the mineral component of bone and as such plays an important role in mineral formation. However calcium homeostasis is also very important to many other systems within the body and hence is very tightly regulated through a series of mechanisms (Peacock 2010). This makes it very difficult to experimentally determine the effect of circulating calcium levels on mineralisation. Instead the influence of P_i on mineralisation has been far more widely studied both *in vivo* and *in vitro* due to the availability of suitable mouse models. Indeed it is curious to note that mineralisation is achieved *in vitro* by the addition of a phosphate source to the medium, rather than additional calcium (Birch & Wright 2013). We also note that the effect of calcium ion concentration was considered by Carlier et al. (2011), where the authors presented a modified version of the bioregulatory model for fracture healing presented in Geris et al. (2006).

In Figure 5.1 a diagram of the relationship between TNAP, PP_i and P_i is shown. In this figure we illustrate the key processes occurring that we aim to model. The mineralisation inhibitor PP_i is produced by the osteoblast. The osteoblast also produces the enzyme TNAP bound to its cell membrane. The TNAP cleaves the PP_i removing the inhibitor. Additionally as the PP_i is cleaved it results in two new P_i ions. Thus the cleaving action of TNAP both lowers the levels of inhibitor and raises the levels of P_i ions. A further description of these mechanisms is given below.

The mineralisation inhibitor PP_i is present in the extracellular fluid. Its presence in the extracellular space is regulated via two separate mechanisms within the osteoblasts. It is created internally within the cell and exported into the extracellular space via the ANK protein. It is also produced externally of the

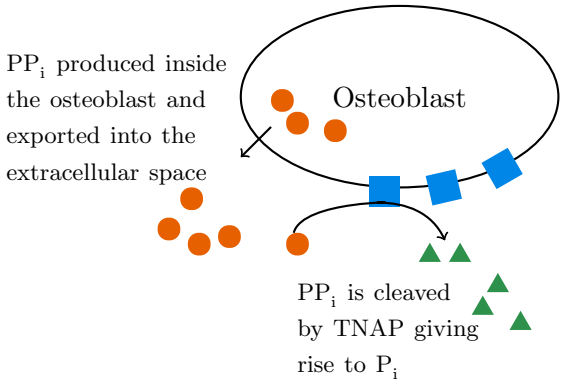

Figure 5.1: Illustration of the relationship of PP$_i$ and TNAP. The mineralisation inhibitor PP$_i$ (orange circles) is produced by osteoblasts and deposited into the extracellular space. The membrane bound protein TNAP (blue squares) cleaves the inhibitor PP$_i$, giving rise to extra P$_i$ (green triangles). This additional P$_i$ can be incorporated into the new hydroxyapatite crystals.

cell via the NPP1 protein embedded in the osteoblast cell membrane (Harmey et al. 2004, Terkeltaub 2001).

In order for mineralisation to proceed the PP$_i$ needs to be removed from the extracellular fluid. In bone formation this occurs through the actions of TNAP which cleaves the PP$_i$. TNAP is found both freely circulating in the extracellular fluid and bound to the cell membrane of osteoblasts, however in the context of bone formation in healthy individuals the membrane bound TNAP is believed to play the dominant role (Murshed et al. 2005).

The removal of PP$_i$ by TNAP plays another important role other than the removal of an inhibitor. As the PP$_i$ is cleaved it gives rise to P$_i$. This raises the local concentration of P$_i$ which can be incorporated into the growing hydroxyapatite crystal.

5.3 Kinetic Equations

We begin by constructing a set of kinetic equations to describe the relationship between TNAP, PP$_i$ and P$_i$. We introduce the variables A for TNAP (tissue non-specific **A**lkaline phosphatase), P for PP$_i$ (**P**yrophosphate – the mineralisation inhibitor) and I for P$_i$ (**I**norganic phosphate). At this stage of the modelling process we are interested in establishing the kinetic equations that describe the relationship between our three chemical species. We ignore spatial effects, such as diffusion and the influx or outflux of PP$_i$ and P$_i$ as they

freely circulate through the extracellular fluid. Doing this allows us to focus on the osteoblastic regulation of TNAP,PP_i and P_i concentration levels.

TNAP is produced by osteoblasts and remains bound to the cell membrane. There is evidence that cells cultured with increased PP_i have an increase in TNAP gene expression and activity (Addison et al. 2007). In addition we assume that TNAP has a constant rate of decay. Based on this we write an equation for TNAP mass concentration as

$$\frac{\mathrm{d}A}{\mathrm{d}t} = \alpha O + \beta APO - \delta A. \tag{5.1}$$

Here O represents the cell density of osteoblasts, and for this model we assume that the osteoblast population is not changing and hence that O is a constant. The parameter α is the baseline rate of production of TNAP by the osteoblasts, β is the rate of production of TNAP by the osteoblasts as increased by the presence of TNAP and PP_i and δ is the decay rate of TNAP.

Pyrophosphate is produced by all cells in the body as a by-product of respiration and through other processes. Interestingly mineralising osteoblasts produce PP_i at a rate greater then other cell types (Murshed et al. 2005). We model the production of PP_i by cells as a constant production by osteoblasts. It is widely assumed that ALP is a Michaelis-Menten like enzyme (Ciancaglini et al. 2010), thus we use a Michaelis-Menten type reaction to model the enzymatic cleaving of PP_i by ALP. In addition there is evidence that P_i is also a competitive inhibitor for this reaction (Cyboron et al. 1982). We write the equation for the molar concentration of PP_i as

$$\frac{\mathrm{d}P}{\mathrm{d}t} = \eta O - \frac{k_{\mathrm{cat}} AP}{K_M\left(1 + \frac{I}{K_I}\right) + P}, \tag{5.2}$$

where η is the production rate of PP_i by osteoblasts. The remaining parameters $k_{\mathrm{cat}}, K_M, K_I$ follow the standard definitions of Michaelis-Menten kinetics. The turnover number k_{cat} is the maximum number of substrate molecules cleaved per enzyme molecule per second. The Michaelis constant K_M is the concentration of substrate at which the reaction rate is half the maximum rate in the absence of inhibitor. The final parameter is the inhibition constant K_I.

For the phosphate equation we simply model the concentration changes due to the cleaving action of ALP. As the PP_i is cleaved two P_i ions are created. In this model we assume that the effect of cell phosphate consumption or production, and the removal of P_i as it becomes incorporated in the hydroxyapatite

Parameter	Value	Units	Dimensionless Value
O	10^6	$\text{cells}\,\text{ml}^{-1}$	
δ	0.36	day^{-1}	0.36
k_{cat}	51.84×10^{-3}	$\text{mol}\,\text{g}^{-1}\ \text{day}^{-1}$	518.4
K_M	150×10^{-9}	$\text{mol}\,\text{ml}^{-1}$	150
K_I	23×10^{-9}	$\text{mol}\,\text{ml}^{-1}$	0.023
A_0	30×10^{-6}	$\text{g}\,\text{ml}^{-1}$	3
P_0	1.8×10^{-9}	$\text{mol}\,\text{ml}^{-1}$	1.8
I_0	1.15×10^{-6}	$\text{mol}\,\text{ml}^{-1}$	1.15

Table 5.1: Table of parameters for mineralisation model.

crystal is negligible. Thus the equation for the molar concentration of P_i was given as

$$\frac{\text{d}I}{\text{d}t} = 2\frac{k_{\text{cat}}AP}{K_M\left(1+\frac{I}{K_I}\right)+P}. \tag{5.3}$$

The initial conditions are

$$A(0) = A_0, \qquad P(0) = P_0, \qquad I(0) = I_0. \tag{5.4}$$

Here we choose A_0, P_0, I_0 to be values within the normal serum range for these species. We assume that before $t = 0$ the cells are not mineralising and all species are at there normal levels. At $t = 0$ the cells become mineralising cells and begin producing high levels of ALP and PP_i as observed in mineralising cell cultures.

5.4 Parameter Values for Kinetic Model

Like many biological problems to which mathematical modelling is applied, some of the parameters can be found or estimated from the literature whereas for others this was not possible. In this model we were able to find or estimate all of our parameters from the literature except for three, α, β and η, which relate to the production of TNAP and PP_i by the cells. The remaining parameters are listed in Table 5.1 and we detail below how they were obtained.

As with our model for cellular differentiation, we assume a carrying capacity for the cells of $10^6\,\text{cells}\,\text{ml}^{-1}$ (Bailón-Plaza & van der Meulen 2001), and further assume that the cells are densely packed with $O = 10^6\,\text{cells}\,\text{ml}^{-1}$. The

decay rate δ was found from the half-life of the protein. TNAP is reported to have a half-life of 2 days, this corresponds to $\delta = 0.35\,\text{day}^{-1}$ (Millán 2006).

Next we determine the parameters for the equations for PP_i and P_i. The Michaelis-Menten kinetic parameters were found in the literature for purified mouse TNAP at physiological pH and temperature (7.4 and 37°C). The values reported were $k_{\text{cat}} = 51.91 \pm 0.65 \times 10^{-3}$ mols (g protein)$^{-1}$ day^{-1} and $K_M = 0.15 \pm 0.4 \times 10^{-6}\,\text{mol ml}^{-1}$ (Ciancaglini et al. 2010). Thus in our simulations we take $k_{\text{cat}} = 51.91 \times 10^{-3}\,\text{mols (g protein)}^{-1}\,\text{day}^{-1}$ and $K_M = 0.15 \times 10^{-6}\,\text{mol ml}^{-1}$. The inhibition constant is reported to have values in the range $K_I = 18 - 26.6 \times 10^{-9}\,\text{mol ml}^{-1}$ (Cyboron et al. 1982). In our simulations we use a mid-range value of $K_I = 23 \times 10^{-9}\,\text{mol ml}^{-1}$.

Finally we are left to determine the initial conditions for our model. As stated previously, it is intended that the initial conditions be representative of normal serum conditions experienced by non-mineralising cells. This allows us to observe the changes in the concentrations as induced by the mineralising cells. Standard serum concentrations of PP_i and P_i are readily available in the literature. The serum concentration of PP_i in healthy humans is within the range $0.64\text{-}2.96\times10^{-9}\,\text{mol ml}^{-1}$ (Psychogios et al. 2011). The serum concentration of P_i is $0.8\text{-}1.5\times10^{-6}\,\text{mol ml}^{-1}$ (Boron & Boulpaep 2003). Using this data we choose the initial conditions $P_0 = 1.8 \times 10^{-9}\text{mol ml}^{-1}$ and $I_0 = 1.15 \times 10^{-6}\text{mol ml}^{-1}$.

The concentration levels of TNAP were far harder to estimate. From the parameter k_{cat} we know the rate at which a mole of substrate is cleaved per minute per gram of enzyme. Since we model PP_i as a molar concentration (mol ml^{-1}), we choose to model TNAP as a mass concentration (g ml^{-1}). Unfortunately in experimental models TNAP concentration is not measured. Instead it is common to measure the TNAP activity level, i.e. the rate at which a substrate (typically pNPP) is cleaved by the TNAP present. Another common measure is the TNAP mRNA expression. Using the data in Chang et al. (2006) human MSCs that were cultured in a mineralisation medium had an average TNAP activity of $1.15\times10^{-13}\,\text{mol pNPP cell}^{-1}\ \text{min}^{-1}$ after 9 days of culture. The control cells which were not cultured in a mineralisation medium and hence did not produce a mineralised matrix had a TNAP expression of $0.36\times10^{-13}\,\text{mol pNPP cell}^{-1}\ \text{min}^{-1}$. The rate at which pNPP is cleaved by purified TNAP was found to be $1.2 \times 10^{-3}\,\text{mol pNPP min}^{-1}\,\text{g}^{-1}$

(Simão et al. 2007). Furthermore we make the assumption that our cells are at a density of 10^6 cells ml^{-1}. This gives an approximate TNAP concentration of $95.8\times10^{-6}\,\mathrm{g\,ml}^{-1}$ for a population of mineralising cells and $30\times10^{-6}\,\mathrm{g\,ml}^{-1}$ for a population of control cells. It is desired that our initial conditions reflect a population of non-mineralising cells, and hence we take $A_0 = 30\times10^{-6}\,\mathrm{g\,ml}^{-1}$. We note however that the level of TNAP for the mineralising cells is useful for comparison to our results.

At this stage there are still 3 unknown parameters, α, β and η. We use the known parameters to rescale Equations (5.1)–(5.3) and make some simplifying assumptions based on the magnitude of some of the terms. This leads to a reduced system that is easier to analyse and allows us to determine some approximate bounds on the unknown parameters.

5.5 Rescaling the Kinetic Equations

Observing the initial conditions we see that there is a large difference in the magnitude of the different species. The sensible approach at this stage is to rescale our equations so that the variables have a magnitude of $\mathcal{O}(1)$.

We introduce new dimensionless variables

$$\bar{A} = \frac{A}{\hat{A}}, \quad \bar{P} = \frac{P}{\hat{P}}, \quad \bar{I} = \frac{I}{\hat{I}}, \quad \bar{t} = \frac{t}{\hat{t}}, \tag{5.5}$$

and let $\hat{A} = 10^{-5}$, $\hat{P} = 10^{-9}$, $\hat{I} = 10^{-6}$ and $\hat{t} = 1$. Substituting these new variables into Equations (5.1)–(5.3), leads us to introduce new dimensionless parameters

$$\begin{gathered} \bar{\alpha} = \frac{\alpha O\hat{t}}{\hat{A}}, \quad \bar{\beta} = \beta O\hat{P}\hat{t}, \quad \bar{\delta} = \delta\hat{t}, \\ \bar{\eta} = \frac{\eta O\hat{t}}{\hat{P}}, \quad \bar{k}_{\mathrm{cat}} = \frac{k_{\mathrm{cat}}\hat{A}\hat{t}}{\hat{P}}, \quad \bar{K}_M = \frac{K_M}{\hat{P}}, \quad \bar{K}_I = \frac{K_I}{\hat{I}}. \end{gathered} \tag{5.6}$$

The non-dimensionalised values for these parameters is given in Table 5.1.

Using these dimensionless parameters we can rewrite Equations (5.1)–(5.3) as

$$\frac{\mathrm{d}\bar{A}}{\mathrm{d}\bar{t}} = \bar{\alpha} + \bar{\beta}\bar{A}\bar{P} - \bar{\delta}\bar{A}, \tag{5.7}$$

$$\frac{\mathrm{d}\bar{P}}{\mathrm{d}\bar{t}} = \bar{\eta} - \frac{\bar{k}_{\mathrm{cat}}\bar{A}\bar{P}}{\bar{K}_M\left(1 + \frac{\bar{I}}{\bar{K}_I}\right) + \bar{P}}, \tag{5.8}$$

$$\frac{\mathrm{d}\bar{I}}{\mathrm{d}\bar{t}} = 2 \times 10^{-3}\frac{\bar{k}_{\mathrm{cat}}\bar{A}\bar{P}}{\bar{K}_M\left(1 + \frac{\bar{I}}{\bar{K}_I}\right) + \bar{P}}. \tag{5.9}$$

With rescaled initial conditions

$$\bar{A}(0) = \bar{A}_0, \qquad \bar{P}(0) = \bar{P}_0, \qquad \bar{I}(0) = \bar{I}_0. \tag{5.10}$$

From this point we can make two observations. The first is that the rate of change of $\mathrm{P_i}$ is at least three orders of magnitude smaller than the rate of change of $\mathrm{PP_i}$ or less obviously TNAP. The second relates to the denominator in the Michaelis-Menten term. The rescaled parameter $\bar{K}_M = \mathcal{O}(10^2)$ and the term $\bar{I}/\bar{K}_I = \mathcal{O}(10^2)$. Thus in the denominator $\bar{K}_M\big(1 + \bar{I}/\bar{K}_I\big) \gg \bar{P}$ and we neglect the term $\bar{P}$ in the denominator and can rewrite the system of equations as

$$\frac{\mathrm{d}\bar{A}}{\mathrm{d}\bar{t}} = \bar{\alpha} + \bar{\beta}\bar{A}\bar{P} - \bar{\delta}\bar{A}, \tag{5.11}$$

$$\frac{\mathrm{d}\bar{P}}{\mathrm{d}\bar{t}} = \bar{\eta} - \frac{\bar{k}_{\mathrm{cat}}\bar{A}\bar{P}}{\bar{K}_M\left(1 + \frac{\bar{I}}{\bar{K}_I}\right)}, \tag{5.12}$$

$$\frac{\mathrm{d}\bar{I}}{\mathrm{d}\bar{t}} = 2 \times 10^{-3}\frac{\bar{k}_{\mathrm{cat}}\bar{A}\bar{P}}{\bar{K}_M\left(1 + \frac{\bar{I}}{\bar{K}_I}\right)}. \tag{5.13}$$

This reduction now leaves the Michaelis-Menten term in the form typically used in the biological literature when discussing the action of TNAP on $\mathrm{PP_i}$.

5.6 Determining the Unknown Parameters

The parameters $\bar{\alpha}$, $\bar{\beta}$ and $\bar{\eta}$ are still yet to be determined. To determine these parameters we make some assumptions about the expected behaviour of our system under different circumstances. We consider the difference between osteoblasts that are actively involved in producing mineralised bone and osteoblasts that are not producing bone tissue. In the latter case we assume that the osteoblast population can be characterised by having a value

of $\bar{\beta} = 0$. This could represent a pool of immature osteoblasts that are not yet capable of producing mineralised bone. In this case the osteoblasts are only producing the baseline levels of TNAP, but are not producing the extra TNAP required to reduce PP_i levels so mineralisation can occur. We remind ourselves that the initial conditions to be used in our model were determined to represent a population of non-mineralising cells. So we would expect that when $\bar{\beta} = 0$ the behaviour seen in our system is that the stable concentration levels for TNAP and PP_i do not vary wildly from the values determined as the initial conditions. We would also expect that this steady state would be recovered even if different initial conditions were used. In particular, if a low initial condition was used for the PP_i concentration that it would recover to relatively high steady state value and inhibit mineral formation.

In the case of actively mineralising osteoblasts we assume that this cell population has a non-zero value of $\bar{\beta}$. In these cell populations we expect that the concentration of TNAP will increase and stabilise at a high level and that the concentration of PP_i will decrease and stabilise at a low level so that mineralisation will no longer be inhibited. Importantly this behaviour needs to be able to occur from an initial condition where TNAP is relatively low and PP_i is relatively high, representing the commencement of mineralisation in a region where mineralisation was previously not occurring.

To begin our analysis to determine the unknown parameters we simplify our model to two species. As mentioned previously, in Equations (5.11)–(5.13) the rate of change of P_i is much smaller then the rate of change of TNAP and PP_i. Thus we make the assumption that P_i has a constant value of $\bar{I} = \bar{I}_0$. We can further non-dimensionalise this system to reduce the number of parameters. We introduce new variables,

$$u = \frac{\bar{\delta}}{\bar{\alpha}}\bar{A}, \qquad v = \frac{\bar{\delta}}{\bar{\eta}}\bar{P}, \qquad \tau = \bar{\delta}\bar{t}, \tag{5.14}$$

and introduce parameters

$$a = \frac{\bar{\beta}\bar{\eta}}{\bar{\delta}^2}, \qquad b = \frac{\bar{\alpha}\bar{k}_{\text{cat}}}{\bar{\delta}^2\bar{K}_M\left(1 + \frac{\bar{I}_0}{\bar{K}_I}\right)}. \tag{5.15}$$

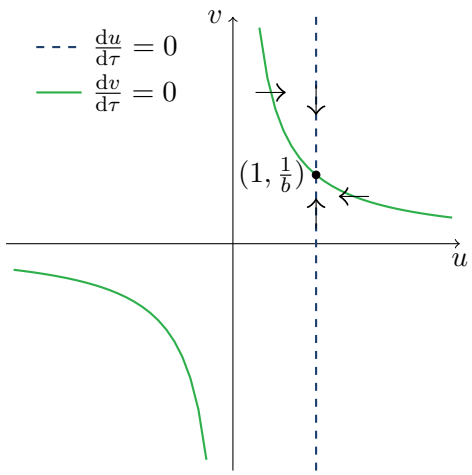

Figure 5.2: Phase plane for the Equations (5.18)–(5.19). The steady state at $(u, v) = (1, 1/b)$ is a stable node.

This gives the following non-dimensional equations for u and v

$$\frac{du}{d\tau} = 1 + auv - u, \tag{5.16}$$

$$\frac{dv}{d\tau} = 1 - buv. \tag{5.17}$$

5.6.1 Non-Mineralising Osteoblasts

In the case of non-mineralising osteoblasts we make the assumption that $\bar{\beta} = 0$. In our non-dimensionalised model this gives $a = 0$ and Equations (5.16) and (5.17) reduce to

$$\frac{du}{d\tau} = 1 - u, \tag{5.18}$$

$$\frac{dv}{d\tau} = 1 - buv. \tag{5.19}$$

We can draw a phase plane for this system and this is illustrated in Figure 5.2. By inspection of the phase plane we see that there exists only one steady state and that this steady state will always be in the positive quadrant. The steady state occurs at $(u, v) = (1, 1/b)$ and can be shown to be a stable node.

Based on the behaviour observed in non-mineralising cells we want the kinetics for $\bar{\beta} = 0$ to have a steady state where TNAP is low and PP_i is high. To determine appropriate bounds on $\bar{\alpha}$, $\bar{\beta}$ and $\bar{\eta}$ we need to introduce some approximate quantitative bounds on TNAP and PP_i concentrations. We define a low range of TNAP to be $1 < \bar{A} < 5$ and a high range for PP_i to be

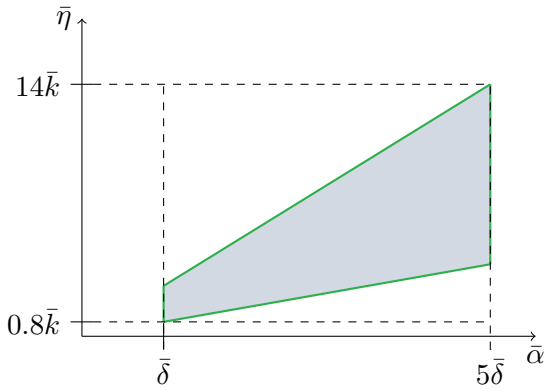

Figure 5.3: Parameter space for $\bar{\alpha}$ and $\bar{\eta}$. The shaded range of values should give results that replicate the behaviour of non-mineralising cells.

$0.8 < \bar{P} < 2.8$, this range of concentration for $\mathrm{PP_i}$ is essentially the range of concentration observed in normal human serum.

Working backwards from the steady state $u = 1$, we have that the corresponding steady state in the original system is $\bar{A} = \bar{\alpha}/\bar{\delta}$. Thus the range of values for $\bar{\alpha}$ that will give rise to a low concentration of TNAP is

$$\bar{\delta} < \bar{\alpha} < 5\bar{\delta}. \tag{5.20}$$

We can use a similar process to determine the range of acceptable values for $\bar{\eta}$. To achieve a high steady state value of $\mathrm{PP_i}$ it must be that

$$0.8\frac{\bar{k}\bar{\alpha}}{\bar{\delta}} < \bar{\eta} < 2.8\frac{\bar{k}\bar{\alpha}}{\bar{\delta}}, \tag{5.21}$$

where

$$\bar{k} = \frac{\bar{k}_{\mathrm{cat}}}{\bar{K}_M\left(1 + \frac{\bar{I}_0}{\bar{K}_I}\right)}. \tag{5.22}$$

We illustrate this region for the parameter values given in Table 5.1 in Figure 5.3.

5.6.2 Mineralising Cells

We now extend this process to consider cells that have responded to an appropriate biological signal and are producing mineralised bone. We model this by setting the parameter $\bar{\beta} \neq 0$ or equivalently $a \neq 0$. The phase plane for Equations (5.16) and (5.17) is given in Figure 5.4. The phase plane shows

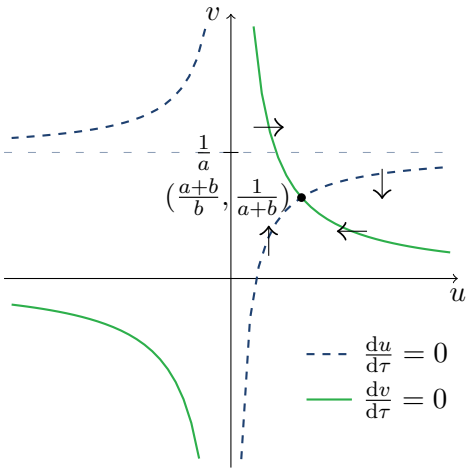

Figure 5.4: Phase plane for the Equations (5.16)–(5.17). There is a single stable steady state at $(u, v) = ((a + b)/b, 1/(a + b))$.

again there is only one steady state and that this steady state is in the positive quadrant. This steady state is located at

$$(u, v) = \left(\frac{a+b}{b}, \frac{1}{a+b}\right), \tag{5.23}$$

and is always stable but may be a node or a spiral dependent on the values of a and b.

For mineralising cells we expect that the concentration of TNAP will be high and that the concentration of $\mathrm{PP_i}$ will be low. Again we define some threshold values to determine an appropriate range for the parameter $\bar{\beta}$. For TNAP to be high we want a steady state value of $6 < \bar{A} < 10$ and for low $\mathrm{PP_i}$ we want a steady state value of $\bar{P} < 0.5$.

Following the same process used to determine $\bar{\alpha}$ and $\bar{\eta}$ we can find the following constraints on β,

$$\frac{\left(6\bar{\delta} - \bar{\alpha}\right)\bar{k}}{\bar{\eta}} < \bar{\beta} < \frac{\left(10\bar{\delta} - \bar{\alpha}\right)\bar{k}}{\bar{\eta}}, \tag{5.24}$$

and

$$\bar{\beta} > \frac{\bar{\eta}\bar{\delta} - 0.5\bar{\alpha}\bar{k}}{0.5\bar{\eta}}. \tag{5.25}$$

The lower and upper bound on $\bar{\beta}$ for the parameters given in Table 5.1 is shown in Figure 5.5.

An interesting observation that can be made is that above the line $\bar{\eta} = 5\bar{k}$ the estimated upper bound on $\bar{\beta}$ is lower then the lower bound. This intro-

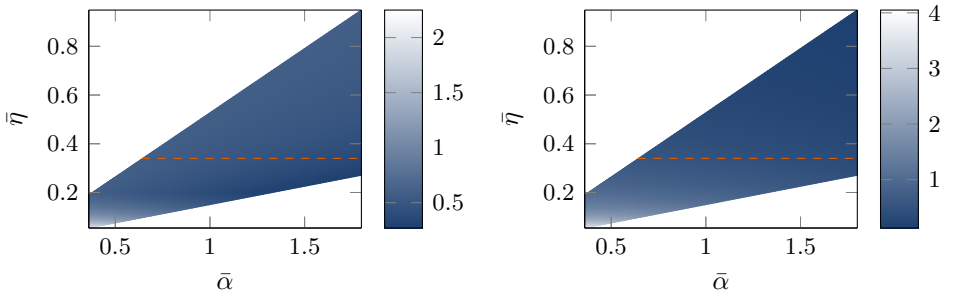

Figure 5.5: Parameter space for $\bar{\beta}$. The lower bound is in (a) and the upper bound is in (b). The dashed orange line represents the bound $\bar{\eta} = 5\bar{k}$

duces an additional constraint on the parameter choices, $\bar{\eta} < 5\bar{k}$. We also observe through experimentation with differing parameter choices that parameter choices from the lower left hand corner of the parameter space tend to have unrealistic properties. The behaviour of the TNAP concentration, for example, rises then falls rapidly to form a very tall sharp peak.

We can take the information above as well as the constraints in Equations (5.20)–(5.21) to come up with some possible ranges for the parameters $\bar{\alpha}$ and $\bar{\eta}$. Using the parameter values given in Table 5.1 we estimate that

$$0.36 < \bar{\alpha} < 1.8, \tag{5.26}$$

$$0.1 < \bar{\eta} < 0.34. \tag{5.27}$$

It is much harder to define even an approximate range of potential values for $\bar{\beta}$, as this parameter is highly dependent on the choice of $\bar{\alpha}$ and $\bar{\beta}$. For example with $\bar{\alpha} = 0.36$ and $\bar{\eta} = 0.1$ the range of potential $\bar{\beta}$ values is $1.2 < \bar{\beta} < 2.1$, however with $\bar{\alpha} = 1.8$ and $\bar{\eta} = 0.33$ the range of potential $\bar{\beta}$ values is $0.35 < \bar{\beta} < 0.37$.

For the simulations in the following sections we choose to use mid-range values for $\bar{\alpha}$, $\bar{\eta}$ and $\bar{\beta}$. Thus we choose $\bar{\alpha} = 1.08$, with this choice of $\bar{\alpha}$ then the range of potential $\bar{\eta}$ values is $0.16 < \bar{\eta} < 0.33$. Again taking the mid-point we obtain $\bar{\eta} = 0.25$. Finally using these values of $\bar{\alpha}$ and $\bar{\eta}$ gives a potential range for $\bar{\beta}$ of $0.43 < \bar{\beta} < 0.68$. Once again we take the midpoint giving $\bar{\beta} = 0.56$. These parameter ranges and values are summarised in Table 5.2.

Parameter	Range	Value Used
$\bar{\alpha}$	0.36–1.8	1.08
$\bar{\eta}$	0.16–0.33	0.25
$\bar{\beta}$	0.43–0.68	0.56

Table 5.2: Non-dimensional values for parameters $\bar{\alpha}$,$\bar{\eta}$ and $\bar{\beta}$ as used in simulations.

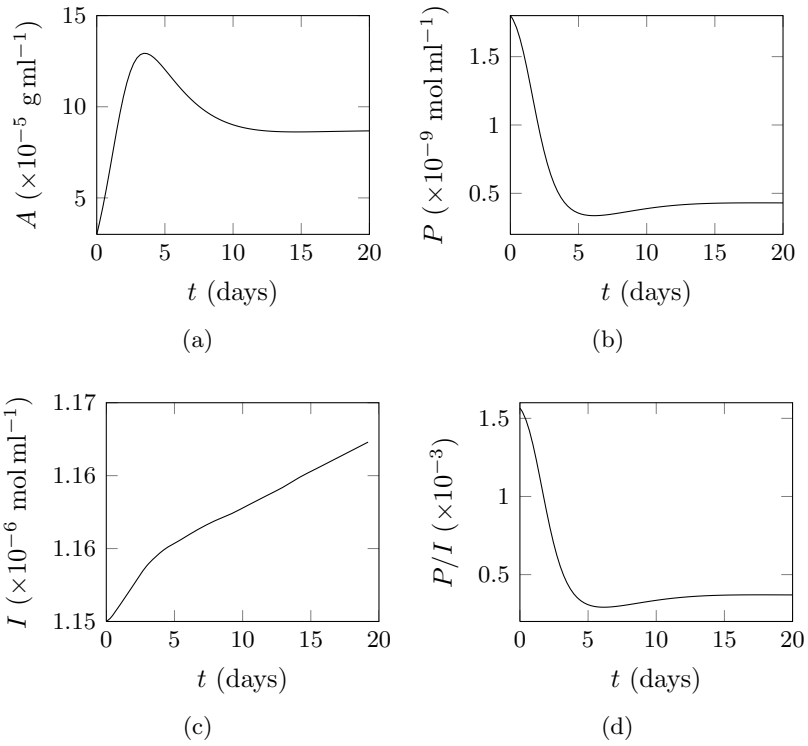

Figure 5.6: Concentration profiles for (a) TNAP, (b) PP_i, (c) P_i and (d) the ratio of PP_i to P_i. The parameters used in these simulations were as listed in Tables 5.1 and 5.2

5.7 Results and Discussion

Using the rescaled Equations (5.7)–(5.9) we simulated our model. The parameters and initial conditions were as given in Table 5.1 and Table 5.2. We used the inbuilt MATLAB (Release 2012b) solver `ode45` to solve the equations numerically. The concentration profiles for each of the 3 species are shown in Figure 5.6, as well as the ratio of the concentrations of PP_i to P_i.

We see that initially the TNAP concentration increases sharply with a peak

of $130 \times 10^{-6}\,\mathrm{g\,ml^{-1}}$ occurring just before 3.5 days have elapsed. This peak represents a 4.3 fold increase in the amount of TNAP present. After this the concentration declines at a slower rate and appears to be tending towards a steady state. The concentration for the PP_i initially decreases as PP_i is cleaved by the TNAP. The lowest concentration of PP_i is $3.37\times10^{-10}\,\mathrm{mol\,ml^{-1}}$. This is below the lower bound of physiological serum values for PP_i which is $0.64 \times 10^{-9}\,\mathrm{mol\,ml^{-1}}$. This minimum occurs after 6.2 days so the PP_i minimum lags the ALP peak by 2.7 days. The concentration profile for P_i shows that P_i concentration values are only changing minimally, and we note that these changes are much smaller then the daily fluctuations in serum P_i concentrations (Jubiz et al. 1972). This result should not be surprising if we consider the concentrations of both of these species in serum. The concentration of PP_i is in the order of $10^{-9}\,\mathrm{mol\,ml^{-1}}$ whereas P_i concentrations are in the order of $10^{-6}\,\mathrm{mol\,ml^{-1}}$, three orders of magnitude larger. Given that the enzymatic reaction that cleaves PP_i creates two P_i from one PP_i we expect that to make a significant change in the P_i concentration a large amount of PP_i would need to be cleaved. It is often mentioned in the literature that the role of TNAP is to both decrease PP_i and increase P_i, however further research has indicated that the former of these is the dominant role (Hessle et al. 2002, Murshed et al. 2005). Our model further supports this theory that the most important role of TNAP is to remove PP_i.

Our model only considers the influence of the cleaving of PP_i on the concentration level of P_i. The observation that the cleaving of PP_i does not significantly change the P_i concentration levels is of interest in understanding the role played by PP_i and P_i in mineralisation. It has been hypothesised that the ratio of PP_i to P_i is more important in driving mineralisation rather then the actual concentrations of the species individually (Murshed et al. 2005). The ratio P/I over time for our simulation is shown in Figure 5.6(d). We see that because of the small changes in P_i concentration the profile of the ratio follows that of the concentration of PP_i. Thus from our results it appears that, for a person with a normal healthy metabolism of phosphate, the changes in this ratio in order for mineralisation to occur are much more related to the removal of the inhibitor PP_i then the associated increase in P_i levels (however in the instance where phosphate metabolism is impaired then it may still be playing an important role in raising serum concentration).

Due to the wide ranging experimental protocols apparent in the biological community it is difficult to quantitatively match our TNAP concentration profile to those presented in the literature. We can however match our profiles qualitatively to plots of TNAP activity in cell cultures. In Figure 5.7 we show the TNAP expression for human osteoblasts treated with BMP 2 at $100\,\mathrm{ng\,ml^{-1}}$ (Lecanda et al. 1998). The qualitative behaviour in this plot is typical of TNAP activity of mineralising cells in culture (see for example (Korkalainen et al. 2009, Choi et al. 1996, Kristensen et al. 2012, Delhanty et al. 2006)). The TNAP activity levels increase, hit a peak, then decrease slightly to a level that is still much higher than the initial condition, the exact timing and magnitude of the curves depends on a variety of factors including the cell type and mineralisation medium used. In the data shown here the peak is achieved at 5 days. At this peak the increase in TNAP activity compared to the control experiment (data not shown) is approximately 3.7 fold. The activity rate then decreases to be a 3.3 increase on the control value. These results are similar to those presented in Chang et al. (2006) and discussed in Section 5.4. There mineralising cells had a 3.2 fold increase in TNAP activity after 9 days of culture compared to the rate of TNAP activity in non-mineralising cells.

If we compare our simulation results for TNAP concentration to those for TNAP activity we see our concentration profile follows the general shape seen in cell culture experiments, with an increase to a peak followed by a small decrease. However in our simulations the peak occurs earlier then observed in the experimental results. One possible explanation for this discrepancy is that our model fails to account for the time required for cellular differentiation to occur. The parameters in our model were chosen to represent the parameters in mineralising cells whereas our initial conditions were chosen to represent a situation were no cells were mineralising. Thus an interpretation of this is that at $t = 0$ all the non-mineralising cells (possibly osteoblast progenitors) suddenly differentiate into osteoblasts. In reality cell-differentiation is non-discrete and changes in cell production rates of proteins. for example TNAP, change gradually over time as the cells differentiate. Indeed increased TNAP expression is typically used as a marker that osteoblastic differentiation has occurred.

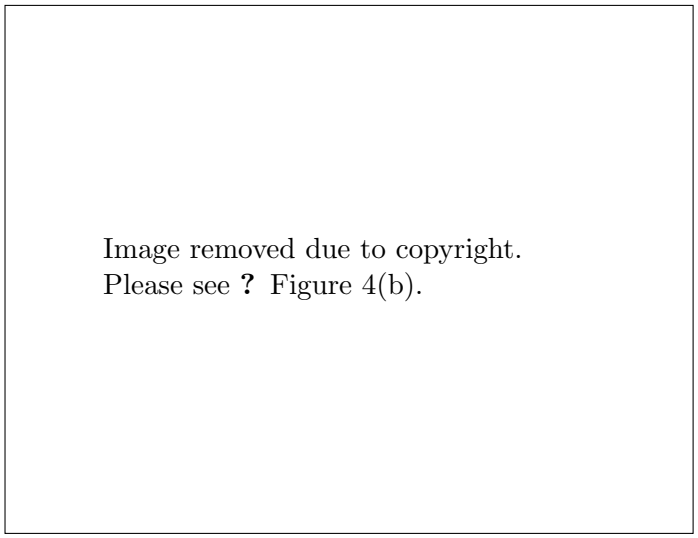

Figure 5.7: Comparison of experimental results for TNAP expression with simulation results for TNAP concentration. The blue curve shows experimentally determined TNAP activity in human osteoblasts treated with BMP-2 (Data from (Lecanda et al. 1998)). The green curve shows TNAP concentration as predicted by our model. We see that the curves have a similar characteristic shape but that there are differences in the timing of the peaks.

5.7.1 Influence of the rate of TNAP expression on the system

In our discussion of the appropriate choice of parameters $\bar{\alpha}$, $\bar{\eta}$ and $\bar{\beta}$ we examined the behaviour that we would expect to occur in a population of non-mineralising cells. As no mineralisation is occurring we expect that the concentration levels of the mineralisation inhibitor PP_i will not be reduced below the known physiological serum concentration.

Non-mineralising osteoblast progenitors express TNAP at a much lower rate than mineralising cells. In our model we represent this by setting $\bar{\beta} = 0$. We interpret this as the non-mineralising cells are still producing baseline levels of TNAP (as defined by the parameter $\bar{\alpha}$) but are not producing any additional TNAP in response to the local TNAP or PP_i concentration.

We now observe the behaviour of our model when used to simulate a population of non-mineralising cells. To do this we set $\bar{\beta} = 0$ and keep all other parameters as given in Table 5.1 and Table 5.2. The concentration profiles from these simulations are shown in Figure 5.8.

In these results we see a slightly different qualitative behaviour to that observed in Figure 5.6. The TNAP concentration levels stay constant. This

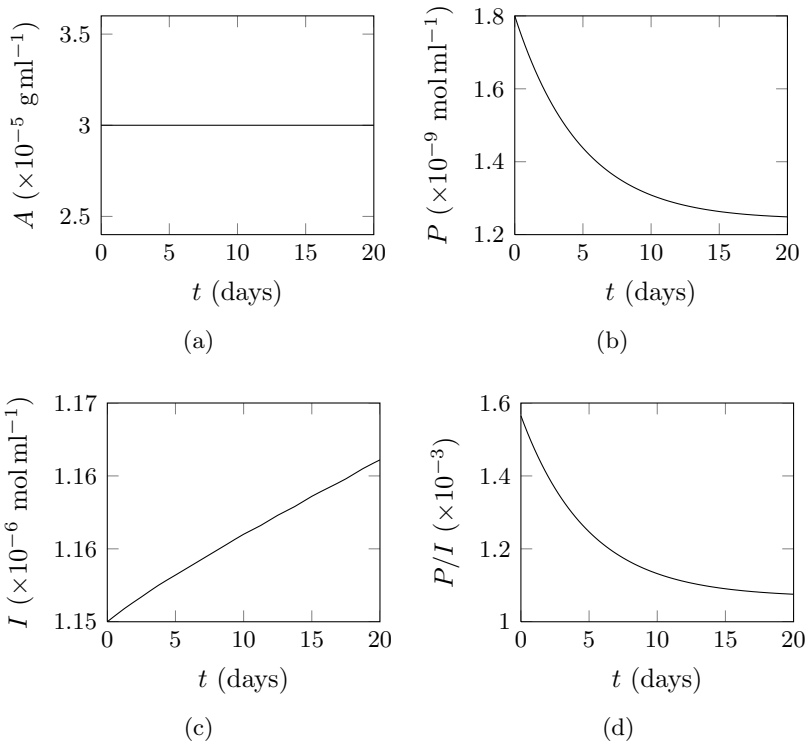

Figure 5.8: Concentration profiles for (a) TNAP, (b) PP_i, (c) P_i and (d) the ratio of PP_i to P_i. The parameters used are given in Tables 5.1 and 5.2, with $\bar{\beta} = 0$. We see that the ALP concentration remains constant, the PP_i concentration decreases slightly but still remains within physiological serum values.

is a consequence of the parameter choice of $\bar{\alpha}$ which means that the initial condition is the steady state. Again we recall that the initial conditions were chosen to be representative of non-mineralising cells so this result is desirable. The concentration profile for PP_i shows that PP_i decreases over time but importantly the lowest value for PP_i concentration is $1.25 \times 10^{-9}\,\mathrm{mol\,ml^{-1}}$ which is still well within the bounds of normal serum concentration (0.64-$2.96\times10^{-9}\mathrm{mol\,ml^{-1}}$). Since the concentration of PP_i is still within the bounds of normal serum concentration this would indicate that mineralisation would be unlikely to occur under these circumstances.

5.8 Extension to Moving Boundary

Within our generalised view of the fracture callus formation we consider apposition of new bone to be an important factor in driving the growth of the

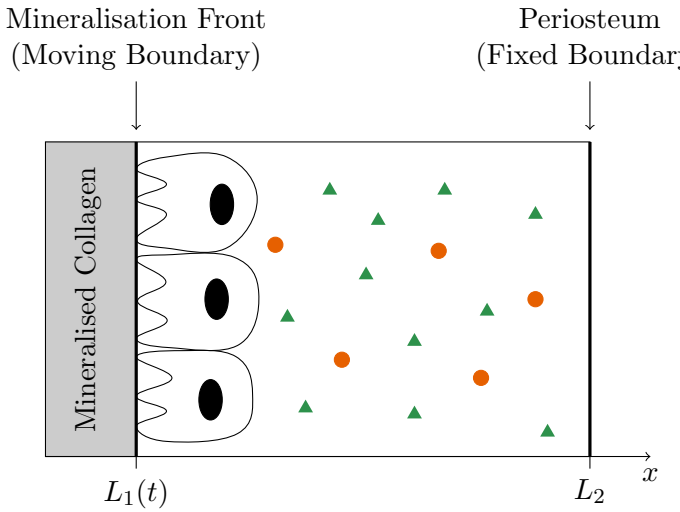

Figure 5.9: Schematic of domain for mineralisation model, we assume uniformity in the y direction and only consider the behaviour in the x direction. On the mineral front $x = L_1$ new mineralised bone is being created due to the actions of osteoblasts present on the bone surface. The right boundary at $x = L_2$ represents the periosteum. In the region between these boundaries exists other osteoblasts and extracellular matrix. PP_i and P_i are free to circulate throughout this region but TNAP is bound to the cell membrane of the osteoblasts.

callus. To model the movement of the mineralisation front we take our previously described kinetics for TNAP, PP_i and P_i and include appropriate spatial effects. The behaviour we are aiming to model is the deposition of new bone onto an existing bone surface, such as that illustrated in Figure 5.9. The mineralisation occurs through the presence of osteoblasts on the bone surface. These cells produce the collagen matrix and regulate the deposition of mineral onto the matrix. As the mineral forms the osteoblast can become trapped in the matrix and subsequently differentiate to become osteocytes, which are believed to play a key role in regulating the remodelling of the bone.

A model for the progression of the mineralisation front is also presented in (Prokharau et al. 2012). They build a model for osseointegration of an implant. Whilst the the authors consider a different context and model differing regulatory factors to those we consider here, both models aim to represent the movement of the mineralisation front during intramembranous bone formation.

5.8.1 Model Description

The model that we present here represents an initial attempt at creating a mathematical model for the deposition of mineral during bone formation as a response to the ratio of concentrations of PP_i and P_i. We consider a 1D domain where there is an existing bone surface at one end. Adopting the convention that new bone formation tends to occur adjacent to existing bone we assume that new bone formation can only occur at this bone surface. The bone formation occurs when the ratio of PP_i to P_i is conducive to mineralisation, that is when there is a low ratio of PP_i to P_i. In our model we only consider the three species previously explored in the kinetic model, TNAP, PP_i and P_i.

In this model we do not explicitly include the effect of either the cellular populations or the collagen extracellular matrix. Instead we make some assumptions about their behaviour. We assume that across our domain of interest there is a uniform distribution of osteoblasts, but that mineralisation is confined to only occur on the existing bone surface. In addition we assume that the osteoblasts have produced sufficient collagen such that mineralisation can occur.

To describe the rate of change of TNAP, PP_i and P_i we use the kinetics given in Equations (5.1)–(5.3) and include appropriate terms to describe their spatial movement. We assume that the functional TNAP is bound to the osteoblast cell membrane (Murshed et al. 2005), whereas the PP_i and P_i will be freely circulating throughout the domain.

We can write an equation for the rate of change of TNAP as

$$\frac{\partial A}{\partial t} = D_A \frac{\partial^2 A}{\partial x^2} + \alpha O + \beta APO - \delta A, \tag{5.28}$$

the first term represents the spatial movement of the TNAP due to the movement of the osteoblasts. As with our earlier models, we model the osteoblast movement as Fickian diffusion as a first approximation, where D_A is the diffusion coefficient. We note that we are neglecting the influence that the moving mineralisation front may have on the displacement of the osteoblasts.

The equation for the rate of change of PP_i is given as

$$\frac{\partial P}{\partial t} = D_P \frac{\partial^2 P}{\partial x^2} + \eta O - \frac{k_{\text{cat}} AP}{K_M(1 + \frac{I}{K_I})}, \tag{5.29}$$

and the equation for the rate of change of P_i as

$$\frac{\partial I}{\partial t} = D_I \frac{\partial^2 I}{\partial x^2} + 2\frac{k_{\text{cat}} AP}{K_M + \frac{I}{K_I}}, \tag{5.30}$$

where D_P and D_I are the diffusion coefficients for PP_i and P_i respectively.

We now turn our attention to the behaviour at the boundaries. Referring to the schematic in Figure 5.9 the left boundary represents the moving mineralisation front, which we denote as $x = L_1(t)$ and the right boundary at $x = L_2$ represents the periosteum. As the new bone tissue is deposited the boundary $x = L_1(t)$ moves to the right. We consider the boundary at $x = L_2$ to be static, but note that it could be of interest to consider the behaviour of the model if this boundary could also move, for example representing the growth of the callus due to proliferation of progenitor cells.

We focus first on the boundary at $x = L_1(t)$. We assume that the speed at which the boundary moves is dependent on the ratio of PP_i to P_i. When this ratio is high mineralisation occurs slowly or not at all, whereas when the ratio is low mineralisation occurs at a much faster rate. Based on this we model the movement of the left boundary as a smoothed step function,

$$\frac{\mathrm{d}L_1}{\mathrm{d}t} = \frac{\lambda}{2}\left(1 + \tanh\left(\mu\left(\gamma - \frac{P(L_1,t)}{I(L_1,t)}\right)\right)\right), \tag{5.31}$$

where λ represents the maximum speed of the boundary, μ determines the steepness of the front, and γ is the switching point.

In addition we need to define the boundary conditions for the three species in our model. As the mineralisation front moves we assume that cells on the bone surface are not displaced by the mineralisation front. Rather as the front advances these cells become trapped within the new matrix and eventually become osteocytes. As such the TNAP that is bound to the cell membranes will also become embedded in the newly formed matrix. We use a similar boundary condition for the PP_i. Here we assume that there is an outward flux of PP_i as the boundary moves due to two factors. Firstly as the mineral crystal is formed some PP_i binds to the mineral. Secondly newly mineralised bone is porous, so the extracellular fluid containing the PP_i can flow through this space. As a first approximation for the loss of PP_i we assume that all PP_i in a region that transforms from non-mineral to mineralised bone is lost.

Thus, we write the boundary conditions for TNAP and PP_i on $x = L_1$ as

$$\frac{\partial A}{\partial x} = 0, \tag{5.32}$$

$$\frac{\partial P}{\partial x} = 0. \tag{5.33}$$

We note that within the moving boundary framework that this is not a zero flux boundary condition. The flux leaving the boundary for TNAP, for example, is actually equal to $\frac{\mathrm{d}L_1}{\mathrm{d}t}A$. For more details on this see Section C.4 in the appendix.

The final condition on the left boundary is for P_i. We assume that there is a loss of P_i due to P_i being incorporated into the newly forming mineral. From a conservation of mass argument, as seen in Stefan problems (Gupta 2003), the boundary condition is

$$\frac{\partial I}{\partial x} = \frac{I - I_M}{D_I}\frac{\mathrm{d}L_1}{\mathrm{d}t}, \tag{5.34}$$

where I_M is the density of P_i in newly mineralised bone.

Finally, we need to determine the boundary conditions on the right boundary $x = L_2$. We assume that this right boundary represents the periosteum. As the TNAP is bound to the cells we assume that these cells cannot cross the periosteum and hence that on $x = L_2(t)$ that

$$\frac{\partial A}{\partial x} = 0. \tag{5.35}$$

For the PP_i we assume that there is some inflow of PP_i from the extracellular space, where the concentration of PP_i is P_0, through the periosteum, however this flow is impeded by the membrane and hence use an advective boundary condition

$$\frac{\partial P}{\partial x} = -\sigma(P - P_0), \tag{5.36}$$

where σ represents the permeability of the periosteum.

For P_i we assume that at the periosteum P_i concentration levels are at the serum concentration levels and hence take

$$I = I_0. \tag{5.37}$$

The initial conditions used were to assume a spatially homogeneous distribution across the domain and that this value was equal to the previously

Parameter	Value	Units	Dimensionless Value
D_A	4×10^{-8}	$\mathrm{cm}^2\,\mathrm{day}^{-1}$	4×10^{-6}
D_P	285×10^{-3}	$\mathrm{cm}^2\,\mathrm{day}^{-1}$	28.5
D_I	285×10^{-3}	$\mathrm{cm}^2\,\mathrm{day}^{-1}$	28.5
λ	2.2×10^{-4}	$\mathrm{cm}\,\mathrm{day}^{-1}$	2.2×10^{-3}
μ	30×10^{3}		30
γ	0.45×10^{-3}		0.45
I_M	2.9×10^{-3}	$\mathrm{mol}\,\mathrm{ml}^{-1}$	2.9×10^{3}
σ	0.01	cm^{-1}	1×10^{-3}

Table 5.3: Table of additional parameters for the extended mineralisation model.

determined serum concentration levels. This gives

$$A(x,0) = A_0, \tag{5.38}$$

$$P(x,0) = P_0, \tag{5.39}$$

$$I(x,0) = I_0, \tag{5.40}$$

and finally we define the initial position of the bone surface as

$$L_1(0) = L_{1_0}. \tag{5.41}$$

5.8.2 Parameters

For the kinetic component of the equations we use the parameters given in Tables 5.1 and 5.2. The remaining parameter values are discussed here.

We have assumed that the active TNAP is bound to the cell membrane of the osteoblasts, hence we take the diffusion coefficient for TNAP to be the same as the diffusion coefficient used for the osteoblast population in our model for cellular differentiation. This gives $D_A = 4 \times 10^{-8}\,\mathrm{cm}^2\,\mathrm{day}^{-1}$.

Measurements of the diffusion of $\mathrm{P_i}$ through frog muscle tissue give a diffusion coefficient of $3.3 \pm 0.4 \times 10^{-6}\,\mathrm{cm}^2\,\mathrm{s}^{-1}$ (Yoshizaki et al. 1982). We assume that the diffusion throughout muscle tissue provides a good approximation for diffusion through the fracture callus region and take $D_I = 285 \times 10^{-3}\,\mathrm{cm}^2\,\mathrm{day}^{-1}$. In water the diffusion coefficient of $\mathrm{PP_i}$ is of a similar magnitude as that of $\mathrm{P_i}$ (Flury & Gimmi 2002). Thus as a first approximation we assume that the diffusion coefficient for $\mathrm{PP_i}$ is the same as $\mathrm{P_i}$ and take $D_P = 285 \times 10^{-3}\,\mathrm{cm}^2\,\mathrm{day}^{-1}$.

In humans the density of mineral in cancellous bone, which is similar in structure to new intramembranous bone, is $0.49\,\mathrm{g\,cm^{-3}}$ (Donnelly et al. 2010). As a starting point we assume that this is also the density of mineral in new intramembranous bone. We further assume that this mineral is 100% pure hydroxyapatite, which gives a molar density for $\mathrm{P_i}$ in new bone as $I_M = 2.9 \times 10^{-3}\,\mathrm{mol\,ml^{-1}}$. We note that it is likely that this is an overestimation of the parameter I_M as newly formed woven bone is generally more porous than existing bone (Currey 2002).

We have three parameters to determine the speed of the mineralisation front described in Equation (5.31). The parameter λ describes the maximum speed at which the mineralisation front moves, the parameter μ determines the steepness of the curve and the parameter γ determines the switching point of the curve. Considering our results from the kinetic model, we desire almost no mineralisation for a ratio of $P/I > 0.55 \times 10^{-3}$, but full mineralisation occurring for ratios $P/I < 0.35 \times 10^{-3}$. From this we choose $\gamma = 0.45 \times 10^{-3}$ and $\mu = 30 \times 10^3$ to give an appropriate switching point and a sufficiently steep curve. To determine the maximum speed of the mineralisation front we used the mineral apposition rate, commonly reported in histomorphological studies of bone. In a goat model of distraction osteogenesis, where healing is assumed to occur mostly through an intramembranous pathway, the mineral apposition rate in the mineralising zone was on average $2.2\,\mu\mathrm{m\,day^{-1}}$ (Welch et al. 1998). From this we set $\lambda = 2.2 \times 10^{-4}\,\mathrm{cm\,day^{-1}}$. The validity of using the mineral apposition rate to determine the mineralisation front speed is discussed later in this chapter.

The parameter σ represents the permeability of the periosteum. Through trial and error it was taken as $\sigma = 0.01$.

5.8.3 Non-Dimensionalisation

As was done with the kinetic equations we rescale our system of PDEs to aid with the numerical simulations. We use the same non-dimensional variables as before,

$$\bar{A} = \frac{A}{\hat{A}}, \quad \bar{P} = \frac{P}{\hat{P}}, \quad \bar{I} = \frac{I}{\hat{I}}, \quad \bar{t} = \frac{t}{\hat{t}}, \tag{5.42}$$

and introduce a new non-dimensional spatial variable

$$\bar{x} = \frac{x}{\hat{x}}. \tag{5.43}$$

As before we let $\hat{A} = 10^{-5}\,\mathrm{g\,ml^{-1}}$, $\hat{P} = 10^{-9}\,\mathrm{mol\,ml^{-1}}$, $\hat{I} = 10^{-6}\,\mathrm{mol\,ml^{-1}}$ and $\hat{t} = 1\,\mathrm{min}$, and introduce $\hat{x} = 0.1\,\mathrm{cm}$.

We introduce new dimensionless parameters as in Equation (5.6), as well as

$$\begin{aligned} \bar{D}_A = \frac{D_A\hat{t}}{\hat{x}^2}, \quad \bar{D}_P = \frac{D_P\hat{t}}{\hat{x}^2}, \quad \bar{D}_I = \frac{D_I\hat{t}}{\hat{x}^2}, \\ \bar{\lambda} = \frac{\lambda\hat{t}}{\hat{x}}, \quad \bar{\mu} = \frac{\mu\hat{P}}{\hat{I}}, \quad \bar{\gamma} = \frac{\gamma\hat{I}}{\hat{P}}, \\ \bar{I}_M = \frac{I_M}{\hat{I}}, \quad \bar{\sigma} = \sigma\hat{x}. \end{aligned} \tag{5.44}$$

Additionally the location of the boundaries are also rescaled to

$$\bar{L}_1(t) = \frac{L_1(t)}{\hat{x}}, \quad \bar{L}_2 = \frac{L_2}{\hat{x}}. \tag{5.45}$$

Using these dimensionless parameters the system can be written in full as

$$\frac{\partial\bar{A}}{\partial\bar{t}} = \bar{D}_A\frac{\partial^2\bar{A}}{\partial\bar{x}^2} + \bar{\alpha} + \bar{\beta}\bar{A}\bar{P} - \bar{\delta}\bar{A}, \tag{5.46}$$

$$\frac{\partial\bar{P}}{\partial\bar{t}} = \bar{D}_P\frac{\partial^2\bar{P}}{\partial\bar{x}^2} + \bar{\eta} - \frac{\bar{k}_{\mathrm{cat}}\bar{A}\bar{P}}{\bar{K}_M\left(1 + \frac{\bar{I}}{\bar{K}_I}\right)}, \tag{5.47}$$

$$\frac{\partial\bar{I}}{\partial\bar{t}} = \bar{D}_I\frac{\partial^2\bar{I}}{\partial\bar{x}^2} + 2\times10^{-3}\frac{\bar{k}_{\mathrm{cat}}\bar{A}\bar{P}}{\bar{K}_M\left(1 + \frac{\bar{I}}{\bar{K}_I}\right)}, \tag{5.48}$$

$$\frac{\mathrm{d}\bar{L}_1}{\mathrm{d}\bar{t}} = \frac{\bar{\lambda}}{2}\left(1 + \tanh\left(\bar{\mu}\left(\bar{\gamma} - \frac{\bar{P}(\bar{L}_1,\bar{t})}{\bar{I}(\bar{L}_1,\bar{t})}\right)\right)\right). \tag{5.49}$$

$$\tag{5.50}$$

With boundary conditions on $\bar{x} = \bar{L}_1(t)$

$$\frac{\partial\bar{A}}{\partial\bar{x}} = 0, \tag{5.51}$$

$$\frac{\partial\bar{P}}{\partial\bar{x}} = 0, \tag{5.52}$$

$$\frac{\partial\bar{I}}{\partial\bar{x}} = \frac{\bar{I} - \bar{I}_M}{\bar{D}_I}\frac{\mathrm{d}\bar{L}_1}{\mathrm{d}\bar{t}}, \tag{5.53}$$

and on $\bar{x} = \bar{L}_2$,

$$\frac{\partial\bar{A}}{\partial\bar{x}} = 0, \tag{5.54}$$

$$\frac{\partial\bar{P}}{\partial\bar{x}} = -\bar{\sigma}(\bar{P} - \bar{P}_0), \tag{5.55}$$

$$\bar{I} = \bar{I}_0. \tag{5.56}$$

The initial conditions are given as

$$\bar{A}(\bar{x},0)=\bar{A}_0,\quad \bar{P}(\bar{x},0)=\bar{P}_0,\quad \bar{I}(\bar{x},0)=\bar{I}_0,\quad \bar{L}_1(0)=\bar{L}_{1_0}. \tag{5.57}$$

5.8.4 Numerical Methods

The numerical method used to simulate these results was the same as that used in Chapter 4. We rescaled the moving domain to a static domain, rewrote the equation in conservative form and then used the finite volume method to obtain the spatial discretisation and used the inbuilt MATLAB (Release 2012b) function `ode15i` to perform the time integration. More details on the rescaling and the finite volume method is given in Appendix C.

5.8.5 Results and Discussion

In the first set of simulations conducted we considered the periosteum to be located 0.2 mm away from the original bone surface, that is $\bar{L}_{1_0}=0$ and $\bar{L}_2=2$. All other parameters were as in Tables 5.1–5.3. In Figure 5.10 we show the concentration profiles over a period of 10 days. We remind ourselves that within the context of fracture healing these processes need to occur quickly and hence we are only interested in the behaviour of the system over a relatively short period of time. In addition we show a magnified version of the concentration profiles of I near the boundary $x=L_1(t)$ to show that the boundary is indeed moving. We also show the position of the mineralisation front and its velocity in Figure 5.11.

Spatially the profiles for ALP and $\mathrm{PP_i}$ appear almost uniform, however the concentrations on the right boundary, where there is a small influx of $\mathrm{PP_i}$ are slightly higher. Temporally the concentration levels follow a similar pattern to that observed in the purely kinetic models. The ALP starts at the low initial condition representing the expression of non-mineralising cells. Initially, it rises rapidly to a maximum of around $13.4\times10^{-5}\,\mathrm{g\,ml^{-1}}$ achieved after 3.7 days. It then decreases slightly before reaching a minimum of around $9.3\times10^{-5}\,\mathrm{g\,ml^{-1}}$ after 12.3 days. Following this point there is at least one more small oscillation visible in the solution. As the oscillations decay we note that over a long time the concentration does not tend to a steady value. This is not surprising given the changing nature of the domain. There is instead a very slow increase in TNAP concentration. We are not overly concerned with the long time behaviour but we note that even after running the simulation to

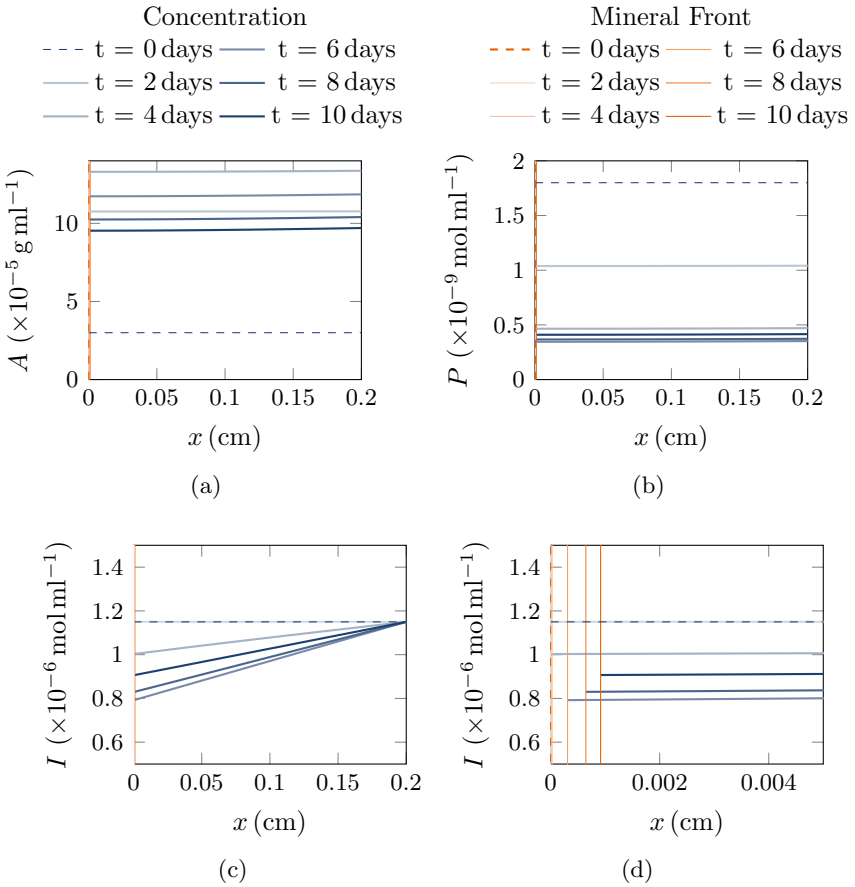

Figure 5.10: Concentration profiles over time, the blue lines represent the concentration profiles and the orange lines represent the location of the boundary. We show the profiles at $t = 0, 2, 4, 6, 8, 10$ days. The initial condition is shown as a dotted line and the remaining time-steps are the solid lines with a darker shade representing a later time point. (a) Concentration profile for TNAP, the concentration rises and then falls. (b) Concentration profiles for PP_i, over time the concentration decreases and then slightly increases. (c) Concentration profiles for P_i over time. The slope of the profiles increases over time and then slightly decreases. (d) Magnified image of the concentration profiles for P_i showing the movement of the right boundary.

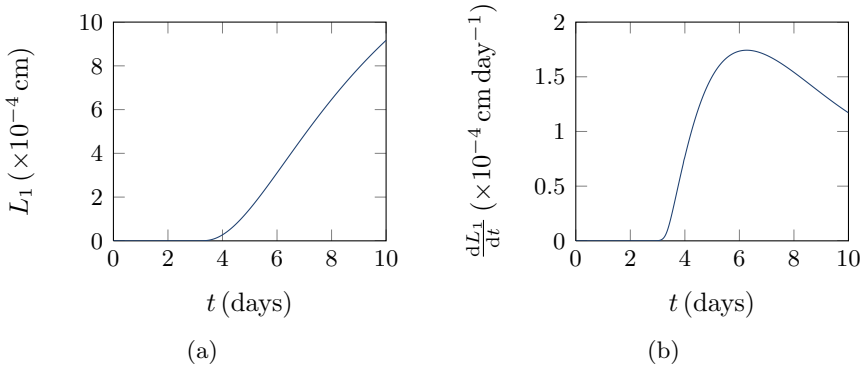

Figure 5.11: (a)Position of the mineralisation front. (b) Velocity of the mineralisation front. We see that mineralisation does not begin to occur until 3 days have passed.

100 days the final values for the concentration of TNAP due to this increase were only around $9.8 \times 10^{-5}\,\mathrm{g\,ml^{-1}}$.

The $\mathrm{PP_i}$ starts at a high level and initially decreases rapidly. As before the minimum of $\mathrm{PP_i}$ concentration lags the maximum of the TNAP concentration. The minimum occurs at $t = 6.3$ days and corresponds to a $\mathrm{PP_i}$ concentration of $0.35 \times 10^{-9}\,\mathrm{mol\,ml^{-1}}$. Following this the solution rises to reach a local maximum of $0.46 \times 10^{-9}\,\mathrm{mol\,ml^{-1}}$ just after 9 days have elapsed. After this, as with the TNAP concentration, there is another small oscillation visible. Following the visible decay of the oscillations the concentration has a very slow increase in value.

The profiles for $\mathrm{P_i}$ appear close to linear, with the slope dependent on the speed of the boundary. We see that the slope is initially zero, and remains that way until the onset of mineralisation, at about day 3 (see Figure 5.11). At this point the gradient increases quickly as the speed of mineralisation increases. The speed of the mineralisation front hits a maximum at day 6 and correspondingly after this point the gradient of $\mathrm{P_i}$ decreases again. If we follow the long term behaviour of the gradient there are some further oscillations, but following the decay of these oscillations there is a general slow increase in the slope of the profile corresponding with the slow increase in the speed of the boundary that occurs.

In Figure 5.11 the position and velocity of the mineralisation front is shown. We see that mineralisation does not begin to occur until after 3 days. This delay is expected and physiologically realistic. These simulations represent

an artificial problem where a group of uniformly non-mineralising cells are switched on to become mineralising cells at time $t = 0$ and begin expressing high levels of TNAP accordingly (in the context of our model this could be seen as the switch from $\bar{\beta} = 0$ to $\bar{\beta} = 0.5$). Following this switch there is a period of time in which the cells act to produce an environment that is conducive to mineralisation, that is a low ratio of $\mathrm{PP_i}$ to $\mathrm{P_i}$. This could be considered as being similar to the circumstances encountered in *in vitro* cell cultures. Here cultures of cells are treated with chemicals which induce mineralisation and the resulting effects on the cells are observed. Whilst the results from these assays varies with the precise experimental procedure used, there are experiments where mineralisation was observed in less then 5 days, which is consistent with our results (Maeda et al. 2001, Orimo & Shimada 2006, Stanford et al. 1995).

5.8.6 Speed of Mineralisation

The speed at which the mineralisation front moves is consistent with the choice of parameter λ, however, unsurprisingly on the scale of the domain of these simulations, the mineralisation front appears to barely move. The choice of a large domain was a deliberate one, based on the geometry of the callus observed in the sheep osteotomy model. In these experiments after 2 weeks mineralised bone is visible in a range of 4–5 mm from the pre-existing cortical bone. Thus the speed of mineralisation observed in our simulations is not consistent with experimental observations.

In their paper for mineralisation of endosteal implants (Prokharau et al. 2012) assumed that the new mineral front was advancing at a rate in the order of $10\,\mu\mathrm{m\,day^{-1}}$. We take this a a more physically realistic value for the mineralisation rate and investigate the effect of changing the parameters of our model in order to achieve this mineralisation rate. In particular we focus on the roles of λ, the maximum speed, and I_M, the mineral density, on the mineralisation rate. In particular the relationship between the mineral density and the mineralisation rate is of interest as bone that is formed rapidly is less dense than bone that is formed more slowly.

The parameter λ was determined based on the mineral apposition rate (MAR) measured for goat distraction osteogenesis. Healing during distraction osteogenesis is similar to that observed in fracture healing, however a key difference

is that most new bone is formed through an intramembranous pathway. At first glance the MAR would appear to be an appropriate measure to use to build our model. The standard method used to calculate the MAR is to label the bone with two (or more) different fluorescent labels separated by a period of time. These labels bind to calcium and become incorporated into the newly forming bone. When viewed under an epiflourescent microscope both labels will be apparent. To find the MAR the distance between the differently labelled surfaces can be measured and then divided by the time between the labelling (van Gaalen et al. 2010, Parfitt et al. 1987). The labels are taken up quickly by the bone and tend to remain in the body for only a short period of time. Generally the interfaces of the labels are sharp, however when bone is forming rapidly, such as in fracture healing, they become more diffuse making measurement more difficult. Additionally there is the risk that newly formed bone will be turned over due to the commencement of remodelling before a tissue sample can be made.

Further influencing this is the geometry of the newly formed intramembranous bone. The new bone has a woven appearance formed by interconnected rods that resemble trabeculae. The new bone growth starts with bony spicules, and it is possible that the rate of mineral formation on these spicules is not uniform. For example mineralisation may be occurring faster at the tip than the sides of the spicule. We must also remember that the histomorphometric measurements used to calculate the MAR are taken from 2D slices of a 3D callus, so we will never be able to see the complete picture.

As a first attempt to achieve a faster mineralisation rate with our model we increase the parameter λ by a factor of 10, to give $\lambda = 2.2 \times 10^{-3}\,\mathrm{cm\,day^{-1}}$. We see in Figure 5.12 that the increase in λ has provided a small increase in the speed of the mineralisation front. Indeed increasing λ by 1000 times to $\lambda = 2.2 \times 10^{-1}\,\mathrm{cm\,day^{-1}}$ less then doubles the maximum speed achieved.

This result tends to indicate that other factors are also influencing the speed of the front. Examining the boundary conditions for both the speed of the boundary and $\mathrm{P_i}$ reveals that as the boundary moves faster more $\mathrm{P_i}$ is lost at the boundary. This in turn increases the ratio of $\mathrm{PP_i}$ to $\mathrm{P_i}$ slowing down the bone formation. This suggests that if we considered the newly formed bone to be less dense, that is we take a lesser value of I_M, then the mineralisation speed will increase. The parameter $I_M = 0.29 \times 10^{-3}\,\mathrm{cm\,day^{-1}}$ was taken based on

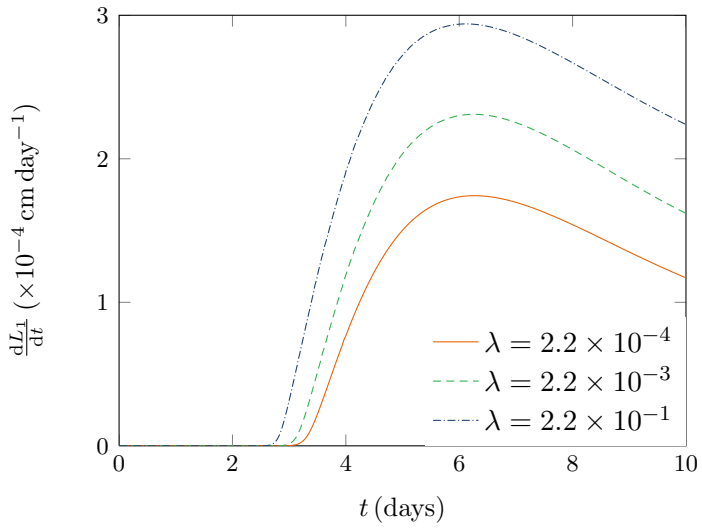

Figure 5.12: Velocity of the mineralisation front for increasing values of λ. We see as λ increases the speed of the mineralisation front also increases, however this is not a strong effect.

the density of established cancellous bone, whereas the newly formed woven bone observed in fracture healing is likely to have a lower density(Currey 2002).

In Figure 5.13 we show the effect of decreasing I_M on the speed of the boundary. We see that decreasing the mineral density to $I_M = 2 \times 10^{-1}\,\text{mol}\,\text{ml}^{-1}$ gives a small increase in the mineralisation speed. With a further decrease to $I_M = 1 \times 10^{-3}\,\text{mol}\,\text{ml}^{-1}$ we see that the curve has a flattened top, where the speed stays at $2.2 \times 10^{-4}\,\text{cm}\,\text{day}^{-1}$ for a period of days. This is the maximum speed determined by the parameter λ and shows that for decreased I_M the parameters λ is the limiting factor on the mineralisation speed.

We now observe the effect of changing both the mineral density and maximum speed of the mineralisation front. Combining both a decrease in the mineral density to $I_M = 1 \times 10^{-3}\,\text{mol}\,\text{ml}^{-1}$ and an increase in the maximum front speed $\lambda = 2.210^{-3}\,\text{cm}\,\text{day}^{-1}$ yields the velocity profile shown in Figure 5.14. We see that the combined effect of both increasing the maximum mineralisation speed λ and decreasing the mineral density I_M results in a much greater increase in the speed of the mineralisation front than was achieved when they were considered individually. The maximum speed achieved is $6.1 \times 10\,\text{cm}\,\text{day}^{-1}$, this is closer to the value $10\mu\text{m}\,\text{day}^{-1}$ cited in (Prokharau et al. 2012). A fur-

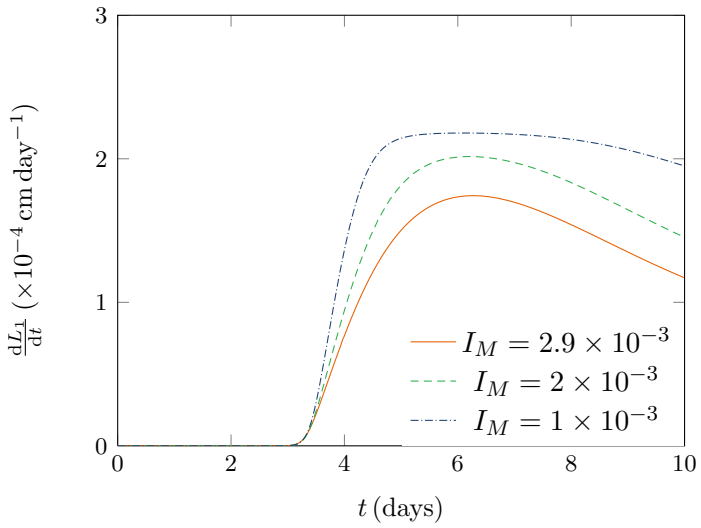

Figure 5.13: Velocity of the mineralisation front for decreasing values of I_M. We see that as I_M decreases the speed of the boundary increases.

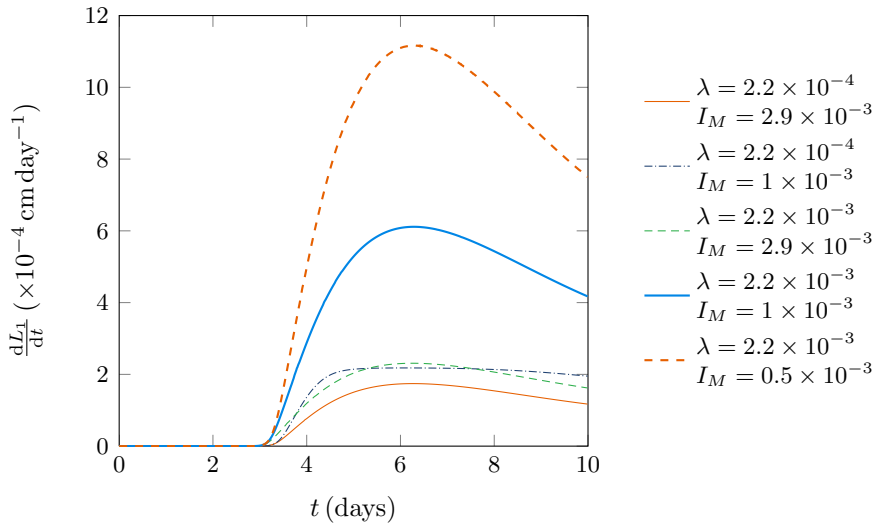

Figure 5.14: Velocity of the mineralisation front showing effect of both increasing λ and decreasing I_M.

ther decrease of the mineral density to $I_M = 0.5\,\text{mol ml}$ results in a maximum speed of $11\mu\text{m day}^{-1}$.

By varying the parameters λ and I_M we were able to significantly increase the speed at which the mineralisation front moved, to a speed which is likely more realistic. These alterations that were made to the parameters were justified

from a biological perspective. Whilst we did not show the concentration profiles for the chemical species over time, we note that other then the increased speed of the mineralisation front, the general behaviour did not vary significantly to that described previously (Section 5.8.5). These results suggest that in our model the availability of P_i is a limiting factor in the movement of the mineralisation front. This indicates that for new bone mineral to form there is a requirement for not only a reduction in the concentration of PP_i, but also sufficient P_i available for the new mineral to form.

5.8.7 Effect of Domain Size

We are also interested in the effect of the domain size on the concentration profiles and movement of the mineralisation front. In our original construction of the domain the left boundary represents the mineralising surface and the right boundary the periosteum. At the onset of the fracture healing cascade, cells in the periosteum begin proliferating, driving the periosteum away from the bone surface. As healing progresses the mineralised callus approaches the periosteum once again. Thus during the healing process the distance between the periosteum and the mineralisation front varies depending on many different factors. As such we wish to determine the effect changing the domain size has on our simulation results.

We observe these effects by altering the initial length of the domain by changing L_2. If we halve the initial length of the domain such that $L_2 = 0.1\,\text{cm}$ and keep all other parameters as in Tables 5.1–5.3 then the results are shown in Figure 5.15. These results do not appear to differ substantially to those obtained for an initial domain length of 0.2 cm.

If we further decrease the initial size of the domain we begin to have a greater influence on the concentration profiles and the speed of mineralisation. We further decreased the initial length of the boundary to 0.02 cm. In Figure 5.16 we show the concentration profiles for TNAP and PP_i over a period of 10 days, as well as the speed of the mineralisation front over 30 days. We see that this decrease in domain length has had a significant effect on our results. The concentration for PP_i does not decrease to the levels seen in the original simulation. This is because the shorter domain combined with the fast diffusion speed of PP_i and the PP_i source at the periosteum results in an overall increase in PP_i concentration across the domain. We additionally illustrate two

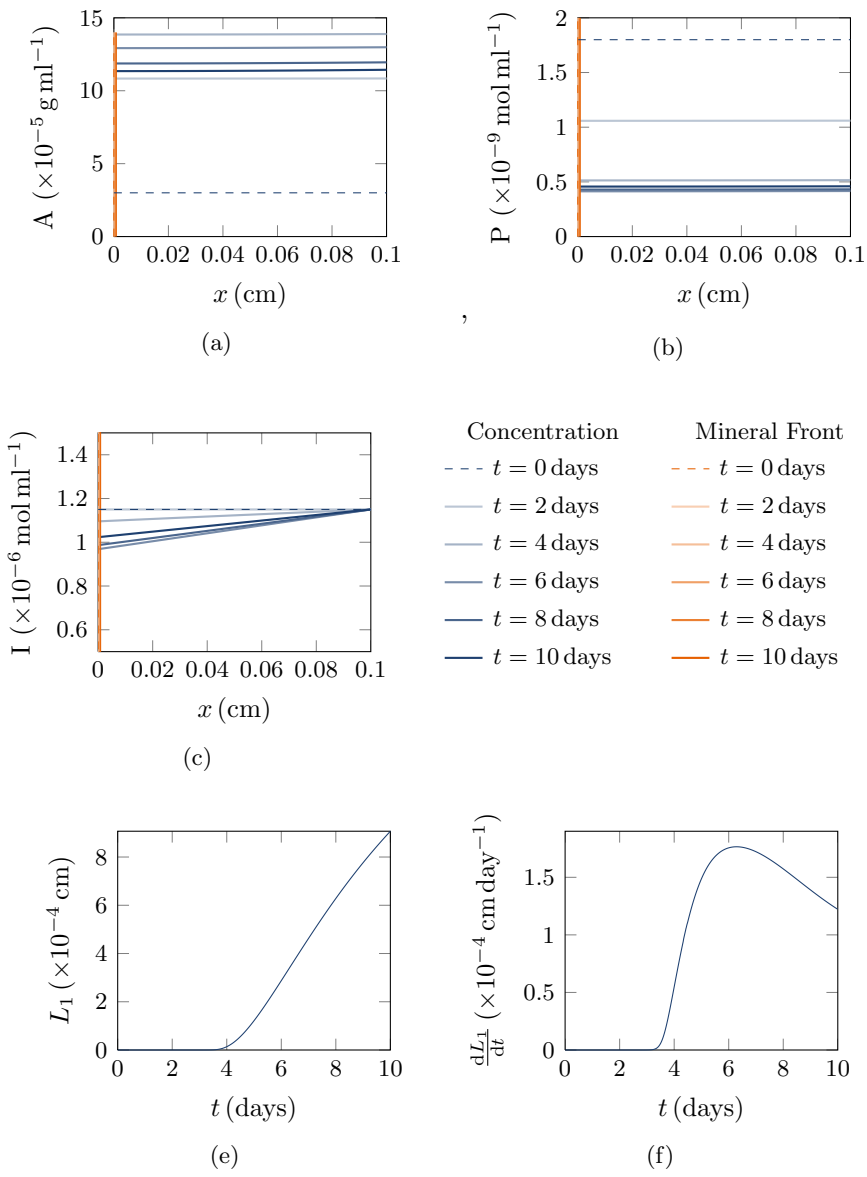

Figure 5.15: Concentration profiles over time for a domain with an initial width of 0.1 cm, we note that there is no substantial difference in the results seen here and those for a initial domain length of 0.2 cm as seen in Figures 5.10 and 5.11. The blue lines represent the concentration profiles and the orange lines represent the location of the boundary. We show the profiles at $t = 0, 2, 4, 6, 8, 10$ days. The initial condition is shown as a dotted line and the remaining time-steps are the solid lines with a darker shade representing a later time point. We show the concentration profiles for (a) TNAP, (b) PP_i and (c) P_i over time. (e) Position and (f)velocity of the mineralisation front.

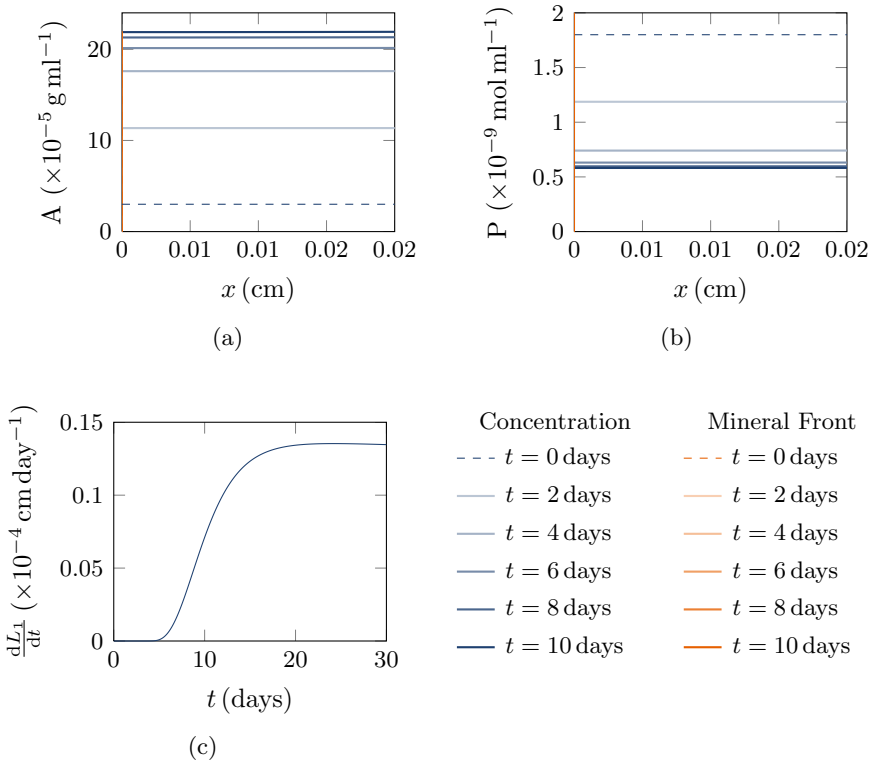

Figure 5.16: Concentration profiles over time for a domain with an initial width of 0.02 cm. The blue lines represent the concentration profiles and the orange lines represent the location of the boundary. We show the profiles at $t = 0, 2, 4, 6, 8, 10$ days. The initial condition is shown as a dotted line and the remaining time-steps are the solid lines with a darker shade representing a later time point. We show the concentration profiles for (a) TNAP, (b) PP_i and in (c) we show the velocity of the mineralisation front.

consequences of the higher levels of PP_i. Firstly the concentration of TNAP is significantly raised as an increase in PP_i increases the production rate of TNAP by the osteoblasts. We also observe that the temporal behaviour does not match that shown previously. In the original simulations we observed a sharp increase in TNAP concentration followed by a slower decrease. However here we see that TNAP concentration continues to increase over time, initially rapidly, before then slowing down. Another consequence of the higher concentrations for PP_i is that the mineralisation speed, shown in Figure 5.16(c) is reduced compared to the longer domain. We show the mineralisation speed over a period of 30 days. This illustrates that the onset of mineralisation is slightly delayed compared to the longer domain and that the maximum min-

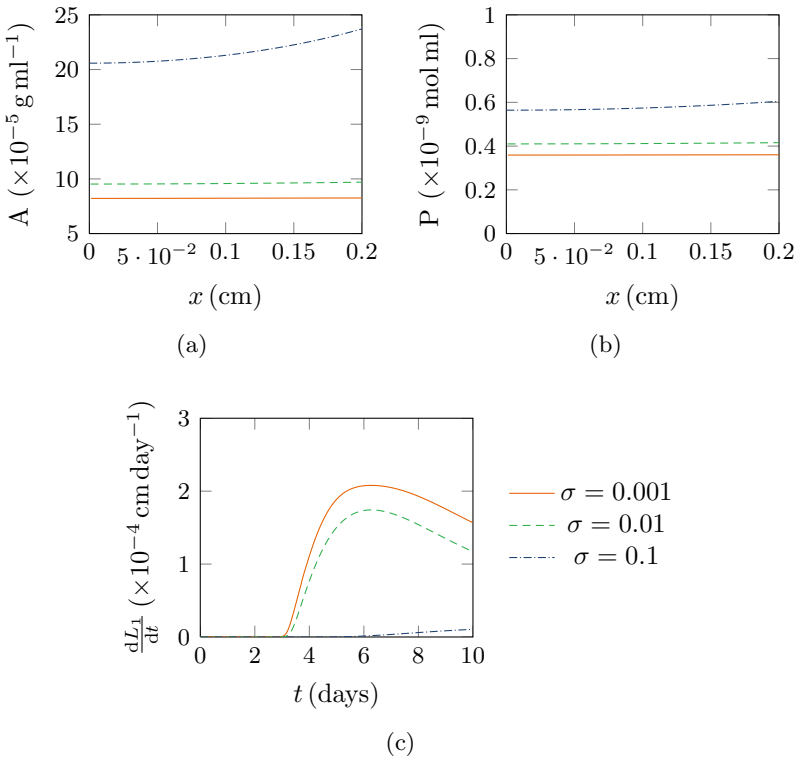

Figure 5.17: Effect of parameter σ on mineralisation. (a) and (b) concentration of ALP and PP_i respectively after 10 days. (c) Speed of the mineralisation front. We see that decreasing σ to $\sigma = 0.1$ significantly impedes mineralisation.

eralisation speed is $= 0.13 \times 10^{-4}\,\mathrm{cm\,day^{-1}}$ and is achieved at around 24 days. Following this maximum the speed continues to decrease slowly.

5.8.8 Effect of the Parameter σ

The overall higher concentrations achieved in the smaller domain were in part caused by the source of PP_i at the boundary. The boundary condition used at the periosteum for the concentration of PP_i took the form a Newton's cooling type condition

$$\frac{\partial P}{\partial x} = \sigma(P - P_0), \tag{5.58}$$

with the parameter σ representing how permeable the periosteum is to the flow of PP_i. The larger σ is the greater the amount of PP_i that diffuses through the periosteum. In Figure 5.17 we show the effect of varying σ on the concentration profiles and the speed of the mineralisation front, whilst all other parameters

were held as in 5.1–5.3. Figures 5.17(a) and (b) show the concentration profiles of TNAP and PP_i after 10 days for varying values of σ and Figure 5.17(c) shows the effect of varying σ on the speed of the mineralisation front. We see that decreasing the parameter σ from $\sigma = 0.01\,\mathrm{cm}^{-1}$ to $\sigma = 0.001\,\mathrm{cm}^{-1}$ does not provide much change in either the concentration profiles or the speed of mineralisation. However an increase to $\sigma = 0.1\,\mathrm{cm}^{-1}$ results in a overall increase in the concentration of PP_i across the domain. As in the case of the shortened domain this has consequences for the concentration of TNAP and the mineralisation speed. We see that the concentration of TNAP is at least twice as large and also that there is a rise in the concentration at the right boundary. This rise corresponds to the smaller rise visible in the PP_i concentration at the right boundary but is further accentuated in the TNAP profile due to the low diffusion rate. We also see that the speed of the mineralisation front is significantly reduced due to the increased concentration of PP_i. These results again demonstrate the importance of the removal of PP_i for mineralisation to occur.

5.9 Summary

The removal of the mineralisation inhibitor PP_i due to the cleaving actions of TNAP has been widely identified in the biological literature as key to the regulation of new mineral formation. Furthermore as bone is comprised of hydroxyapatite a sufficient supply of P_i is required to create the new bone mineral. We developed a simple mathematical model for new mineral formation based on the relationship of TNAP, PP_i and P_i.

Initially we considered a purely kinetic model for TNAP, PP_i and P_i without considering spatial effects. This model appeared to qualitatively match expression of TNAP in mineralising cultures of osteoblasts. The presence of high levels of TNAP induced a reduction of the concentration of PP_i, a known mineralisation inhibitor. The removal of PP_i is seen as a key requirement for mineralisation to occur. We also considered a case where TNAP expression due to the presence of PP_i had been suppressed. As TNAP is a marker of osteoblastic differentiation this could be seen as the dynamics when considering a population of non-mineralising osteoblast progenitor cells. When the TNAP expression was suppressed the PP_i concentration remained within the range of normal serum concentrations and thus it is reasonable to expect that

no mineralisation could occur. This model demonstrates the importance of TNAP as produced by the osteoblasts to the mineralisation process. Further to this the model supports the hypothesis that the dominant role of TNAP in fracture healing is to remove PP_i rather than to create P_i ions.

Extending the kinetic models, we developed a model for the movement of a mineralising front across a domain. Again the model was simplistic only considering the effect of the concentrations of TNAP, PP_i and P_i on the speed of mineralisation. This model reinforced the importance of the removal of PP_i for mineralisation to occur. This was demonstrated through a series of simulations varying the domain size and the source of PP_i at the right hand boundary.

A key result from this model is the effect of the mineral density on the speed of mineralisation. Our initial choice of parameters resulted in an extremely slow speed of mineralisation which was physiologically unrealistic. This led to an investigation of some of the parameters likely to affect the mineralisation speed. These investigations revealed that a decrease in the mineral density of the new bone led to an increase in the mineralisation speed. This would appear to support a view of the overall healing strategy of bone, where new less dense bone is produced rapidly to stabilise the gap, but the remodelling process to restore the bone to its original dense cortical structure takes a much longer time.

6

Summary and Future Directions

Bone formation during fracture healing is a complex process, that is currently poorly understood. The speed at which new bone forms and the quality of this new bone is a key issue for patient outcomes. Increasing human understanding of the fracture healing cascade is a key step towards developing clinical interventions to improve patient outcomes.

Fracture healing is a multiscale process, that is both spatially and temporally heterogeneous. Experimental data is difficult to obtain and has many limitations. The nature of fracture healing means that it is difficult to observe the processes that are occurring in an *in vivo* experimental model. In these experiments histological sections can be used to observe tissue formation across the entire callus but to obtain these sections the animal must be sacrificed, and hence these sections represent a single picture of a callus at a single time point. On the other hand *in vitro* experiments such as cell cultures can be used to understand behaviour on a cellular scale, but there is no guarantee that the behaviour of cells in a Petri dish resembles the *in vivo* behaviour of these cells. Mathematical modelling is a tool that can be used to explore ideas and hypotheses that would otherwise be difficult to quantify from experimental work.

There is a fundamental hypothesis of bone formation stemming from the work of (Pauwels 1980), that cellular differentiation is due to the mechanical stresses and strains placed on the MSCs present at the fracture gap. This hypothesis is incomplete as it ignores the effect of bioregulatory factors such as proteins and growth factors that influence the formation of new bone tissue. Mathematical models that consider these bioregulatory effects exist but they examine the callus scale dynamics of fracture healing.

Instead we have built models for aspects of fracture healing as they occur at a cellular level. These models are designed to illustrate specific elements of the healing cascade. In particular we focused on the differentiation of MSCs to become osteoblasts and the mineralisation of new bone tissue to better understand the mechanisms that drive these processes to occur. The outcomes of these models is summarised in this chapter. We also indicate some future directions to extend the research presented to further increase the understanding of the biological processes that are occurring.

6.1 Summary

In Chapter 1 we set out two key objectives for this thesis. These objectives were to build mathematical models for two different processes, cellular differentiation and mineral deposition, that occur during intramembranous bone formation in fracture healing in order to help increase the knowledge and understanding of the bioregulatory mechanisms that drive these processes. In the following we summarise the work presented in the thesis with specific mention of how this work met the outlined objectives.

In Chapter 2 we presented a brief overview of fracture healing and some of the biological processes that occur in the callus region, as well as a review of existing mathematical models of fracture healing and bone formation. Examining the biology of fracture healing revealed that intramembranous bone formation occurs in regions of the callus that have a high mechanical stability. This indicates that bioregulatory factors are strong driving forces behind the events that occur during intramembranous bone formation. In our examination of the biological literature we identified two bioregulatory feedback loops for the regulation of cellular differentiation and mineralisation. The differentiation of osteoblast progenitor cells to become mature osteoblasts is enhanced by the presence of BMP ad inhibited in the presence of noggin. For mineralisation to occur it is required that the mineralisation inhibitor PP_i is removed, this is facilitated by the osteoblasts through the production of the enzyme TNAP. Both of these bioregulatory loops are well established as playing a role in bone formation but to the best of our knowledge they have yet to be fully explored through mathematical modelling.

Our review of the existing models of fracture healing revealed that these mod-

els focus on modelling the entire callus as fracture healing occurs. These models consider a variety of stimuli for driving fracture healing, from mechanical stresses or strains, to growth factor concentrations to hybrid models that consider both mechanical and biological factors. Because of the complexity of callus growth and the many complex and coupled processes that are occurring these models tend to be phenomenological instead of focusing on the underlying mechanisms that are driving the healing to occur. In line with our aims established in Chapter 1, to gain insight into the bioregulatory factors affecting two key processes, cellular differentiation and mineralisation, as they occur during intramembranous bone formation, we decided to take a different approach in our modelling of intramembranous bone formation. In our modelling approach we focused on building models that explored the regulation of a specific aspect of intramembranous bone formation, either cellular differentiation or mineralisation, as a result of bioregulatory factors that we identified from the biological literature.

In Chapters 3 and 4 we addressed the first objective and presented our model for cellular differentiation. In Chapter 3 we described a model where cellular differentiation of progenitor cells to osteoblasts was regulated by a chemical pre-pattern established by BMP and noggin, two proteins that have been implicated with cell differentiation during intramembranous bone formation. Following the development of the model we reduced the underlying relationship between BMP and noggin to a Turing pattern problem which allowed for analysis of the patterning ability of the model. This analysis revealed that as the cells populations changed due to differentiation that the chemical pattern in BMP should remain at the same frequency. This is an important result when we consider the model in its biological context. We also observed that when simulating our model that the spatial and temporal appearance of the patterning seemed to be consistent with our expectations based on histological observations of the callus region.

We further extended this model to more accurately represent the callus domain in Chapter 4. In particular we investigated the influence of a BMP source at the boundary representing the cortical bone, and the effect of domain growth on the patterning that is apparent in our model. We first considered a static domain with a source of BMP at the cortical bone surface. These simulations allowed us to predict the speed of the front of differentiation. Using

this method the front of differentiation predicted by our model was found to move at speed much greater then the expected growth rate of the callus. Also problematic in these simulations was that the resultant patterning in the cell species appeared to be more stripe-like, which is not consistent with our view of the callus region. However as we moved to a growing domain, where we assumed that the domain grew due to progenitor proliferation at the periosteum, we again recovered a spotted pattern. When we considered domain growth to be similar to that observed in a sheep callus (i.e. much slower then the speed of the differentiation front), a well defined spotted pattern appeared with only transient strip-like features. Another interesting result identified in Chapter 4 was the effect of a BMP source on only half of the left boundary. This simulation demonstrated how specific boundary conditions can influence the eventual distribution of spots. This indicates that growth factors that are released from the damaged bone or other signalling molecules that diffuse from the fracture gap are likely to influence the structure of the intramembranous bone.

Our original hypothesis for objective one was that cellular differentiation occurred in a non-uniform fashion across the callus region in response to a chemical pre-pattern and that the heterogeneities in the osteoblast population would guide and shape the appearance of the new woven bone. Whilst we did not explicitly model the new bone formation we would expect that the pools of osteoblasts observed in our model would present as the first sites where mineralisation would occur, and as the mineral structure grew that these pools would shape the new bone. Our model indicates that the regulation of the differentiation by BMP and noggin gives rise to patterns that appear consistent with the structure of intramembranous bone observed in histology, further increasing the evidence for the role these species play in intramembranous bone formation.

In Chapter 5 we addressed the second objective of developing a model for mineralisation. The relationship between TNAP and PP_i has been widely identified in the literature as playing an important role in the regulation of mineral deposition onto the collagen matrix. We used this relationship as the basis for a new model of mineralisation. In addition we focused on the effect of P_i rather calcium on the formation of new mineral.

Initially we examined a simple kinetic model for TNAP, PP_i and P_i. Having

determined appropriate parameters, when simulated, the system went from an initial condition of low TNAP and high PP_i to a state where TNAP was high and PP_i was low. The low level of PP_i is important as this is what creates an environment that is conducive to mineralisation. Furthermore we note that TNAP concentration levels qualitatively match experimentally determined profiles for TNAP activity in cell cultures. It has been proposed that the role of TNAP during mineralisation is to both decrease the levels of PP_i and increase the local P_i concentration, with most recent research indicating that the first of these is the dominant role. Our results lend support to this theory.

We further extended this model to include spatial effects and explicitly model the movement of the mineralisation front. For this model the choice of appropriate parameters and boundary conditions became difficult and this had a significant effect on the behaviour of the model. There are two outcomes from this model that are relevant to the biological context. The first was that decreasing the mineral density of the new bone increased the speed of the mineralisation rate. The second was that the model demonstrated that a sufficient supply of P_i was required for mineralisation to occur.

6.2 Future Work

There are many additions, improvements and extensions that could be made to the models presented in this thesis.

Our model for cellular differentiation is only capable of producing a spotted distribution of cellular differentiation. Inclusion of BMP saturation could give rise to a labyrinth like patterns that are commonly observed in Turing patterns. These labyrinth patterns could bear a closer resemblance to the appearance of the new intramembranous bone.

It would also be of interest to include some form of new bone tissue formation to observe how the heterogeneities in the osteoblast population help shape the structure of the new intramembranous bone. This does not necessarily have to use the mineralisation model we presented in this thesis, although this is discussed below. A more simple description of new bone formation being proportional to the osteoblast density such as is seen in other fracture healing models would suffice.

If we consider the model for mineralisation, whilst the kinetics for TNAP, PP_i and P_i seemed to give realistic results when considered without spatial effects, our attempts to include the spatial effects were less successful. Future work should be conducted to improve this model, in particular the determination of appropriate parameters and boundary conditions. Further to this relevant cell species, osteoblasts and progenitor cells, and even the collagen matrix could be included in the model. Initially the cells could be included with a spatially heterogeneous distribution across the domain with more osteoblasts closer the bone surface and more progenitors at the periosteum.

Taking this further, we could consider the incorporation of the mineralisation model with the cellular differentiation. Implementing this in 2D would introduce several numerical difficulties in the simulation of the model. Ideally this hybrid model would be capable of replicating the woven appearance of new intramembranous bone. However this new bone has a complex, changing topology which would pose difficulties for many front tracking numerical schemes.

One numerical method that may be ideally suited to this problem is the level set method. Developed by Osher & Sethian (1988), the level set method is an interface tracking method that works by embedding the interface into a higher dimensional surface and evolving the surface and tracking the level curves (sets). One of the big advantages of the level set method is that it handles changes in topology with ease, which is important in the context of new intramembranous bone formation.

Along with the tracking of the bone surface, another potential difficulty would be the numerical treatment of the boundary conditions at the bone surface. If the finite volume method was used in conjunction with the level set method, the control volumes intersected by the bone surface would become irregular in shape. Appropriate numerical methods would then need to be used to approximate the area of the irregular cell and the flux lost through the bone surface.

It would also be of interest to further verify our models with experimental data. This could be done through the use of *ex vivo* models of bone growth and formation, where the mechanical and biochemical environment are controlled. In particular the hypothesis of chemical pattern formation leading to heterogeneities in the cell population could be further tested through the

collection of data regarding the spatial distribution of biochemicals such as BMP and noggin as the bone tissue forms.

Appendices

A

An Overview of Bone Biology

Bones play many important roles in the body from structural support to maintaining calcium homeostasis. Bone fractures impede the bones ability to perform many of these functions. Thus the ability of the fracture repair process to restore the original function of the bone is important. In this appendix we provide some background information about the structure and biology of bone and its formation.

A.1 Bone Function

Bone has many functions within the body. Perhaps the most obvious that they form the skeleton which provides structural support for muscles and organs, as well as protection for important organs. In addition to these mechanical roles bones also play an important role in maintaining calcium homeostasis in the body. The bone mineral acts as a pool of calcium that can be accedes in times of calcium depletion. Bone also houses bone marrow in its interior, which produces new blood cells.

A.2 Bone Classification

Human bones are often classified based on there shape and structure. They are typically described as belonging to one of the following categories: long, short, flat, irregular and sesamoid (Rizzo 2011, Gosling et al. 2008).

Long Bones These are the long thin bones that form most of the bones in the limbs. They have a well defined structure and consist of a long thin hollow shaft comprised of cortical bone, with wider ends where the cortical bone thins surrounds cancellous bone.

Flat Bones These bones are flat and platelike. They consist of a cancellous bone sandwiched between two sheets of cortical bone. Bones such as the cranium (skull) and scapula (shoulder blade) are flat bones.

Short Bones These bones are as long as they are wide and are often roughly cuboidal in shape. They have a thin outer layer of cortical bone surrounding cancellous bone. The tarsals and carpals in the ankle and wrist are examples of short bones.

Sesamoid Bones These are bones that are embedded in a tendon. They are similar in structure to short bones. They act to increase the mechanical effect of the tendon and reduce the amount of wear on the tendon. In humans the patella (knee bone) is an example of a sesamoid bone.

Irregular Bones These are bones that do not fit into any of the above categories, such as the vertebrae. They often have complicated and irregular geometries. Structurally they consist of cancellous bone in a thin shell of cortical bone.

A.3 Bone Structure

Based on the descriptions above bones can be broadly classified into two categories, those that are long bones and have a well defined structure and those that are not long bones. These bones have irregular geometries and structurally are composed of a thin cortical shell surrounding cancellous bone. Most models (both biological and mathematical) of fracture healing focus on mid shaft fractures of long bones. Within this thesis we continue that trend, and will focus on these types of fractures.

A.3.1 Long Bone Structure

The structure of long bones is well defined. A typical schematic is shown in A.1. The general structure can be described as a long, thin shaft, known as the diaphysis, connecting two wider ends, known as the epiphysis or heads of the bone.

The boney material that makes up the diaphysis is known as compact or cortical bone. This cortical bone is dense and well structured giving strength to the bone. The cortical bone forms a hollow cylindrical shape. The hollow

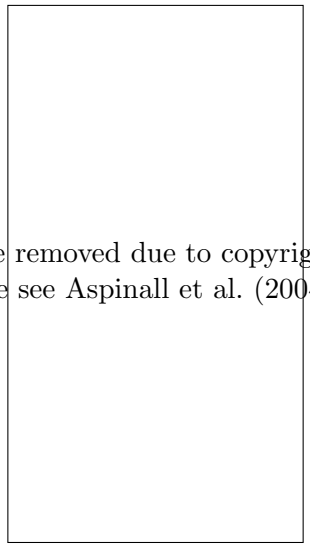

Figure A.1: Typical schematic of a long bone, (Aspinall et al. 2004).

inside the diaphysis is known as the medullary cavity and contains the bone marrow. The cortical bone is surrounded by two membranes. The first on the exterior of the bone is known as the periosteum. This fibrous membrane contains many potential bone cells for required for bone repair or remodelling. The other membrane is the endosteum which separates the cortical bone from the marrow.

The epiphysis has a different structure. Here the cortical bone shell is much thinner and the interior space is filled with cancellous bone, also known as spongy bone due to its appearance. The epiphysis also contains the growth plates. As an immature individual grows the cartilage in the growth plate also grows and becomes mineralised bone via a process known as endochondral ossification. As the individual matures, the cartilage becomes fully mineralised and the bone growth is halted. In addition the ends of long bone are also covered in articular cartilage. This cartilage allows the bone to move smoothly during movement and provides some shock absorption for the bone. It is the degradation of this articular cartilage that leads to osteoarthritis.

A.3.2 Cortical and Cancellous Bone

Cortical bone is the hard, dense bone that comprises the majority of bone mass and is responsible for most of the bones structural strength (Jee 2001). Mature cortical bone is comprised of many microscopic layers, laid together

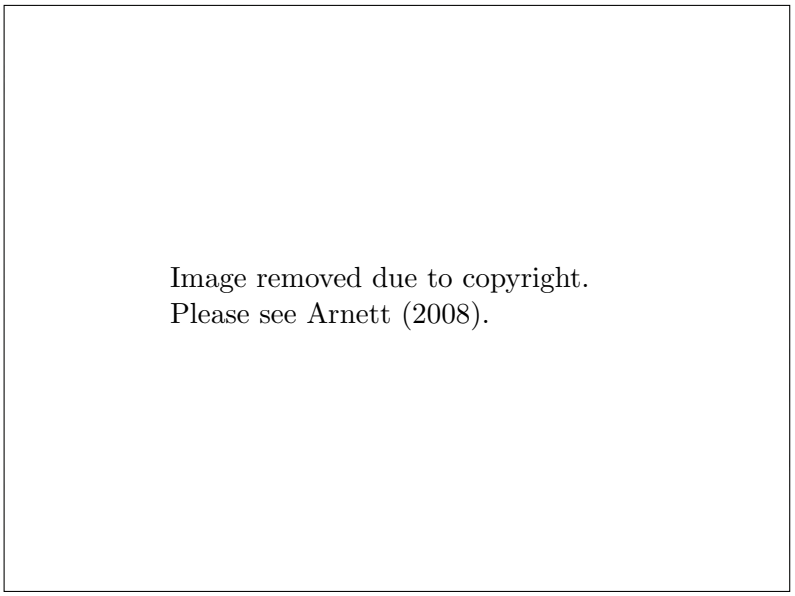

Figure A.2: Transverse section through cortical bone showing the osteon structure (Arnett 2008).

like plywood. These layers are known as lamellae and are 3-7μm thick. Within these lamellae the collagen fibres and mineral crystal lattice are well aligned, however there is a difference in alignment between adjacent lamellae Most of these lamellae form in concentric circles surrounding a channel known as the Haversian canal which contains the blood vessels and nerves of the bone. A group of lamellae surrounding a Haversian canal is known as a osteon.

An illustration of a osteon structure is shown in Figure A.2. This figure is representative of a transverse section taken through cortical bone. The concentric nature of the lamellae can be seen. Osteons are cylindrically shaped and run longitudinally with the bone. They are typically around 200-250μm in diameter (Jee 2001).

Cancellous bone, has a much less defined structure. It is constructed from a network of rods and plates known as trabeculae. This network of trabeculae gives the cancellous bone a very porous structure. These interconnected pores contain red bone marrow, which is responsible for the production of red and white blood cells and platelets (Scanlon & Sanders 2011, Doblaré et al. 2004). Due to its structure cortical bone has a much larger surface area to volume ratio. This allows the cancellous bone to be formed or resorbed quickly to help maintain calcium and other mineral homeostasis (Clarke 2008).

A.3.3 Important Cells

There are many different cell types that are present during different stages of bone development, maintenance and reparation. The key bone cells include osteoblasts, osteoclasts and osteocytes. Other cells which play important roles during bone formation include chondrocytes, mesenchymal stem cells (MSC)s and endothelial cells.

Osteoblasts Osteoblasts are the bone forming cells. They differentiate from MSCs through a progression of stages, from MSC to committed osteoblast precursor to pre-osteoblast to mature osteoblast (Majeska 2001). They are polarised, cuboidal in shape and about 15-30μm thick. Mature osteoblasts rarely proliferate (Jee 2001).

Mature osteoblasts produce the collagen matrix of bone tissue and control is alignment, and regulate the mineralisation of this matrix. The functions of osteoblasts are known to be controlled by the presence of many different growth factors present during bone formation (Barnes et al. 1999).

Quiescent osteoblasts are present on the surface of bone tissue. These cells are sometimes referred to as bone lining cells. it is believed that these cells help maintain a separate region of bone fluid from the extracellular fluid. In this bone fluid the concentrations of calcium and phosphate ions can be more closely controlled, which in turn will regulate bone crystal growth (Jee 2001).

Osteocytes As the osteoblasts produce the bone matrix some may become trapped in the new matrix and turn into osteocytes. Osteocytes have small bodies but posses long cell processes spread through the bone matrix. This allows the osteocytes to sense changes in the bones mechanical loading, detect microdamage to the bone and signal other osteocytes or cells (Majeska 2001).

Osteoclasts Osteoclasts are giant multinucleated cells that are able to resorb bone. They attach tightly to the bone forming an impermeable barrier, this gives rise to a sealed compartment between the cell and the existing bone surface. Within this compartment the osteoclasts create a highly acidic local environment. The acidic environment dissolves the

bone mineral releasing calcium and phosphate ions. The osteoclasts also secrete a range of proteases that digest the collagen matrix. By possessing the ability to free minerals from the bone matrix osteoclasts play a key role in maintaining calcium homeostasis (Jee 2001, Clarke 2008)

Mesenchymal Stem Cells Mesenchymal stem cells are multiplurent stem cells that have the ability to differentiate to form many different tissue types including bone, cartilage, bone marrow, muscle, tendons and ligaments. They can thus be found in all of these tissue types. The differentiation of these cells is controlled by different physical and chemical stimuli (Prendergast & van der Meulen 2001).

Chondrocytes These are cartilage forming cells. During endochondral bone formation a cartilage matrix is formed by chondrocytes and is then mineralised to form mineralised bone (Einhorn 1998).

Endothelial Cells These cells form the new blood vessels throughout the bone. Vascularisation occurs early during fracture healing in the same region as intramembranous bone is forming. The blood vessels spread toward the fracture gap and help to convert cartilage tissue into mineralised bone (Glowacki 1998). If insufficient vascularisation occurs during healing then it is likely that the fracture will not fully heal, resulting in a non-union (Augat et al. 2005).

A.3.4 Collagen and Mineral Structure

The noncellular component of bone is a matrix of collagen fibres that have been mineralised. The mineral is hard but brittle whereas the collagen matrix is soft and tough(resistant to fracture). The composite nature of bone tissue has the advantages of both of these material types to create bone tissue that is stiff and resistant to fracture (Fratzl et al. 2004, Ashby et al. 1995).

Bone mineral is typically described as an impure form of hydroxyapatite ($Ca_5(PO_4)_3(OH)$), other ions that are present in the mineral phase include magnesium, sodium and carbonate. As well as providing strength to bones, the mineral component of bone provides a pool of calcium and phosphate that can be accessed by the body when required (Boskey 2001).

Collagen I is the main organic component of bone and is expressed by osteoblasts. It is also the main collagen type found in skin and arterial walls. In

bone, the collagen molecules align themselves to form fibrils The molecules in these fibrils are aligned in staggered parallel lines. As part of this staggered structure between the end of adjacent molecule there is a 40 nm gap, known as a hole zone. These hole zones play an important role in mineralisation as they provide the first nucleation points for crystal growth (Mann 2001). The collagen matrix also contains many other non-collagenous proteins. Some of these proteins help aid mineralisation by attracting calcium or phosphate ions and acting as nucleation points for the hydroxyapatite growth (Boskey 2001).

A.4 Mechanism of Bone Formation

Bone can be formed by two different mechanisms, endochondral or intramembranous ossification. During endochondral ossification bone is formed through an intermediary cartilage stage, whereas in intramembranous ossification the new bone forms directly.

During development and growth endochondral ossification is responsible for the formation and lengthening of long bones. It also plays an important role in fracture healing. During fracture healing endochondral ossification occurs across the fracture gap, where there is little mechanical stability. Chondrocytes present form a cartilage matrix which stabilises the fracture gap. Through the process of endochondral ossification this cartilage matrix eventually becomes a boney matrix allowing the fracture gap to be bridged by bone.

Intramembranous ossification is where bone is formed directly by osteoblasts without an intermediary cartilage stage. Intramembranous ossification is responsible for the formation of flat bones such as the bones in the skull. In fracture healing intramembranous ossification occurs in regions of high mechanical stability. Here the new bone is formed appositionally on existing bone near the fracture gap.

B

Introduction to Turing pattern formation

From the spots on a leopard's skin to the skeletal structure of limbs, patterns are widely evident across nature. The development of form and structure in an organism is termed morphogenesis. Morphogenesis is most readily associated with the developing embryo however it can also occur during growth or tissue repair.

Turing pattern formation is one mechanism that has been proposed as a mathematical description of morphogenesis. Mathematical models for Turing pattern formation are well studied and there exists a series of known conditions that must be satisfied for patterning to occur. Through the work of Segel & Jackson (1972) and Gierer & Meinhardt (1972) it has been established that patterning only occurs in a two species system when there is local self-enhancement and long-range inhibition.

We can further derive a set of more rigorous conditions to determine whether patterning will arise. In the process of this we will also reveal other aspects of Turing patterning that influence the form of the final pattern.

B.1 Diffusion Driven Instability

These days Turing patterns are generally described as forming due to a diffusion driven instability. This occurs when a steady state for a system of equations is stable in the absence of diffusion, however when diffusion is included the steady state becomes unstable. A pattern is then formed as a new spatially heterogeneous stable steady state evolves (see Figure B.1(c)).

The idea that the inclusion of diffusion could give rise to spatial patterns is counter-intuitive as diffusion is typically seen as a stabilizing process. During

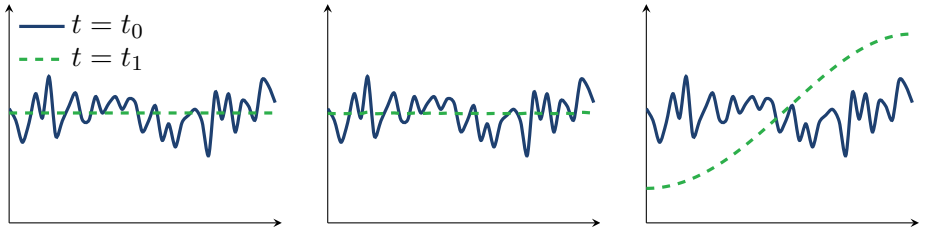

Figure B.1: Plots showing instability introduced by diffusion. When (a) diffusion or (b) reaction terms only are considered the solution tends to a spatially homogeneous state. When (c) both reaction and diffusion terms are considered the system tends to a spatially non-homogeneous steady state.

diffusion, matter moves from areas of high concentration to areas of low concentration. This results in a smoothing process and the entire region will, as $t \to \infty$, all be at the same concentration as illustrated in Figure B.1(a). Similarly perturbations from a homogeneous stable steady state for some given reaction will eventually return to the homogeneous steady state as in Figure B.1(b).

B.2 Turing Mechanisms

The following equations describe a general reaction diffusion system involving two species.

$$\frac{\partial A}{\partial t} = D_A \nabla^2 A + F(A, B) \tag{B.1}$$

$$\frac{\partial B}{\partial t} = D_B \nabla^2 B + G(A, B) \tag{B.2}$$

where A, B are the concentrations of two different chemicals, D_A, D_B are the diffusion coefficients of A, B respectively and F, G are the (non-linear) kinetics of the system. A and B are chosen such that A represents the slower diffusing chemical ($D_A < D_B$). The kinetics of the system describe the interaction between A and B. Some common kinetics that produce Turing patterns are Schnackenberg (Schnackenberg 1979) and Gierer-Meinhardt (Gierer & Meinhardt 1972).

Equations (B.1) and (B.2) can be nondimensionalised by setting $\mathbf{x}^* = \mathbf{x}/L$, $t^* = t/\hat{t}$ and $d^* = D_B/D_A$, where L is the typical length scale and $\hat{t} = L^2/D_A$.

We also set $u^* = A/\hat{A}$ and $v^* = B/\hat{B}$ as the dimensionless concentrations. The appropriate choice of $\hat{A}$, $\hat{B}$ is determined by the kinetics. This gives the general form

$$\frac{\partial u^*}{\partial t^*} = \nabla^2 u^* + \gamma f(u^*, v^*), \tag{B.3}$$

$$\frac{\partial v^*}{\partial t^*} = d^* \nabla^2 v^* + \gamma g(u^*, v^*), \tag{B.4}$$

where $f(u^*, v^*)$, $g(u^*, v^*)$ are the dimensionless kinetics and γ is a constant proportional to L^2/D_A, the exact form of which depends on the kinetics.

B.3 Conditions for Diffusion Driven Instability

Diffusion driven instability occurs when a steady state that is stable in the absence of diffusion becomes unstable when diffusion is present. As such it is possible to derive a set of conditions on the parameters in Equation (B.3) and Equation (B.4) such that this instability can occur. The following derivation of the conditions required for diffusion driven instability to occur is based mostly upon the approach presented in Murray (2003).

We start by determining the conditions for stability of the steady state in the absence of diffusion. Removing diffusion the system becomes, with the *'s dropped for convenience

$$\frac{\partial u}{\partial t} = \gamma f(u, v), \tag{B.5}$$

$$\frac{\partial v}{\partial t} = \gamma g(u, v). \tag{B.6}$$

The stability of the steady state $(\bar{u}, \bar{v}) = (u_0, v_0)$ can be determined by linearising about the steady state,

$$u_t = \gamma(f_u(u_0, v_0)(u - u_0) + f_v(u_0, v_0)(v - v_0)) \tag{B.7}$$

$$v_t = \gamma(g_u(u_0, v_0)(u - u_0) + g_v(u_0, v_0)(v - v_0)). \tag{B.8}$$

From here on it will be assumed that f_u, f_v, g_u, g_v are the respective functions evaluated at u_0, v_0. By setting

$$\mathbf{w} = \begin{pmatrix} u - u_0 \\ v - v_0 \end{pmatrix}, \qquad A = \begin{bmatrix} f_v & f_u \\ g_u & g_v \end{bmatrix}, \tag{B.9}$$

we can rewrite Equation (B.7) and Equation (B.8) as

$$\mathbf{w}_t = \gamma A \mathbf{w}. \tag{B.10}$$

The steady state is stable if the real part of both the eigenvalues of A are negative. For a 2×2 matrix, M, the eigenvalues, λ, are the solution to

$$\lambda^2 - \mathrm{tr}(M)\lambda + |M| = 0, \tag{B.11}$$

i.e. the eigenvalues are given by

$$\lambda = \frac{\mathrm{tr}(M) \pm \sqrt{\mathrm{tr}(M)^2 + 4|M|}}{2}. \tag{B.12}$$

From this we see that for $\mathrm{Re}\{\lambda\} < 0$, we must have $\mathrm{tr}(M) < 0$ and $|M| > 0$. Thus for our steady state $(\bar{u}, \bar{v}) = (u_0, v_0)$ we are guaranteed stability if

$$tr(\gamma A) = \gamma(f_u + g_v) < 0 \quad \Rightarrow \quad f_u + g_v < 0 \tag{B.13}$$

$$|\gamma A| = \gamma^2(f_u g_v - f_v g_u) > 0 \quad \Rightarrow \quad f_u g_v - f_v g_u > 0. \tag{B.14}$$

These are the first two conditions that must be satisfied for diffusion driven instability to occur.

We now consider the full reaction diffusion system given by equations (B.3) and (B.4). Linearising about the steady state gives

$$\mathbf{w}_t = \gamma A \mathbf{w} + D\nabla^2 \mathbf{w} \tag{B.15}$$

where

$$D = \begin{bmatrix} 1 & 0 \\ 0 & d \end{bmatrix}. \tag{B.16}$$

This is a partial differential equation (PDE) which can be solved using separation of variables. We set

$$\mathbf{w}(\mathbf{x}, t) = \mathbf{W}(\mathbf{x})T(t), \tag{B.17}$$

and by following the standard process we obtain

$$\nabla^2 \mathbf{W} = -k^2 \mathbf{W}, \tag{B.18}$$

where k is an eigenvalue of the PDE, also referred to as the wavenumber.

From separation of variables we also expect that our time solution will take the form

$$T(t) = ce^{\lambda t}. \tag{B.19}$$

Since the problem is linear we expect a superposition of solutions such that our final solution has the form

$$\mathbf{w} = \sum_k c_k e^{\lambda t} \mathbf{W}_k(\mathbf{x}), \tag{B.20}$$

where c_k are coefficients which can be determined from a Fourier expansion of the initial conditions.

We can substitute Equation (B.18) and Equation (B.20) into Equation (B.15). Our system, for each k, is now

$$\lambda c_k e^{\lambda t} \mathbf{W}_k(\mathbf{x}) = \gamma c_k e^{\lambda t} A \mathbf{W}_k(\mathbf{x}) - k^2 c_k e^{\lambda t} D \mathbf{W}_k(\mathbf{x}), \tag{B.21}$$

which can be rearranged as

$$c_k e^{\lambda t} \mathbf{W}_k (\lambda I - \gamma A + D k^2)(\mathbf{x}) = 0. \tag{B.22}$$

For a matrix equation $B\mathbf{x} = \mathbf{0}$ a non-trivial solution for $\mathbf{x}$ only exists if $|B| = 0$. This means that

$$|\lambda I - \gamma A + D k^2| = 0. \tag{B.23}$$

This is equivalent to finding the eigenvalues λ of the matrix

$$M = \gamma A - D k^2 \tag{B.24}$$

$$= \begin{bmatrix} \gamma f_u - k^2 & \gamma f_v \\ \gamma g_u & \gamma g_v - d k^2 \end{bmatrix}. \tag{B.25}$$

These eigenvalues determine the stability of the steady state. For diffusion driven instability to occur the steady state must now be unstable. For the steady state to be unstable the real part of at least one eigenvalue must be positive. From Equation (B.12) we see that this will occur if $\mathrm{tr}(M) > 0$ or $|M| < 0$.

The $\mathrm{tr}(M)$ is given by

$$\mathrm{tr}(M) = \gamma(f_u + g_v) - (1 + d)k^2. \tag{B.26}$$

From the condition given in Equation (B.13) we know that $f_u + g_v < 0$, and also by definition $d > 0$ and $\gamma > 0$. From this we see that $\mathrm{tr}(M) < 0$ and that for a diffusion driven instability to occur $|M| < 0$. The $|M|$ is given by

$$|M| = \gamma^2(f_u g_v - f_v g_u) - k^2 \gamma (d f_u + g_v) + d k^4. \tag{B.27}$$

Since $f_u g_v - f_v g_u > 0$ from the condition in Equation (B.14) it must be that

$$df_u + g_v > 0, \tag{B.28}$$

in order to have $|M| < 0$. However $f_u + g_v < 0$, so $d \neq 1$ is required. Equation (B.28) is the third condition for diffusion driven instability. It is necessary but not sufficient for $|M| < 0$.

To get the final condition we consider that Equation (B.27) is a quadratic in terms of k^2. For $|M| < 0$ for some values of k^2, it follows that the minimum value of $|M|$ must be negative. $|M|_{\min}$ occurs at

$$k^2 = \frac{\gamma d f_u + g_v}{2d} \tag{B.29}$$

and is given by

$$|M|_{\min} = -\frac{\gamma^2 (df_u + g_v)^2}{4d} + \gamma^2 (f_u g_v - f_v g_u). \tag{B.30}$$

By solving for $|M|_{\min} < 0$, we get the final condition

$$(df_u + g_v)^2 > 4d(f_u g_v - f_v g_u). \tag{B.31}$$

For given reaction kinetics there exists a critical value of the diffusion ratio $d = d_c$ for instability to occur. The critical value occurs when $|M|_{\min} = 0$. Remembering that the equations were set up such that $d > 1$, d_c is found as the appropriate root of

$$f_u^2 d_c^2 - 2(f_u g_v - 2 f_v g_u) d_c + g_v^2 = 0 \tag{B.32}$$

Given this, a critical wavenumber, k_c^2 can also be found as

$$k_c^2 = \frac{\gamma (d_c f_u + g_v)}{2 d_c} \tag{B.33}$$

Figures (B.2a) and (B.2b) show $|M|$ and $\mathrm{Re}\{\lambda\}$, respectively, as functions of k^2 for different d. As can be seen when $d < d_c$ there are no values of k^2 for which $|M| < 0$ and equivalently $\mathrm{Re}\{\lambda\} > 0$ and so no diffusion driven instability will occur. When $d > d_c$ there is a range of k^2 values that give $|M| < 0$ and $\mathrm{Re}\{\lambda\} > 0$. In this case the value of k^2 that corresponds to the maximum value of $\mathrm{Re}\{\lambda\}$ will be the dominant wavenumber in the final pattern.

The four conditions for diffusion driven instability to occur are given by Equations (B.13), (B.14), (B.28) and (B.31) and are summarised in Table B.1.

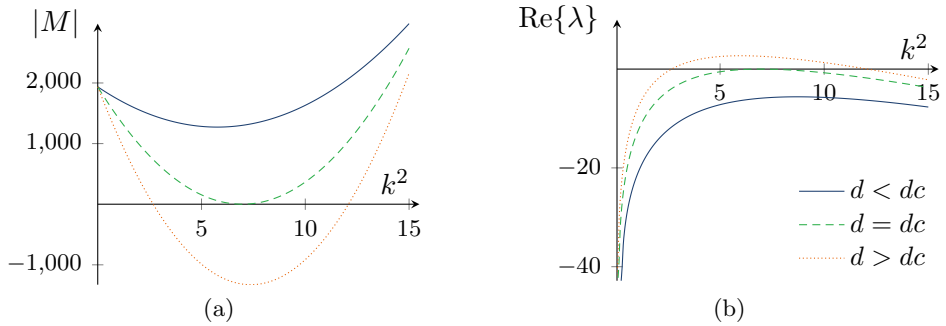

Figure B.2: Effect of diffusion coefficient on $|M|$ and $\mathrm{Re}\{\lambda\}$ for Schnackenberg kinetics with a=0.2, b=2.

Conditions for Diffusion Driven Instability
$f_u + g_v < 0$
$f_u g_v - f_v g_u > 0$
$df_u + g_v > 0$
$(df_u + g_v)^2 > 4d(f_u g_v - f_v g_u)$

Table B.1: Conditions for diffusion driven instability.

B.3.1 Physical solutions

The above conditions must be satisfied for diffusion driven instability to occur on an infinite domain. To ensure that the patterns are biologically realistic it must be that neither u nor v become negative or grow infinitly large. This introduces an extra constraint that is often overlooked. The kinetics must have a confined set in the positive quadrant

A confined set (also known as a bounded domain) exists if a closed curve can be found in the (u, v) domain where all phase trajectories on the curve point into the enclosed domain. This means that once a trajectory enters the domain it cannot leave the domain, since if the trajectory were ever to reach the boundary, it would move back into the domain. For a confined set to exist, we must have that for all points on the boundary

$$\mathbf{n}.\left(\frac{\mathrm{d}u}{\mathrm{d}t}, \frac{\mathrm{d}v}{\mathrm{d}t}\right) \leq 0, \tag{B.34}$$

where $\mathbf{n}$ is the outward pointing normal to the boundary. It can be shown that a confined set for the non-diffusive kinetics is also a confined set when diffusion is included (Smoller 1994). The important implication of this is that if a

confined set in the positive quadrant exists, then the solution obtained when diffusion is included will have finite amplitude and solutions will never become negative. If no such confined set exists then the solutions obtained with the inclusion of diffusion will tend toward infinity and/or become negative, which would both result in unrealistic solutions.

B.4 Finite Domains

A further consideration in a biological context is that we are restricted to a finite domain and both domain size and boundary conditions effect the appearance of the final pattern. For example for a given domain size it may not be possible for any of the patterns associated unstable wavenumbers to fit, and hence no pattern will be observable. We demonstrate this by considering a 1D domain of length 1 unit, with the parameters set such that unstable wavenumbers are associated with patterns with wavelengths between 8–10 units. Because the domain is much shorter then the wavelength of the possible patterns we do not expect to observe any patterns across the domain. This behaviour is also influenced by the boundary conditions.

Another example of this demonstrates the importance of the boundary conditions. Consider the case of of a 1D domain $0 \leq x \leq p$, with zero flux boundary conditions. These boundary conditions imply that the slope of the curve will be zero at the endpoint so the domain and hence that concentrations will be at either the maximum or minimum value. This means that for a pattern to fit it must be that the domain length is an integer multiple of half its wavelength. The following provides a mathematical derivation of this.

If we consider the spatial eigenvalue problem in Equation (B.18) with our imposed zero flux boundary conditions we get the following system of ODEs,

$$\frac{\mathrm{d}^2\mathbf{W}}{\mathrm{d}x^2} + k^2\mathbf{W} = 0, \qquad \left.\frac{\mathrm{d}\mathbf{W}}{\mathrm{d}x}\right|_{x=0} = \left.\frac{\mathrm{d}\mathbf{W}}{\mathrm{d}x}\right|_{x=p} = 0.c \tag{B.35}$$

Solving this gives

$$\mathbf{W}_n = \mathbf{A}_n \cos(kx), \qquad n = 0, 1, 2, ... \tag{B.36}$$

where

$$k = \frac{n\pi}{p}. \tag{B.37}$$

For each k the resultant pattern will have a wavelength of

$$l = \frac{2\pi}{k} = \frac{2p}{n}, \tag{B.38}$$

that is domain length p is an integer multiple of half the wavelength l, as described above.

Equation (B.37) gives the allowable values of k for this domain. For a diffusion driven instability to occur it must be that not only the conditions given in Table B.1 are satisfied but that the eigenvalue λ associated with at least 1 admissible wave number k as given by Equation (B.37) has $\mathrm{Re}\{\lambda\} > 0$.

It is possible that their exists multiple values of k which satisfy $\mathrm{Re}\{\lambda\} > 0$. Remembering that the linear solution is given by

$$\mathbf{w} = \sum_k c_k e^{\lambda t} \cos(kx), \tag{B.39}$$

we see that the solution is a superposition of all unstable modes. We would expect that the dominant mode of our solution would be that corresponding to the largest value of λ. This is because this mode would be the fastest growing mode when the system is perturbed from the steady state.

In reality this is only true for patterns with a low dominant mode. For larger modes the nonlinearities present in the equations have an increased effect and the expected dominant mode from the linear analysis may not be the dominant mode present in the ultimate pattern (Murray 2003).

Thus the appearance of Turing patterns is shaped by both the parameters of the model and the domain conditions. The parameters must satisfy the conditions given in Table B.1. In addition to this the domain size and boundary conditions need to be appropriate given the choice of parameters to allow patterning to be observed.

C

Numerical Methods

C.1 Introduction

Throughout this thesis a variety of numerical methods have been used to solve the PDEs and ODEs that formed our model equations. These methods were implemented in MATLAB (Release 2012b), a software package/high level coding language that is designed for solving complex mathematical problems. As part of this it contains a suite of highly efficient and optimised ODE solvers. Because of this, as much as possible we utilised the tools and functions already available within MATLAB (Release 2012b). One of the potential disadvantages with MATLAB (Release 2012b) is that because it is an interpreted language the runtimes in MATLAB (Release 2012b) will always be slower than for a similar script in a complied language such as C++. This can cause problems for large complex systems which end up with huge runtimes. However in the simulations we conducted we did not encounter any excessively long runtimes.

MATLAB (Release 2012b) has functions available to solve both systems of ODEs (the `ode` family of functions) and parabolic and elliptic PDEs with one spatial dimension (`pdepe`) and we used these to solve our model equations as appropriate. However MATLAB (Release 2012b) does not have the functionality to solve PDEs with more then one spatial dimension. Instead, for our simulations of a two dimensional domain we used a methods of lines approach. This meant that we first performed a spatial discretisation of our domain using the finite volume method. This gives a system of ODEs which we could then be solved using a suitable ODE solver in MATLAB (Release 2012b).

As we moved to more complex problems with growing and shrinking domains the above approach needed to be adapted. Two methods were explored to

handle these changing domains. Firstly we followed the approach in Illingworth & Golosnoy (2005) and rescaled to a fixed domain, and then rewrote the equations in such a way to give new conservative PDEs which we could then solve using the previously described approach. The second approach implemented but ultimately not used in any of the simulations presented in this thesis was the level set method.

C.2 Finite Volume Method

The finite volume method (FVM), also known as the control volume method is a numerical method used to discretise PDEs. It is popular in the fields of computational fluid dynamics, numerical heat transfer and transport in porous medium. An important reason for this popularity is that the FVM results in a conservative discretisation of the PDE, this allows the solution to retain the conservation present in the original equation.

We present here a basic introduction to the finite volume method. Initially we focus on a 1D discretisation discuss and demonstrate the process. We then take the 1D discretisation and use this as a basis to extend to a 2D discretisation. For a more detailed derivation of the finite volume method the reader is directed towards the many texts that can be found on the subject including Patankar (1980) and Versteeg (1995).

C.2.1 Mesh Grids

The domain on which we wish to solve our PDE is divided up using a mesh structure. The mesh is constructed from a series of nodes, which are connected to form elements. Node points can be regularly or irregularly spaced. In two dimensions elements are rectangles for a regular grid of nodes or typically triangles or quadrilaterals for an irregular grid. In three dimensions elements are typically tetrahedrons or hexahedrons.

The mesh is used to construct control volumes. This can be done using either a cell-centred or vertex-centred approach. In the cell-centred approach the control volumes are the elements and the discrete values of the solution are stored at the centroid of the cell. In a vertex-centred approach the solutions are stored at the nodes and the control volume is constructed to surround the node.

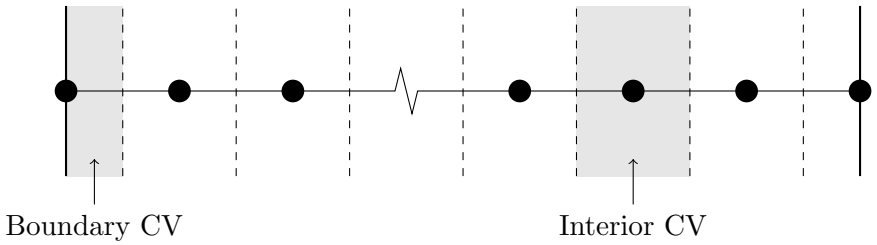

Figure C.1: Diagram of node distribution for a 1D problem, nodes are indicated by black dots and cell faces as dashed lines. We note that in this image the nodes are all separated by the same distance, this type of mesh is often referred to as a uniformly spaced mesh. A useful feature of the finite volume method is that it is not a requirement that the mesh be uniformly spaced. Instead the mesh can be designed to suit the particular problem and domain.

C.2.2 Discretisation in 1D

We start by illustrating the discretisation for a vertex centred finite volume discretisation in 1D. This discretisation is valid for a generalised advection diffusion equation

$$\frac{\partial \phi}{\partial t} + \frac{\partial}{\partial x}\left(v_x \phi - D_{xx}\frac{\partial \phi}{\partial x}\right) = S. \tag{C.1}$$

Here v_x is the advection velocity and D_{xx} is the diffusion coefficient, these coefficients are not necessarily constant and instead could depend on ϕ, x or t. The term S is the source term, a function of ϕ, x and t. This equation is often written as

$$\frac{\partial \phi}{\partial t} + \frac{\partial}{\partial x}(J) = S, \tag{C.2}$$

where

$$J = v_x \phi - D_{xx}\frac{\partial \phi}{\partial x}, \tag{C.3}$$

and is the flux due to both advection and diffusion. The boundary conditions are given by

$$v_x \phi - D_{xx}\frac{\partial \phi}{\partial x} = k(\phi_\infty - \phi) \qquad \text{at } x = 0, \tag{C.4}$$

$$v_x \phi - D_{xx}\frac{\partial \phi}{\partial x} = -k(\phi_\infty - \phi) \qquad \text{at } x = L. \tag{C.5}$$

We note that in the limit $k \to \infty$ the generalised boundary conditions become Dirichlet conditions. The initial condition is

$$\phi(0, x) = \phi_0(x). \tag{C.6}$$

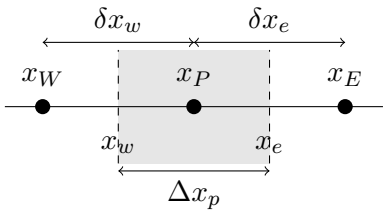

Figure C.2: Diagram of an interior node, demonstrating the notations used in this section. The following conventions are used, capital subscripts refer to values at the node points, for example P refers to the current point, and E and W refer to the points to the east and west respectively. Lower case subscripts refer to values at the faces, again the subscripts e and w referring to the east and west face, relative to the current node. When describing the spatial properties of the grid an upper-case Δx refers to a individual cells width, whereas a lower-case δx refers to the distance between cells, again the subscripts e and w to denote between the east and west.

A regularly spaced vertex centred mesh is illustrated in Figure C.1. An individual interior node is illustrated in Figure C.2. This figure also provides an illustration of the notation used in the following discretisation.

In the following we are only deriving a spatial discretisation. The temporal integration can then be completed numerically by a variety of methods including the use of the many widely available numerical integrators available (such as `ode45` or any of the other ODE solvers available with MATLAB (Release 2012b), or the sundials package).

Taking Equation (C.2) and integrating over the control volume we get

$$\int_{x_w}^{x_e} \frac{\partial \phi}{\partial t} \,\mathrm{d}x + \int_{x_w}^{x_e} \frac{\partial}{\partial x}(J) \,\mathrm{d}x = \int_{x_w}^{x_e} S \,\mathrm{d}x. \tag{C.7}$$

We introduce control volume averages

$$\bar{\phi}_P = \frac{1}{\Delta x_P} \int_{x_w}^{x_e} \phi \,\mathrm{d}x, \tag{C.8}$$

and

$$\bar{S}_P = \frac{1}{\Delta x_P} \int_{x_w}^{x_e} S \,\mathrm{d}x, \tag{C.9}$$

to get

$$\frac{\partial \bar{\phi}_P}{\partial t} + \frac{1}{\Delta x_P}(J_e - J_w) = \bar{S}_P. \tag{C.10}$$

Here J_e and J_w is the flux evaluated at the east and west face respectively. We can approximate the control volume averages as the value at the node P

and write

$$\frac{\partial \phi_P}{\partial t} + \frac{1}{\Delta x_P}(J_e - J_w) \approx S_P. \tag{C.11}$$

We note that for a uniformly spaced grid this approximation will be second order accurate. All that is left now is to approximate the flux at the faces, J_e and J_w.

C.2.3 Treatement of the Diffusion Term

In the case where $v_x = 0$ then there is no advection and flow is purely diffusive. The expression for the east flux becomes,

$$J_e = \left(-D_{xx}\frac{\partial \phi}{\partial x}\right)_e, \tag{C.12}$$

$$= -D_{xx_e}\left(\frac{\partial \phi}{\partial x}\right)_e. \tag{C.13}$$

Here D_{xx_e} is the diffusion coefficient evaluated at the east face. In the case of a non-constant diffusion coefficient care must be taken in the approximation of D_{xx_e}, however this level of detail is beyond the level required in this thesis. The remaining term $\left(\frac{\partial \phi}{\partial x}\right)_e$ is the x derivative of ϕ evaluated at the east face. A natural approximation of this derivative is to use

$$\left(\frac{\partial \phi}{\partial x}\right)_e \approx \frac{\phi_E - \phi_P}{\delta x_e}. \tag{C.14}$$

This gives the east flux as

$$J_e \approx -D_{xx_e}\frac{\phi_E - \phi_P}{\delta x_e}, \tag{C.15}$$

and simiarly we find the west flux as

$$J_w \approx -D_{xx_w}\frac{\phi_P - \phi_W}{\delta x_w}. \tag{C.16}$$

These flux approximations are second order accurate for a uniformly spaced grid.

C.2.4 Treatment of the Advection Term

We now present a method for the discretisation of the advection term. There are many methods that can be used to implement this discretisation, including averaging and up-winding. Averaging and up-winding are simple to implement

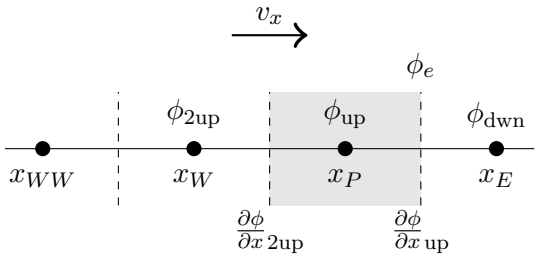

Figure C.3: Illustration of the labels used in the description fo flux limiting to find the value of ϕ_e, for an advection from left to right.

but have drawbacks. Instead, in this thesis we use an approach known as flux limiting, and use the van Leer limiter. This method is both second order accurate in space and will not give spurious oscillations in the solution (van Leer 1974, Sweby 1984).

With advection the flux on the east face is

$$J_e = v_{x_e}\phi_e - D_{xx_e}\left(\frac{\partial\phi}{\partial x}\right)_e. \tag{C.17}$$

The diffusion component of this equation can be approximated in the same fashion as before. We assume that the velocity at the face, v_{x_e}, can be found exactly. However we need a way to approximate ϕ_e, that is the value of ϕ at the east face.

When using flux limiting to approximate ϕ_e we introduce a limiter function $\sigma(r)$ where r is a sensor to be defined. The value of ϕ_e at the face is then given as

$$\phi_e \approx \phi_{\text{up}} + \frac{\sigma}{2}(\phi_{\text{dwn}} - \phi_{\text{up}}), \tag{C.18}$$

where ϕ_{up} is the upstream value of ϕ and ϕ_{dwn} is the downstream value as illustrated in Figure C.3. When the velocity is positive, the advective flow is from left to right. In this case to find ϕ_e, the downwind value is ϕ_E and the upwind value is ϕ_P. If the velocity was negative (flow from right to left) these would be reversed. We note that through our choice of σ we can achieve averaging ($\sigma = 1$), up-winding ($\sigma = 0$) or down-winding ($\sigma = 2$). For van Leer flux limiting σ is given by

$$\sigma(r) = \frac{r + |r|}{1 + |r|}. \tag{C.19}$$

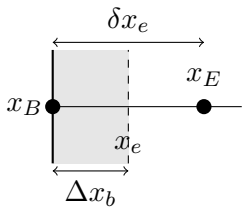

Figure C.4: Diagram illustrating the notation used for boundary nodes. The diagram shows the boundary at $x = 0$ and we note the introduction of the subscript B to illustrate the boundary nodes.

To evaluate σ we use a sensor r defined as

$$r = \frac{\left(\frac{\partial \phi}{\partial x}\right)_{\text{2up}}}{\left(\frac{\partial \phi}{\partial x}\right)_{\text{up}}} \tag{C.20}$$

where the subscript $2up$ indicates the value at the second upwind face and the subscript up indicates the value at the upwind face.

C.2.5 Boundary Nodes

For the boundary nodes a similar process is followed to obtain the discretisation. The boundary at $x = 0$ is illustrated in Figure C.4. We note the introduction of the subscript b to indicate the boundary node, face and control volume. Integrating across the control volume and introducing the control volume averages $\bar{\phi}$ and $\bar{S}$ gives

$$\frac{\partial \bar{\phi}_P}{\partial t} + \frac{1}{\Delta x_b}(J_e - J_b) = \bar{S}_P. \tag{C.21}$$

We approximate the cell averages as the value at the boundary and yhe east flux can be approximated using the methods described above. This leaves only the flux at the boundary, J_b to be found. Equation (C.4) explicitly states the flux and hence can simply be substituted into this equation. Thus for the boundary cell at $x = 0$ we can write

$$\frac{\partial \phi_B}{\partial t} \approx \frac{1}{\Delta x_b}(J_e - k(\phi_\infty - \phi_B)) + S_B. \tag{C.22}$$

Using the same process a similar expression can be formulated for the boundary at $x = L$.

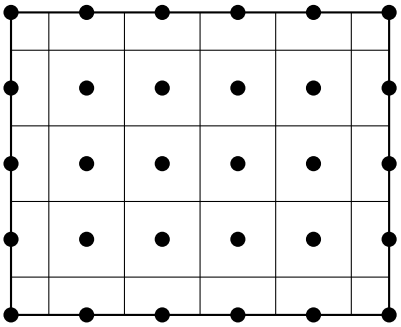

Figure C.5: Schematic of a rectangular grip over a 2D domain. The circles are nodes and the solid lines the cell faces.

C.3 Finite Volume Method in Two Dimensions

In the following section we extend the discretisation presented above to a 2D mesh. Whilst it is possible to use a irregular mesh, in this section we focus purely on a discretisation on a regular mesh grid, such as that illustrated in Figure C.5, as this was the scheme used throughout the thesis. In 2D the generalised equation to be discretised is

$$\frac{\partial \phi}{\partial t} + \nabla \cdot (-\mathbf{D}\nabla\phi + \mathbf{v}\phi) = S, \tag{C.23}$$

where $\mathbf{D}$ is the diffusion tensor and $\mathbf{v}$ is the advection velocity. As in the one dimensional case we can introduce an expression for the flux

$$\mathbf{J} = -\mathbf{D}\nabla\phi + \mathbf{v}\phi. \tag{C.24}$$

We consider generic boundary conditions

$$-\mathbf{D}\nabla\phi + \mathbf{v}\phi = k(\phi_\infty - \phi), \quad \text{on } x \in \partial\Omega \tag{C.25}$$

and initial condition

$$\phi(x, y, 0) = \phi_0(x, y). \tag{C.26}$$

In Figure C.6 we illustrate a typical interior control volume and its neighbours. If we integrate over the control volume we get

$$\int_{\Omega_P} \frac{\partial \phi}{\partial t} \,\mathrm{d}V + \int_{\Omega_P} \nabla \cdot \mathbf{J} \,\mathrm{d}V = \int_{\Omega_P} S \,\mathrm{d}V. \tag{C.27}$$

We introduce the control volume averages

$$\bar{\phi}_P = \frac{1}{V_P} \int_{\Omega_P} \phi \,\mathrm{d}V, \tag{C.28}$$

$$\bar{S}_P = \frac{1}{V_P} \int_{\Omega_P} S \,\mathrm{d}V, \tag{C.29}$$

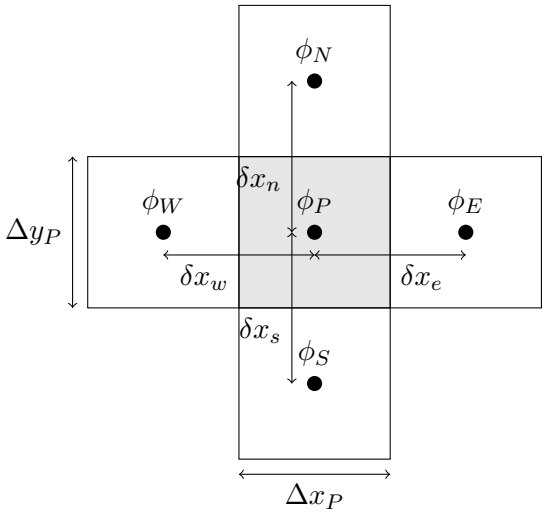

Figure C.6: Diagram of a typical control volume in 2D demonstrating the notation.

where $V_P = \Delta x_P \Delta y_P$ is the area of the control volume and use these to rewrite Equation (C.27) as

$$\frac{\partial \bar{\phi}_P}{\partial t} + \frac{1}{V_P} \int_{\Omega_P} \nabla \cdot \mathbf{J} \, \mathrm{d}V = \bar{S}_P. \tag{C.30}$$

We turn our attention now to approximating the second term in this equation. From Gausses law we can write this term as

$$\int_{\Omega_P} \nabla \cdot \mathbf{J} \, \mathrm{d}V = \int_{\partial \Omega_P} \mathbf{J} \cdot \hat{\mathbf{n}} \, \mathrm{d}S, \tag{C.31}$$

$$= \sum_{j \in n,e,s,w} \int_{\partial \Omega_{P_j}} \mathbf{J} \cdot \hat{\mathbf{n}} \, \mathrm{d}S_j. \tag{C.32}$$

for a rectangular cell such as that in Figure C.6. If we consider for example the east face. Here the normal is defined as $\hat{\mathbf{n}} = \mathbf{i}$. Thus we introduce the notation $J_e = \mathbf{J} \cdot \hat{\mathbf{n}}$ as representing the horizontal component of the flux evaluated at the east face. The total flux lost through the east face is

$$\int_{\partial \Omega_{P_e}} J_e \, \mathrm{d}S_e = \bar{J}_e \Delta y_p, \tag{C.33}$$

where $\bar{J}_e$ is the average value of J_e along the face. We use a midpoint approximation for this average value and take $\bar{J}_e$ as the value of the flux at the midpoint of the face $(x, y) = (x_e, y_p)$. Furthermore we need to approximate the value of the flux at this point. In the case of pure diffusion we can use the

same approximation as the one dimensional case and get

$$\int_{\partial\Omega_{P_e}} J_e \,\mathrm{d}S_e \approx D_{xx}\frac{\phi_E - \phi_P}{\delta_e}\Delta y_p. \tag{C.34}$$

Using the same arguments for the north, south and west faces we can write the following approximation

$$\int_{\Omega_P} \nabla \cdot \mathbf{J} \,\mathrm{d}V \approx (J_e - J_w)\Delta y_p + (J_n - J_s)\Delta x_p \tag{C.35}$$

$$\begin{aligned} &\approx D_{xx}\left(\frac{\phi_E - \phi_P}{\delta x_e} - \frac{\phi_P - \phi_W}{\delta x_w}\right)\Delta y_p \\ &\quad + D_{yy}\left(\frac{\phi_N - \phi_P}{\delta y_n} - \frac{\phi_P - \phi_S}{\delta y_s}\right)\Delta x_p \end{aligned} \tag{C.36}$$

With the inclusion of advection terms the approximation of the flux becomes more difficult. The use of averaging is the simplest of the methods. Upwinding and flux limiting can be used however their use introduces additional complexities, particularly when the velocity field is complex. For example, consider a velocity field that curves by 90° from heading north to heading east. If we consider a node point just after the bend, is the upwind point to the west of the node or to the south?

For the purposes of these thesis we do not encounter these problems. In all of our simulations with advection the velocity vector $\mathbf{v} = [V_x, 0]$ only has a horizontal component. Thus we can safely use flux-limiting to approximate the flux due to advection in the horizontal direction.

The treatment of the boundaries done in a manner similar to the 1D case. Again we note that the boundary condition Equation (C.25) explicitly states the flux at the boundary. We can simply substitute this boundary flux for the relevant term in Equation (C.35).

C.4 Simulations on a Growing or Shrinking Domain: A Rescaling Approach

In some of the models we consider there is a need to be able to numerically solve a moving boundary problem, with both growing and shrinking domains. One approach that can be used to solve these moving boundary problems is to rescale the problem to static domain. In order to use the FVM on this

rescaled problem we need to convert it to conservative form. To do this we use follow the approach in (Illingworth & Golosnoy 2005). In this section we consider a 2D domain that is static in the y direction but the boundaries in the x direction are moving. We enforce no specific directionality on the movement of these boundaries, rather there direction will be determined by the velocity function. This formulation can be reuduced to either of the moving boundary problems in Chapters 4 and 5. Throughout the domain we solve the generic PDE

$$\frac{\partial \phi}{\partial t} = D\nabla^2\phi + S, \tag{C.37}$$

where D is the diffusion constant and S is the source function, possible dependent on ϕ, x, y or t. We note that there is no advection considered in this initial PDE as there was no advection in any of our models. At this stage we do not define any boundary conditions but will discuss the effect of the rescaling on the boundary conditions as used in our models later on. We will however define the velocity of the moving boundaries as

$$\frac{\mathrm{d}L_1}{\mathrm{d}t} = v_1, \tag{C.38}$$

$$\frac{\mathrm{d}L_2}{\mathrm{d}t} = v_2, \tag{C.39}$$

where v_1 and v_2 are functions that describe the velocity of the boundary. By convention if the velocity is positive the boundary moves to the right and if it is negative it moves to the left. Finally we define the initial condition as

$$\phi(x, y, 0) = \phi_0. \tag{C.40}$$

Since the domain is only changing in the x direction this is the only direction in which we need to apply the scaling. We introduce a new spatial variable, $\zeta \in [0, 1]$, and rescale x as

$$\zeta(t) = \frac{x - L_1(t)}{L_2(t) - L_1(t)}. \tag{C.41}$$

Applying this scaling to Equation (C.37) gives

$$\frac{\partial \phi}{\partial t} + \frac{\partial \zeta}{\partial t}\frac{\partial \phi}{\partial \zeta} = D\left(\frac{\partial \zeta}{\partial x}\right)^2 \frac{\partial^2 \phi}{\partial \zeta^2} + D\frac{\partial^2 \phi}{\partial y^2} + S, \tag{C.42}$$

Evaluating the partial derivatives of ζ and introducing the notation L_1' and L_2' to represent the temporal derivatives of L_1 and L_2 we get

$$\frac{\partial \phi}{\partial t} + \frac{(\zeta - 1)L_1' - \zeta L_2'}{L_2 - L_1}\frac{\partial \phi}{\partial \zeta} = \left(\frac{D}{L_2 - L_1}\right)^2 \frac{\partial^2 \phi}{\partial \zeta^2} + D\frac{\partial^2 \phi}{\partial y^2} + S. \tag{C.43}$$

This can be rewritten in conservative form as

$$\frac{\partial \mu}{\partial t} = \frac{\partial}{\partial \zeta}\left(\frac{D}{(L_2 - L_1)^2}\frac{\partial \mu}{\partial \zeta} + \frac{\zeta L_2' + (1-\zeta)L_1'}{L_2 - L_1}\mu\right) + D\frac{\partial^2 \mu}{\partial y^2} + (L_2 - L_1)S, \tag{C.44}$$

where $\mu = (L_2 - L_1)\phi$. This equation is conservative for the quantity $\mu = (L_2 - L_1)\phi$, we could write it in the form given in Equation (C.23) and hence easily solve this PDE numerically using the FVM. We notice that whilst our original equation had no advection terms the moving boundaries have introduced advection in the x direction. As this artificial velocity is purely in the x direction and hence we can easily use flux-limiting as our scheme to calculate the advection fluxes without any of the complexities that can arise for more complicated velocity fields.

Of course we also have to apply the transform in Equation (C.41) to our boundary and initial conditions and ensure that they are written in terms of $\mu = (L_2 - L_1)\phi$. Applying these to the initial condition yeilds

$$(L_2 - L_1)\phi|_{t=0} = (L_2(0) - L_1(0))\phi_0. \tag{C.45}$$

In addition to the discretised equations from the FVM we also need to solve Equations (C.38) and (C.39) to track the position of our boundaries. Because of the presence of the L_1' and L_2' in Equation (C.44) to solve these equations in MATLAB (Release 2012b) we need to use the function `ode15i`.

C.4.1 Transformation As Applied To The Model For Cellular Differentiation

We conclude this appendix by providing details of the specific equations that were used to solve the PDE systems giving throughout this thesis. In Chapter 4 we considered a 2D domain where the domain was fixed in the y direction but the right most boundary in the x direction was growing. We see that this is a simplification of our general case where $L_1 = 0$ and $L_1' = 0$. Additionally in this model the right most boundary is denoted as $L_2 = L_x$. The equations

to be solved are

$$\frac{\partial \bar{P}}{\partial \bar{t}} = \bar{P}\big(1-\bar{P}-\bar{O}\big) - \frac{\bar{B}\bar{P}}{\bar{\epsilon}+\bar{N}} + \nabla^2 \bar{P}, \tag{C.46}$$

$$\frac{\partial \bar{O}}{\partial \bar{t}} = -\bar{\delta}\bar{O} + \frac{\bar{B}\bar{P}}{\bar{\epsilon}+\bar{N}} + \bar{D}_O \nabla^2 \bar{O}, \tag{C.47}$$

$$\frac{\partial \bar{B}}{\partial \bar{t}} = \bar{\alpha}\bar{P} + \bar{\beta}\frac{\bar{B}^2\bar{O}}{\bar{\sigma}+\bar{N}} - \bar{\rho}\bar{B} + \bar{D}_B \nabla^2 \bar{B}, \tag{C.48}$$

$$\frac{\partial \bar{N}}{\partial \bar{t}} = \bar{\eta}\bar{B}^2\bar{O} - \bar{\mu}\bar{N} + \bar{D}_N \nabla^2 \bar{N}. \tag{C.49}$$

with

$$\frac{\mathrm{d}\bar{L}_x}{\mathrm{d}\bar{t}} = \bar{\rho}. \tag{C.50}$$

The boundary conditions on $\bar{x} = 0$ are

$$\begin{aligned} \frac{\partial \bar{P}}{\partial \bar{x}} &= 0, & \frac{\partial \bar{O}}{\partial \bar{x}} &= 0, \\ \bar{B} &= 5, & \frac{\partial \bar{N}}{\partial \bar{x}} &= 0, \end{aligned} \tag{C.51}$$

and on $\bar{x} = \bar{L}_x$

$$\begin{aligned} \bar{P} &= 0.8, & \bar{O} &= 0, \\ \frac{\partial \bar{B}}{\partial \bar{x}} &= -\frac{\bar{\rho}}{\bar{D}_B}\bar{B}, & \frac{\partial \bar{N}}{\partial \bar{x}} &= -\frac{\bar{\rho}}{\bar{D}_N}\bar{N}. \end{aligned} \tag{C.52}$$

On the top and bottom boundaries, zero flux boundary conditions are applied for all species. The initial conditions are

$$\begin{aligned} \bar{P} &= 0.8, & \bar{O} &= 0, \\ \bar{B} &= 2.77, & \bar{N} &= 0.077. \end{aligned} \tag{C.53}$$

We can apply the above rescaling and transformation in a straight forward manner to Equations C.46–C.49,

$$\begin{aligned} \frac{\partial \bar{L}_x \bar{P}}{\partial \bar{t}} = \bar{L}_x &\left(\bar{P}\big(1-\bar{P}-\bar{O}\big) - \frac{\bar{B}\bar{P}}{\bar{\epsilon}+\bar{N}} \right) + \frac{\partial}{\partial \zeta}\left(\frac{\bar{D}_P}{\bar{L}_x^2}\frac{\partial \bar{L}_x \bar{P}}{\partial \zeta} + \frac{\zeta L_x'}{L_x}\bar{L}_x\bar{P} \right) \\ &+ \bar{D}_P \frac{\partial^2 \bar{L}_x \bar{P}}{\partial \bar{y}^2}, \end{aligned} \tag{C.54}$$

$$\begin{aligned} \frac{\partial \bar{L}_x \bar{O}}{\partial \bar{t}} = \bar{L}_x &\left(-\bar{\delta}\bar{O} + \frac{\bar{B}\bar{P}}{\bar{\epsilon}+\bar{N}} \right) + \frac{\partial}{\partial \zeta}\left(\frac{\bar{D}_O}{\bar{L}_x^2}\frac{\partial \bar{L}_x \bar{O}}{\partial \zeta} + \frac{\zeta L_x'}{L_x}\bar{L}_x\bar{O} \right) \\ &+ \bar{D}_O \frac{\partial^2 \bar{L}_x \bar{O}}{\partial \bar{y}^2}, \end{aligned} \tag{C.55}$$

$$\frac{\partial \bar{L}_x \bar{B}}{\partial \bar{t}} = \bar{L}_x\left(\bar{\alpha}\bar{P} + \bar{\beta}\frac{\bar{B}^2\bar{O}}{\bar{\sigma}+\bar{N}} - \bar{\rho}\bar{B}\right) + \frac{\partial}{\partial\zeta}\left(\frac{\bar{D}_B}{\bar{L}_x^2}\frac{\partial \bar{L}_x\bar{B}}{\partial\zeta} + \frac{\zeta L_x'}{L_x}\bar{L}_x\bar{B}\right) + \bar{D}_B\frac{\partial^2 \bar{L}_x\bar{B}}{\partial\bar{y}^2}, \tag{C.56}$$

$$\frac{\partial \bar{L}_x \bar{N}}{\partial \bar{t}} = \bar{L}_x\left(\bar{\eta}\bar{B}^2\bar{O} - \bar{\mu}\bar{N}\right) + \frac{\partial}{\partial\zeta}\left(\frac{\bar{D}_N}{\bar{L}_x^2}\frac{\partial \bar{L}_x\bar{N}}{\partial\zeta} + \frac{\zeta L_x'}{L_x}\bar{L}_x\bar{N}\right) + \bar{D}_N\frac{\partial^2 \bar{L}_x\bar{N}}{\partial\bar{y}^2}, \tag{C.57}$$

(C.58)

The boundary conditions on $\bar{y} = 0$ and $\bar{y} = \bar{L}_y$ remain unchanged by the transformation. The left boundary $\bar{x} = 0$ is transformed to $\zeta = 0$. We see that for $\zeta = 0$ the advection term in the flux disappears and it becomes a simple task to transform the boundary conditions. On the right boundary $\bar{x} = \bar{L}_x$ transforms to $\zeta = 1$. Here the Dirichlet boundary conditions for $\bar{P}$ and $\bar{O}$ remain unchanged. However for the chemical species the boundary conditions are zero flux and we demonstrate that this is the case once the transformation has been applied. Applying the transformation to the boundary condition for $\bar{B}$ gives

$$\frac{\partial \bar{B}}{\partial\zeta} = -\frac{\bar{L}_x\bar{\rho}}{\bar{D}_B}\bar{B}, \tag{C.59}$$

and we see that substituting this into the expression for the horizontal flux of $\bar{B}$ gives

$$\frac{\bar{D}_B}{\bar{L}_x^2}\frac{\partial \bar{L}_x\bar{B}}{\partial\zeta} + \frac{\zeta L_x'}{L_x}\bar{L}_x\bar{B} = 0. \tag{C.60}$$

Simiarly for $\bar{N}$

$$\frac{\bar{D}_N}{\bar{L}_x^2}\frac{\partial \bar{L}_x\bar{N}}{\partial\zeta} + \frac{\zeta L_x'}{L_x}\bar{L}_x\bar{N} = 0. \tag{C.61}$$

Finally the initial conditions can be simply scaled by the initial domain length as in Equation (C.45).

C.4.2 Transformation As Applied To The Model For Mineral Deposition

Finally we turn our attention to the model presented in Chapter 5. In this model we consider a 1D domain but both the boundaries are able to move. Again this is a simplified case of the general case given above where we can simply omit the y dimension. The non-dimensional model equations are given

by

$$\frac{\partial \bar{A}}{\partial \bar{t}} = \bar{D}_A \frac{\partial^2 \bar{A}}{\partial \bar{x}^2} + \bar{\alpha} + \bar{\beta}\bar{A}\bar{P} - \bar{\delta}\bar{A}, \tag{C.62}$$

$$\frac{\partial \bar{P}}{\partial \bar{t}} = \bar{D}_P \frac{\partial^2 \bar{P}}{\partial \bar{x}^2} + \bar{\eta} - \frac{\bar{k}_{\text{cat}}\bar{A}\bar{P}}{\bar{K}_M\left(1 + \frac{\bar{I}}{\bar{K}_I}\right)}, \tag{C.63}$$

$$\frac{\partial \bar{I}}{\partial \bar{t}} = \bar{D}_I \frac{\partial^2 \bar{I}}{\partial \bar{x}^2} + 2 \times 10^{-3} \frac{\bar{k}_{\text{cat}}\bar{A}\bar{P}}{\bar{K}_M\left(1 + \frac{\bar{I}}{\bar{K}_I}\right)}, \tag{C.64}$$

$$\frac{\mathrm{d}\bar{L}_1}{\mathrm{d}\bar{t}} = \frac{\bar{\lambda}}{2}\left(1 + \tanh\left(\bar{\mu}\left(\bar{\gamma} - \frac{\bar{P}(\bar{L}_1, \bar{t})}{\bar{I}(\bar{L}_1, \bar{t})}\right)\right)\right). \tag{C.65}$$

$$\tag{C.66}$$

With boundary conditions on $\bar{x} = \bar{L}_1$

$$\frac{\partial \bar{A}}{\partial \bar{x}} = 0, \tag{C.67}$$

$$\frac{\partial \bar{P}}{\partial \bar{x}} = 0, \tag{C.68}$$

$$\frac{\partial \bar{I}}{\partial \bar{x}} = \frac{\bar{I} - \bar{I}_M}{\bar{D}_I}\frac{\mathrm{d}\bar{L}_1}{\mathrm{d}\bar{t}}, \tag{C.69}$$

and on $\bar{x} = \bar{L}_2$,

$$\frac{\partial \bar{A}}{\partial \bar{x}} = 0, \tag{C.70}$$

$$\frac{\partial \bar{P}}{\partial \bar{x}} = -\bar{\sigma}(\bar{P} - \bar{P}_0), \tag{C.71}$$

$$\bar{I} = \bar{I}_0. \tag{C.72}$$

The initial conditions are given as

$$\bar{A}(\bar{x}, 0) = \bar{A}_0, \quad \bar{P}(\bar{x}, 0) = \bar{P}_0, \quad \bar{I}(\bar{x}, 0) = \bar{I}_0, \quad \bar{L}_1(0) = \bar{L}_{1_0} \tag{C.73}$$

We apply the transformation to get

$$\begin{aligned}\frac{\partial(\bar{L}_2 - \bar{L}_1)\bar{A}}{\partial \bar{t}} &= (\bar{L}_2 - \bar{L}_1)\big(\bar{\alpha} + \bar{\beta}\bar{A}\bar{P} - \bar{\delta}\bar{A}\big) \\ &\quad + \frac{\partial}{\partial \zeta}\left(\frac{\bar{D}_A}{(\bar{L}_2 - \bar{L}_1)^2}\frac{\partial(\bar{L}_2 - \bar{L}_1)\bar{A}}{\partial \zeta} + \frac{\bar{L}_1'(1-\zeta)}{(\bar{L}_2 - \bar{L}_1)}(\bar{L}_2 - \bar{L}_1)\bar{A}\right),\end{aligned} \tag{C.74}$$

$$\frac{\partial(\bar{L}_2-\bar{L}_1)\bar{P}}{\partial\bar{t}} = (\bar{L}_2-\bar{L}_1)\left(\bar{\eta}-\frac{\bar{k}_{\text{cat}}\bar{A}\bar{P}}{\bar{K}_M\left(1+\frac{\bar{I}}{\bar{K}_I}\right)}\right) + \frac{\partial}{\partial\zeta}\left(\frac{\bar{D}_P}{(\bar{L}_2-\bar{L}_1)^2}\frac{\partial(\bar{L}_2-\bar{L}_1)\bar{P}}{\partial\zeta}+\frac{\bar{L}_1'(1-\zeta)}{(\bar{L}_2-\bar{L}_1)}(\bar{L}_2-\bar{L}_1)\bar{P}\right), \tag{C.75}$$

$$\frac{\partial(\bar{L}_2-\bar{L}_1)\bar{I}}{\partial\bar{t}} = (\bar{L}_2-\bar{L}_1)\left(2\times10^{-3}\frac{\bar{k}_{\text{cat}}\bar{A}\bar{P}}{\bar{K}_M\left(1+\frac{\bar{I}}{\bar{K}_I}\right)}\right) + \frac{\partial}{\partial\zeta}\left(\frac{\bar{D}_I}{(\bar{L}_2-\bar{L}_1)^2}\frac{\partial(\bar{L}_2-\bar{L}_1)\bar{I}}{\partial\zeta}+\frac{\bar{L}_1'(1-\zeta)}{(\bar{L}_2-\bar{L}_1)}(\bar{L}_2-\bar{L}_1)\bar{I}\right), \tag{C.76}$$

$$\frac{\mathrm{d}\bar{L}_1}{\mathrm{d}\bar{t}} = \frac{\bar{\lambda}}{2}\left(1+\tanh\left(\bar{\mu}\left(\bar{\gamma}-\frac{\bar{P}(\bar{L}_1,\bar{t})}{\bar{I}(\bar{L}_1,\bar{t})}\right)\right)\right). \tag{C.77}$$

The boundary $\bar{x}=\bar{L}_1$ becomes $\zeta=0$ in the rescaled dimensions. On this boundary the equations for $\bar{A}$ and $\bar{P}$ are such that the only material lost through the boundary is due to the movement of the boundary. As the boundary moves from left to right the domain shrinks and a region that was once part of the domain is lost. Additionally any TNAP or $\mathrm{PP_i}$ in this region is also lost. In the unscaled version of this problem, the boundary condition appeared to be a zero flux condition, however we see that once the rescaling has been applied this is not the case. For TNAP and $\mathrm{PP_i}$ the boundary conditions on $\zeta=0$ becomes

$$\frac{\bar{D}_A}{(\bar{L}_2-\bar{L}_1)^2}\frac{\partial(\bar{L}_2-\bar{L}_1)\bar{A}}{\partial\zeta}+\frac{\bar{L}_1'}{(\bar{L}_2-\bar{L}_1)}(\bar{L}_2-\bar{L}_1)\bar{A}=\bar{L}_1'\bar{A} \tag{C.78}$$

$$\frac{\bar{D}_P}{(\bar{L}_2-\bar{L}_1)^2}\frac{\partial(\bar{L}_2-\bar{L}_1)\bar{P}}{\partial\zeta}+\frac{\bar{L}_1'}{(\bar{L}_2-\bar{L}_1)}(\bar{L}_2-\bar{L}_1)\bar{P}=\bar{L}_1'\bar{P} \tag{C.79}$$

$$\tag{C.80}$$

For $\mathrm{P_i}$ on this boundary we had a condition derived from a conservation of mass argument. Rescaling this equation gives

$$\frac{\bar{D}_I}{(\bar{L}_2-\bar{L}_1)^2}\frac{\partial(\bar{L}_2-\bar{L}_1)\bar{I}}{\partial\zeta}+\frac{\bar{L}_1'(1-\zeta)}{(\bar{L}_2-\bar{L}_1)}(\bar{L}_2-\bar{L}_1)\bar{I}=\bar{I}_M\bar{L}_1', \tag{C.81}$$

we see that the amount of $\mathrm{P_i}$ lost through the boundary is simply the density of the new bone mineral times the speed at which the mineralisation is occurring.

On the right boundary the coordinate transformation converts $\bar{x}=\bar{L}_1$ into $\zeta=1$. The advective component of the flux disappears at this boundary and

the boundary conditions can be simply rewritten as

$$\frac{\partial(\bar{L}_2 - \bar{L}_1)\bar{A}}{\partial\zeta} = 0, \tag{C.82}$$

$$\frac{\partial(\bar{L}_2 - \bar{L}_1)\bar{P}}{\partial\zeta} = \bar{\sigma}(\bar{L}_2 - \bar{L}_1)^2(\bar{P} - \bar{P}_0), \tag{C.83}$$

$$(\bar{L}_2 - \bar{L}_1)\bar{I} = (\bar{L}_2 - \bar{L}_1)\bar{I}_0. \tag{C.84}$$

As before it is a simple task to rescale the initial conditions by the initial domain length as in Equation (C.45).

Glossary

ALP Alkaline phosphatase. An enzyme that breaks down phosphate compounds

BMP Bone morphogenetic protein. The BMP family of proteins are growth factors that induce the formation of bone and cartilage. BMP 2 and 4 have both been associated with intramembranous bone growth.

Cancellous Bone Bone that has a spongy appearance. In long bones it is found in the ends of the bone. The plate and rod-like structures that give its appearance are called trabecula.

Chondrocyte Cartilage cell

Cortical Bone Dense bone tissue that forms the shaft of long bones. The cortical bone is constructed from well organised layers of bone, known as lamella.

Hydroxyapatite Mineral component of bone, $Ca_{10}(PO_4)_6(OH)_2$.

MAR Mineral apposition rate. Measured quantity that describes the rate at which new mineral is being formed.

MSC Mesenchymal stem cell. Pluripotent stem cell with the capacity to become osteoblasts. During fracture healing these cells accumulate at the fracture site and differentiate to drive new tissue formation.

Noggin BMP inhibitor associated with reduced intramembranous bone formation.

Osteoblast Bone forming cells. These cells are responsible for creating new bone tissue.

Osteoblast Progenitor Partially differentiated cell on the pathway to become an osteoblast. We use this term throughout the thesis to refer to cells present in the periosteum.

Osteocyte Cells embedding in the bone tissue. Thought to play a role in sensing damage and regulating remodelling.

Osteoid Unmineralised bone matrix.

Periosteum Membrane like material that surrounds bones. In fracture healing is a source of progenitor cells.

P_i Inorganic phosphate. Free phosphate found in the extracellular fluid.

PP_i Pyrophosphate. Potent inhibitor of mineral formation.

TNAP Tissue non-specific alkaline phosphatase. The specific form of ALP produced by osteoblasts. Believed to be important for the removal of PP_i.

Bibliography

Abe, E., Yamamoto, M., Taguchi, Y., Lecka-Czernik, B., O'Brien, C. A., Economides, A. N., Stahl, N., Jilka, R. L. & Manolagas, S. C. (2000), 'Essential requirement of bmps-2/4 for both osteoblast and osteoclast formation in murine bone marrow cultures from adult mice: Antagonism by noggin', *Journal of Bone and Mineral Research* **15**(4), 663–673.

Addison, W., Azari, F., Sørensen, E., Kaartinen, M. & McKee, M. (2007), 'Pyrophosphate inhibits mineralization of osteoblast cultures by binding to mineral, up-regulating osteopontin, and inhibiting alkaline phosphatase activity', *Journal of Biological Chemistry* **282**(21), 15872–15883.

Ament, C. & Hofer, E. P. (2000), 'A fuzzy logic model of fracture healing', *Journal of Biomechanics* **33**(8), 961–968.

Antonova, E., Le, T. K., Burge, R. & Mershon, J. (2013), 'Tibia shaft fractures: costly burden of nonunions', *BMC Musculoskeletal Disorders* **14**(1), 42.

Arnett, T. (2008), 'Osteocytes - human bone', *European Calcified Tissue Society*. Available from: http://www.ectsoc.org/gallery/#myGallery-picture(6),[cited 2013 Dec 28].

Ashby, M., Gibson, L., Wegst, U. & Olive, R. (1995), 'The mechanical properties of natural materials. i. material property charts', *Proceedings of the Royal Society of London. Series A: Mathematical and Physical Sciences* **450**(1938), 123–140.

Aspenberg, P., Jeppsson, C. & Econmides, A. N. (2001), 'The bone morphogenetic proteins antagonist noggin inhibits membranous ossification', *Journal of Bone and Mineral Research* **16**(3), 497–500. PMID: 11277267.

Aspinall, V., O'Reilly, M. & Capello, M. (2004), *Introduction to veterinary anatomy and physiology*, illustrated edn, Elsevier Health Sciences.

Augat, P., Simon, U., Liedert, A. & Claes, L. (2005), 'Mechanics and mechano-biology of fracture healing in normal and osteoporotic bone', *Osteoporosis International* **16**, 36–43.

Bailón-Plaza, A. & van der Meulen, M. C. (2001), 'A mathematical framework to study the effects of growth factor influences on fracture healing', *Journal of Theoretical Biology* **212**(2), 191–209.

Bailón-Plaza, A. & van der Meulen, M. C. (2003), 'Beneficial effects of moderate, early loading and adverse effects of delayed or excessive loading on bone healing', *Journal of Biomechanics* **36**(8), 1069–1077.

Balemans, W. & Hul, W. V. (2002), 'Extracellular regulation of BMP signaling in vertebrates: A cocktail of modulators', *Developmental Biology* **250**(2), 231–250.

Barnes, G., Kostenuik, P., Gerstenfeld, L. C. & Einhorn, T. A. (1999), 'Growth factor regulation of fracture repair', *Journal of Bone and Mineral Research* **14**, 1805–1810.

Birch, M. A. & Wright, K. E. (2013), *Standardisation in Cell and Tissue Engineering: Methods and Protocols*, Elsevier Science, chapter Two- and three-dimensional tissue culture methods for hard tissue engineering, pp. 54 – 76.

Boccaccio, A., Ballini, A., Pappalettere, C., Tullo, D., Cantore, S. & Desiate, A. (2011), 'Finite element method (fem), mechanobiology and biomimetic scaffolds in bone tissue engineering', *International journal of biological sciences* **7**(1), 112.

Boron, W. & Boulpaep, E. (2003), *Medical Physiology: A Cellular and Molecular Approach*, W.B. Saunders.

Bose, S., Roy, M. & Bandyopadhyay, A. (2012), 'Recent advances in bone tissue engineering scaffolds', *Trends in Biotechnology* **30**(10), 546–554.

Boskey, A. (2001), *Bone Mechanics Handbook*, 2nd edn, CRC Press, chapter Bone Mineralization, pp. 5.1–5.33.

Boskey, A. L. & Robey, P. G. (2013), *Primer on the Metabolic Bone Diseases and Disorders of Mineral Metabolism*, 8th edn, Wiley-Blackwell, chapter The composition of bone, pp. 49–58.

Bostrom, M. P. (1998), 'Transforming growth factor beta in fracture repair', *Clinical Orthopaedics and Related Research* **355**, S124–S131.

Buenzli, P. R., Pivonka, P. & Smith, D. W. (2011), 'Spatio-temporal structure of cell distribution in cortical bone multicellular units: a mathematical model', *Bone* **48**(4), 918–926.

Buenzli, P. R., Pivonka, P. & Smith, D. W. (2014), 'Bone refilling in cortical basic multicellular units: insights into tetracycline double labelling from a computational model', *Biomechanics and Modeling in Mechanobiology* **13**(1), 185–203.

Carlier, A., Chai, Y. C., Moesen, M., Theys, T., Schrooten, J., Van Oosterwyck, H. & Geris, L. (2011), 'Designing optimal calcium phosphate scaffold–cell combinations using an integrative model-based approach', *Acta Biomaterialia* **7**(10), 3573–3585.

Carter, D. R., Blenman, P. R. & Beaupré, G. S. (1988), 'Correlations between mechanical stress history and tissue differentiation in initial fracture healing', *Journal of Orthopaedic Research* **6**, 736–748.

Chang, P.-L., Blair, H. C., Zhao, X., Chien, Y.-w., Chen, D., Tilden, A. B., Chang, Z., Cao, X., Faye-Petersen, O. M. & Hicks, P. (2006), 'Comparison of fetal and adult marrow stromal cells in osteogenesis with and without glucocorticoids', *Connective Tissue Research* **47**(2), 67–76.

Chen, D., Harris, M., Rossini, G., Dunstan, C., Dallas, S., Feng, J., Mundy, G. & Harris, S. (1997), 'Bone morphogenetic protein 2 (BMP-2) enhances BMP-3, BMP-4, and bone cell differentiation marker gene expression during the induction of mineralized bone matrix formation in culturesof fetal rat calvarial osteoblasts', *Calcified Tissue International* **60**(3), 283–290.

Chen, D., Zhao, M. & Mundy, G. (2004), 'Bone morphogenetic proteins', *Growth Factors* **22**(4), 233–241.

Cheng, H., Jiang, W., Phillips, F. M., Haydon, R. C., Peng, Y., Zhou, L., Luu, H. H., An, N., Breyer, B., Vanichakarn, P., Szatkowski, J. P., Park, J. Y. & He, T.-C. (2003), 'Osteogenic Activity of the Fourteen Types of Human Bone Morphogenetic Proteins (BMPs)', *The Journal of Bone and Joint Surgery* **85**(8), 1544–1552.

Cho, T., Gerstenfeld, L. & Einhorn, T. (2002), 'Differential temporal expression of members of the transforming growth factor β superfamily during murine fracture healing', *Journal of Bone and Mineral Research* **17**(3), 513–520.

Choi, J.-Y., Lee, B.-H., Song, K.-B., Park, R.-W., Kim, I.-S., Sohn, K.-Y., Jo, J.-S. & Ryoo, H.-M. (1996), 'Expression patterns of bone-related proteins during osteoblastic differentiation in MC3T3-E1 cells', *Journal of Cellular Biochemistry* **61**(4), 609–618.

Ciancaglini, P., Yadav, M., Simão, A., Narisawa, S., Pizauro, J., Farquharson, C., Hoylaerts, M. & Millán, J. (2010), 'Kinetic analysis of substrate utilization by native and TNAP-, NPP1-, or PHOSPHO1-deficient matrix vesicles', *Journal of Bone and Mineral Research* **25**(4), 716–723.

Claes, L. & Heigele, C. (1999), 'Magnitudes of local stress and strain along bony surfaces predict the course and type of fracture healing', *Journal of Biomechanics* **32**(3), 255 – 266.

Clarke, B. (2008), 'Normal bone anatomy and physiology', *Clinical Journal of the American Society of Nephrology* **3**(Supplement 3), S131–S139.

Courtin, B., Perault, A. & Staub, J. (1997), 'A reaction-diffusion model for trabecular architecture of embryonic periosteal long bone', *Complexity International* **4**, 1–17.

Courtin, B., Perault-Staub, A. & Staub, J. (1995), 'Spatio-temporal self organization of bone mineral metabolism and trabecular structure of primary bone', *Acta Biotheoretica* **43**, 373–386.

Cowles, E., DeRome, M., Pastizzo, G., Brailey, L. & Gronowicz, G. (1998), 'Mineralization and the expression of matrix proteins during in vivo bone development', *Calcified Tissue International* **62**(1), 74–82.

Crampin, E., Hackborn, W. & Maini, P. (2002), 'Pattern formation in reaction-diffusion models with nonuniform domain growth', *Bulletin of Mathematical Biology* **64**(4), 747–769.

Currey, J. (2002), *Bones: Structure and Mechanics*, Princeton University Press.

Cyboron, G. W., Vejins, M. S. & Wuthier, R. E. (1982), 'Activity of epiphyseal cartilage membrane alkaline phosphatase and the effects of its inhibitors at physiological pH.', *Journal of Biological Chemistry* **257**(8), 4141 – 4146.

Davies, J. E. (2003), 'Understanding peri-implant endosseous healing', *Journal of Dental Education* **67**(8), 932–949.

Delhanty, P. J. D., van der Eerden, B. C. J., van der Velde, M., Gauna, C., Pols, H. A. P., Jahr, H., Chiba, H., van der Lely, A. J. & van Leeuwen, J. P. T. M. (2006), 'Ghrelin and unacylated ghrelin stimulate human osteoblast growth via mitogen-activated protein kinase (MAPK)/phosphoinositide 3-kinase (PI3K) pathways in the absence of GHS-R1a', *Journal of Endocrinology* **188**(1), 37–47.

Dimitriou, R., Tsiridis, E., Carr, I., Simpson, H. & Giannoudis, P. V. (2006), 'The role of inhibitory molecules in fracture healing', *Injury* **37**(1, Supplement 1), S20–S29.

Doblaré, M., García, J. M. & Gómez, M. J. (2004), 'Modelling bone tissue fracture and healing: a review', *Engineering Fracture Mechanics* **71**(13-14), 1809 – 1840.

Donnelly, E., Chen, D. X., Boskey, A. L., Baker, S. P. & van der Meulen, M. C. (2010), 'Contribution of mineral to bone structural behavior and tissue mechanical properties', *Calcified Tissue International* **87**(5), 450–460.

Economou, A. D., Ohazama, A., Porntaveetus, T., Sharpe, P. T., Kondo, S., Basson, M. A., Gritli-Linde, A., Cobourne, M. T. & Green, J. B. (2012), 'Periodic stripe formation by a turing mechanism operating at growth zones in the mammalian palate', *Nature Genetics* **44**(3), 348–351.

Einhorn, T. A. (1998), 'The cell and molecular biology of fracture healing', *Clinical Orthopaedics and Related Research* **355**, s7–s21.

Epari, D. R., Schell, H., Bail, H. J. & Duda, G. N. (2006), 'Instability prolongs the chondral phase during bone healing in sheep', *Bone* **38**(6), 864–870.

Epari, D., Wehner, T., Ignatius, A., Schuetz, M. & Claes, L. (2013), 'A case for optimising fracture healing through inverse dynamization', *Medical hypotheses* **81**(2), 225–227.

Fernley, H. N. & Walker, P. G. (1967), 'Studies on alkaline phosphatase. inhibition by phosphate derivatives and the substrate specificity', *The Biochemical Journal* **104**(3), 1011–1018.

Fleisch, H. & Bisaz, S. (1962), 'Isolation from urine of pyrophosphate, a calcification inhibitor', *American Journal of Physiology* **203**(4), 671–675.

Flury, M. & Gimmi, T. F. (2002), *Methods of soil analysis: Physical methods*, Soil Science Society of America, chapter Solute diffusion, pp. 1323–1351.

Franz-Odendaal, T. A., Hall, B. K. & Witten, P. E. (2006), 'Buried alive: how osteoblasts become osteocytes', *Developmental Dynamics* **235**(1), 176–190.

Fratzl, P., Gupta, H. S., Paschalis, E. P. & Roschger, P. (2004), 'Structure and mechanical quality of the collagen-mineral nano-composite in bone', *Journal of Materials Chemistry* **14**, 2115–2123.

Gardner, T. N., Stoll, T., Marks, L., Mishra, S. & Tate, M. K. (2000), 'The influence of mechanical stimulus on the pattern of tissue differentiation in a long bone fracture – an FEM study', *Journal of Biomechanics* **33**(4), 415–425.

Garzón-Alvarado, D. (2013), 'A hypothesis on the formation of the primary ossification centers in the membranous neurocranium: A mathematical and computational model', *Journal of Theoretical Biology* **317**, 366–376.

Garzón-Alvarado, D., García-Aznar, J. & Doblaré, M. (2009*a*), 'A reaction–diffusion model for long bones growth', *Biomechanics and modeling in mechanobiology* **8**(5), 381–395.

Garzón-Alvarado, D., García-Aznar, J. & Doblaré, M. (2009*b*), 'Appearance and location of secondary ossification centres may be explained by a reaction-diffusion mechanism', *Computers in Biology and Medicine* **39**(6), 554–561.

Gazzerro, E., Gangji, V. & Canalis, E. (1998), 'Bone morphogenetic proteins induce the expression of noggin, which limits their activity in cultured rat osteoblasts.', *Journal of Clinical Investigation* **102**, 2106–2114.

Geris, L., Gerisch, A., Maes, C., Carmeliet, G., Weiner, R., Sloten, J. V. & Oosterwyck, H. V. (2006), 'Mathematical modeling of fracture healing in mice: comparison between experimental data and numerical simulation results', *Medical and Biological Engineering and Computing* **44**, 280–289.

Geris, L., Gerisch, A., Sloten, J., Weiner, R. & Oosterwyck, H. (2008), 'Angiogenesis in bone fracture healing: a bioregulatory model', *Journal of Theoretical Biology* **251**(1), 137–158.

Geris, L., Schugart, R. & Van Oosterwyck, H. (2010), 'In silico design of treatment strategies in wound healing and bone fracture healing', *Philosophical Transactions of the Royal Society A: Mathematical, Physical and Engineering Sciences* **368**(1920), 2683–2706.

Geris, L., Vander Sloten, J. & Van Oosterwyck, H. (2009), 'In silico biology of bone modelling and remodelling: regeneration', *Philosophical Transactions of the Royal Society A: Mathematical, Physical and Engineering Sciences* **367**(1895), 2031–2053.

Gerstenfeld, L. C., Cullinane, D. M., Barnes, G. L., Graves, D. T. & Einhorn, T. A. (2003), 'Fracture healing as a post-natal developmental process: Molecular, spatial, and temporal aspects of its regulation', *Journal of Cellular Biochemistry* **88**, 873–884.

Gierer, A. & Meinhardt, H. (1972), 'A theory of biological pattern formation', *Biological Cybernetics* **12**, 30–39.

Glaser, D. L., Economides, A. N., Wang, L., Liu, X., Kimble, R. D., Fandl, J. P., Wilson, J. M., Stahl, N., Kaplan, F. S. & Shore, E. M. (2003), 'In vivo somatic cell gene transfer of an engineered noggin mutein prevents

BMP4-induced heterotopic ossification', *The Journal of Bone and Joint Surgery* **85**(12), 2332–2342.

Glowacki, J. (1998), 'Angiogenesis in fracture repair', *Clinical Orthopaedics and Related Research* **355**, S82–S89.

Golub, E. E. (2009), 'Role of matrix vesicles in biomineralization', *Biochimica et Biophysica Acta (BBA)-General Subjects* **1790**(12), 1592–1598.

Golub, E. E. (2010), 'Biomineralization and matrix vesicles in biology and pathology', *Seminars in Immunopathology* **33**(5), 409–417.

Gómez-Benito, M., García-Aznar, J., Kuiper, J. & Doblaré, M. (2005), 'Influence of fracture gap size on the pattern of long bone healing: a computational study', *Journal of Theoretical Biology* **235**(1), 105 – 119.

Gosling, J., Harris, P., Humpherson, J., Whitmore, I. & Willan, P. (2008), *Human Anatomy, Color Atlas and Textbook*, Elsevier Health Sciences UK.

Gupta, S. (2003), *The Classical Stefan Problem: basic concepts, modelling and analysis*, North-Holland Series in Applied Mathematics and Mechanics, Elsevier Science.

Harmey, D., Hessle, L., Narisawa, S., Johnson, K. A., Terkeltaub, R. & Millán, J. L. (2004), 'Concerted regulation of inorganic pyrophosphate and osteopontin by akp2, enpp1, and ank: An integrated model of the pathogenesis of mineralization disorders', *The American Journal of Patholagy* **164**(4), 1199–1209.

Hessle, L., Johnson, K. A., Anderson, H. C., Narisawa, S., Sali, A., Goding, J. W., Terkeltaub, R. & Millán, J. L. (2002), 'Tissue-nonspecific alkaline phosphatase and plasma cell membrane glycoprotein-1 are central antagonistic regulators of bone mineralization', *Proceedings of the National Academy of Sciences* **99**(14), 9445–9449.

Hirakawa, K., Hirota, S., Ikeda, T., Yamaguchi, A., Takemura, T., Nagoshi, J., Yoshiki, S., Suda, T., Kitamura, Y. & Nomura, S. (1994), 'Localization of the mRNA for bone matrix proteins during fracture healing as determined by in situ hybridization', *Journal of Bone and Mineral Research* **9**(10), 1551–1557.

Holtz, K. M. & Kantrowitz, E. R. (1999), 'The mechanism of the alkaline phosphatase reaction: insights from nmr, crystallography and site-specific mutagenesis', *FEBS Letters* **462**(1-2), 7–11.

Hsu, D., Economides, A., Wang, X., Eimon, P. & Harland, R. (1998), 'The xenopus dorsalizing factor gremlin identifies a novel family of secreted proteins that antagonize BMP Activities', *Molecular cell* **1**(5), 673–683.

Huang, X., Wang, Y. & Su, H. (2007), 'Limit cycles in morphogenesis', *Nonlinear Analysis: Real World Applications* **8**(4), 1341 – 1348.

Illingworth, T. & Golosnoy, I. (2005), 'Numerical solutions of diffusion-controlled moving boundary problems which conserve solute', *Journal of Computational Physics* **209**(1), 207–225.

Isaksson, H. (2012), 'Recent advances in mechanobiological modeling of bone regeneration', *Mechanics Research Communications* **42**, 22–31.

Isaksson, H., van Donkelaar, C. C., Huiskes, R. & Ito, K. (2008), 'A mechano-regulatory bone-healing model incorporating cell-phenotype specific activity', *Journal of theoretical biology* **252**(2), 230–246.

Jee, W. S. (2001), *Bone Mechanics Handbook*, CRC Press, chapter Integrated Bone Tissue Physiology:Anatomy and Physiology, pp. 1–1 – 1–68.

Jilka, R. L., Weinstein, R. S., Bellido, T., Parfitt, A. M. & Manolagas, S. C. (1998), 'Osteoblast programmed cell death (apoptosis): modulation by growth factors and cytokines', *Journal of Bone and Mineral Research* **13**(5), 793–802.

Jilka, R. L., Weinstein, R. S., Parfitt, A. M. & Manolagas, S. C. (2007), 'Perspective: Quantifying osteoblast and osteocyte apoptosis: challenges and rewards', *Journal of Bone and Mineral Research* **22**(10), 1492–1501.

Johnson, K., Goding, J., Van Etten, D., Sali, A., Hu, S.-I., Farley, D., Krug, H., Hessle, L., Millán, J. L. & Terkeltaub, R. (2003), 'Linked deficiencies in extracellular ppi and osteopontin mediate pathologic calcification associated with defective PC-1 and ANK expression', *Journal of Bone and Mineral Research* **18**(6), 994–1004.

Jones, C., Armes, N. & Smith, J. (1996), 'Signalling by TGF-β family members: short-range effects of Xnr-2 and BMP-4 contrast with the long-range effects of activin', *Current Biology* **6**(11), 1468–1475.

Jones, C. & Smith, J. (1998), 'Establishment of a BMP-4 morphogen gradient by long-range inhibition', *Developmental Biology* **194**(1), 12–17.

Jubiz, W., Canterbury, J. M., Reiss, E. & Tyler, F. H. (1972), 'Circadian rhythm in serum parathyroid hormone concentration in human subjects: correlation with serum calcium, phosphate, albumin, and growth hormone levels', *The Journal of Clinical Investigation* **51**(8), 2040–2046.

Jung, H.-S., Francis-West, P. H., Widelitz, R. B., Jiang, T.-X., Ting-Berreth, S., Tickle, C., Wolpert, L. & Chuong, C.-M. (1998), 'Local inhibitory action of BMPs and their relationships with activators in feather formation: implications for periodic patterning', *Developmental Biology* **196**(1), 11–23.

Kanakaris, N. & Giannoudis, P. V. (2007), 'The health economics of the treatment of long-bone non-unions', *Injury* **38**, S77–S84.

Kirsch, T. (2006), 'Determinants of pathological mineralization', *Current Opinion in Rheumatology* **18**(2), 174–180.

Kirsch, T., Harrison, G., Golub, E. E. & Nah, H. (2000), 'The roles of annexins and types II and X collagen in matrix vesicle-mediated mineralization of growth plate cartilage', *Journal of Biological Chemistry* **275**(45), 35577–35583.

Kirsch, T., Nickel, J. & Sebald, W. (2000), 'BMP-2 antagonists emerge from alterations in the low-affinity binding epitope for receptor BMPR-II', *The EMBO Journal* **19**, 3314–3324.

Koch, A. J. & Meinhardt, H. (1994), 'Biological pattern formation: from basic mechanisms to complex structures', *Reviews of Modern Physics* **66**, 1481–1507.

Kondo, S. & Asai, R. (1995), 'A reaction-diffusion wave on the skin of the marine angelfish Pomacanthus', *Nature* **376**(6543), 765–768.

Korkalainen, M., Kallio, E., Olkku, A., Nelo, K., Ilvesaro, J., Tuukkanen, J., Mahonen, A. & Viluksela, M. (2009), 'Dioxins interfere with differentiation of osteoblasts and osteoclasts', *Bone* **44**(6), 1134 – 1142.

Krause, C., Guzman, A. & Knaus, P. (2011), 'Noggin', *The International Journal of Biochemistry & Cell Biology* **43**(4), 478–481.

Kristensen, L. P., Chen, L., Nielsen, M. O., Qanie, D. W., Kratchmarova, I., Kassem, M. & Andersen, J. S. (2012), 'Temporal profiling and pulsed silac labeling identify novel secreted proteins during ex vivo osteoblast differentiation of human stromal stem cells', *Molecular & Cellular Proteomics* **11**(10), 989–1007.

Lacroix, D. & Prendergast, P. J. (2002), 'A mechano-regulation model for tissue differentiation during fracture healing: analysis of gap size and loading', *Journal of Biomechanics* **35**(9), 1163 – 1171.

Lecanda, F., Avioli, L. & Cheng, S. (1998), 'Regulation of bone matrix protein expression and induction of differentiation of human osteoblasts and human bone marrow stromal cells by bone morphogenetic protein-2', *Journal of Cellular Biochemistry* **67**(3), 386–398.

Leppänen, T., Karttunen, M., Kaski, K., Barrio, R. A. & Zhang, L. (2002), 'A new dimension to turing patterns', *Physica D: Nonlinear Phenomena* **168**, 35–44.

Li, G., White, G., Connolly, C. & Marsh, D. (2002), 'Cell proliferation and apoptosis during fracture healing', *Journal of Bone and Mineral Research* **17**(5), 791–799.

Luo, G., Ducy, P., McKee, M. D., Pinero, G. J., Loyer, E., Behringer, R. R. & Karsenty, G. (1997), 'Spontaneous calcification of arteries and cartilage in mice lacking matrix GLA protein', *Nature* **386**(6620), 78–81.

Maeda, T., Matsunuma, A., Kawane, T. & Horiuchi, N. (2001), 'Simvastatin promotes osteoblast differentiation and mineralization in mc3t3-e1 cells', *Biochemical and Biophysical Research Communications* **280**(3), 874–877.

Maini, P., Benson, D. & Sherratt, J. (1992), 'Pattern formation in reaction-diffusion models with spatially inhomogeneous diffusion coefficients', *Mathematical Medicine and Biology* **9**(3), 197.

Majeska, R. J. (2001), *Bone Mechanics Handbook*, 2nd edn, CRC Press, chapter Cell Biology of Bone, pp. 2–1 – 2–24.

Manjubala, I., Liu, Y., Epari, D., Roschger, P., Schell, H., Fratzl, P. & Duda, G. (2009), 'Spatial and temporal variations of mechanical properties and mineral content of the external callus during bone healing', *Bone* **45**, 185–192.

Mann, S. (2001), *Biomineralization: Principles and Concepts in Bioinorganic Materials Chemistry*, Oxford Chemistry Masters Series, Oxford University Press.

Manolagas, S. C. (2000), 'Birth and death of bone cells: Basic regulatory mechanisms and implications for the pathogenesis and treatment of osteoporosis', *Endocrine Reviews* **21**(2), 115–137.

MATLAB (Release 2012b), The MathWorks, Inc., Natick, Massachusetts, United States.

Millán, J. (2006), *Mammalian Alkaline Phosphatases*, John Wiley & Sons, Weinheim.

Montessuit, C., Caverzasio, J. & Bonjour, J.-P. (1991), 'Characterization of a Pi transport system in cartilage matrix vesicles. Potential role in the calcification process.', *Journal of Biological Chemistry* **266**(27), 17791–17797.

Moreo, P., García-Aznar, J. M. & Doblaré, M. (2009), 'Bone ingrowth on the surface of endosseous implants. part 1: Mathematical model', *Journal of theoretical biology* **260**(1), 1–12.

Murray, J. (2003), *Mathematical Biology*, Vol. 2, 3 edn, Springer, New York.

Murshed, M., Harmey, D., Millán, J. L., McKee, M. D. & Karsenty, G. (2005), 'Unique coexpression in osteoblasts of broadly expressed genes accounts for the spatial restriction of ECM mineralization to bone', *Genes & Development* **19**(9), 1093 –1104.

Nudelman, F., Pieterse, K., George, A., Bomans, P. H., Friedrich, H., Brylka, L. J., Hilbers, P. A. & Sommerdijk, N. A. (2010), 'The role of collagen in bone apatite formation in the presence of hydroxyapatite nucleation inhibitors', *Nature Materials* **9**(12), 1004–1009.

Ohkawara, B., Iemura, S.-i., ten Dijke, P. & Ueno, N. (2002), 'Action range of BMP is defined by its N-Terminal basic amino acid core', *Current Biology* **12**(3), 205–209.

Onichtchouk, D., Chen, Y., Dosch, R., Gawantka, V., Delius, H., Massague, J. & Niehrs, C. (1999), 'Silencing of TGF-β signalling by the pseudoreceptor BAMBI', *Nature* **401**(6752), 480–485.

Onishi, T., Ishidou, Y., Nagamine, T., Yone, K., Imamura, T., Kato, M., Sampath, T., ten Dijke, P. & Sakou, T. (1998), 'Distinct and overlapping patterns of localization of bone morphogenetic protein (bmp) family members and a bmp type ii receptor during fracture healing in rats', *Bone* **22**(6), 605–612.

Orimo, H. & Shimada, T. (2006), 'Effects of phosphates on the expression of tissue-nonspecific alkaline phosphatase gene and phosphate-regulating genes in short-term cultures of human osteosarcoma cell lines', *Molecular and Cellular Biochemistry* **282**(1-2), 101–108.

Osher, S. & Sethian, J. A. (1988), 'Fronts propagating with curvature-dependent speed: algorithms based on hamilton-jacobi formulations', *Journal of Computational Physics* **79**(1), 12–49.

Page, K., Maini, P. & Monk, N. (2003), 'Pattern formation in spatially heterogeneous Turing reaction-diffusion models', *Physica D: Nonlinear Phenomena* **181**(1-2), 80–101.

Parfitt, A. M., Drezner, M. K., Glorieux, F. H., Kanis, J. A., Malluche, H., Meunier, P. J., Ott, S. M. & Recker, R. R. (1987), 'Bone histomorphometry: standardization of nomenclature, symbols, and units: report of the ASBMR Histomorphometry Nomenclature Committee', *Journal of Bone and Mineral Research* **2**(6), 595–610.

Patankar, S. (1980), *Numerical Heat Transfer and Fluid Flow*, Series in computational methods in mechanics and thermal sciences, Taylor & Francis.

Pauwels, F. (1980), *Biomechanics of the locomotor apparatus: contributions on the functional anatomy of the locomotor apparatus*, Translated by Maquet, P. G. & Furlong, R., Springer-Verlag.

Peacock, M. (2010), 'Calcium metabolism in health and disease', *Clinical Journal of the American Society of Nephrology* **5**(Supplement 1), S23–S30.

Perren, S. (1979), 'Physical and biological aspects of fracture healing with special reference to internal fixation.', *Clinical Orthopaedics & Related Research* **138**, 175–196.

Piccolo, S., Sasai, Y., Lu, B. & De Robertis, E. (1996), 'Dorsoventral patterning in xenopus: inhibition of ventral signals by direct binding of chordin to bmp-4', *Cell* **86**(4), 589–598.

Pivonka, P. & Dunstan, C. R. (2012), 'Role of mathematical modeling in bone fracture healing', *BoneKEy Reports* **1**.

Pivonka, P., Zimak, J., Smith, D. W., Gardiner, B. S., Dunstan, C. R., Sims, N. A., John Martin, T. & Mundy, G. R. (2008), 'Model structure and control of bone remodeling: a theoretical study', *Bone* **43**(2), 249–263.

Pratap, J., Galindo, M., Zaidi, S. K., Vradii, D., Bhat, B. M., Robinson, J. A., Choi, J.-Y., Komori, T., Stein, J. L., Lian, J. B. et al. (2003), 'Cell growth regulatory role of Runx2 during proliferative expansion of preosteoblasts', *Cancer Research* **63**(17), 5357–5362.

Prendergast, P. J., Huiskes, R. & Søballe, K. (1997), 'Biophysical stimuli on cells during tissue differentiation at implant interfaces', *Journal of Biomechanics* **30**(6), 539 – 548.

Prendergast, P. & van der Meulen, M. (2001), *Bone Mechanics Handbook*, 2nd edn, CRC Press, chapter Mechanics of Bone Regeneration, pp. 32–1 – 32–13.

Prokharau, P. A., Vermolen, F. J. & García-Aznar, J. M. (2012), 'Model for direct bone apposition on pre-existing surfaces, during peri-implant osseointegration', *Journal of Theoretical Biology* **304**, 131–142.

Psychogios, N., Hau, D. D., Peng, J., Guo, A. C., Mandal, R., Bouatra, S., Sinelnikov, I., Krishnamurthy, R., Eisner, R., Gautam, B., Young, N., Xia, J., Knox, C., Dong, E., Huang, P., Hollander, Z., Pedersen, T. L., Smith, S. R., Bamforth, F., Greiner, R., McManus, B., Newman, J. W., Goodfriend, T. & Wishart, D. S. (2011), 'The human serum metabolome', *PLoS ONE* **6**(2).

Rezende, A. A., Pizauro, J. M., Ciancaglini, P. & Leone, F. A. (1994), 'Phosphodiesterase activity is a novel property of alkaline phosphatase from osseous plate', *The Biochemical Journal* **301 (Pt 2)**, 517–522.

Rizzo, D. (2011), *Introduction to Anatomy and Physiology*, Delmar Cengage Learning.

Russell, R. G. G., Bisaz, S., Donath, A., Morgan, D. B. & Fleisch, H. (1971), 'Inorganic pyrophosphate in plasma in normal persons and in patients with hypophosphatasia, osteogenesis imperfecta, and other disorders of bone', *The Journal of Clinical Investigation* **50**(5), 961–969.

Rutsch, F., Ruf, N., Vaingankar, S., Toliat, M. R., Suk, A., Höhne, W., Schauer, G., Lehmann, M., Roscioli, T., Schnabel, D. et al. (2003), 'Mutations in ENPP1 are associated with 'idiopathic' infantile arterial calcification', *Nature Genetics* **34**(4), 379–381.

Ryser, M. D., Nigam, N. & Komarova, S. V. (2009), 'Mathematical modeling of spatio-temporal dynamics of a single bone multicellular unit', *Journal of Bone and Mineral Research* **24**(5), 860–870.

Sapir-Koren, R. & Livshits, G. (2011), 'Bone mineralization and regulation of phosphate homeostasis', *IBMS BoneKEy* **8**(6), 286–300.

Scanlon, V. C. & Sanders, T. (2011), *Essentials of anatomy and physiology*, F.A. Davis Co., Philadelphia, PA.

Schell, H., Lienau, J., Epari, D. R., Seebeck, P., Exner, C., Muchow, S., Bragulla, H., Haas, N. P. & Duda, G. N. (2006), 'Osteoclastic activity begins early and increases over the course of bone healing', *Bone* **38**(4), 547 – 554.

Schindeler, A., McDonald, M. M., Bokko, P. & Little, D. G. (2008), 'Bone remodeling during fracture repair: The cellular picture', *Seminars in Cell & Developmental Biology* **19**(5), 459 66.

Schnackenberg, J. (1979), 'Simple chemical reaction systems with limit cycle behaviour', *Journal of Theoretical Biology* **81**, 389–400.

Schoelles, K., Snyder, D., Kaczmarek, J., Evelyn Kuserk, M., Erinoff, E. & Turkelson, C. (2005), *The role of bone growth stimulating devices and orthobiologics in healing nonunion fractures*, Technology Assessment. Prepared by the ECRI Evidence-Based Practice Center for the Agency for Healthcare Research and Quality (AHRQ). Rockville, MD.

Segel, L. A. & Jackson, J. L. (1972), 'Dissipative structure: An explanation and an ecological example', *Journal of Theoretical Biology* **37**(3), 545 – 559.

Simão, A. M. S., Beloti, M. M., Cezarino, R. M., Rosa, A. L., Pizauro, J. M. & Ciancaglini, P. (2007), 'Membrane-bound alkaline phosphatase from ectopic mineralization and rat bone marrow cell culture', *Comparative Biochemistry and Physiology - Part A: Molecular & Integrative Physiology* **146**(4), 679–687.

Smith, W. & Harland, R. (1992), 'Expression cloning of noggin, a new dorsalizing factor localized to the spemann organizer in xenopus embryos.', *Cell* **70**(5), 829–840.

Smoller, J. (1994), *Shock waves and reaction-diffusion equations*, Springer.

Spector, J., Luchs, J., Mehrara, B., Greenwald, J., Smith, L. & Longaker, M. (2001), 'Expression of bone morphogenetic proteins during membranous bone healing', *Plastic and Reconstructive Surgery* **107**(1), 124–134.

Stanford, C. M., Jacobson, P. A., Eanes, E. D., Lembke, L. A. & Midura, R. J. (1995), 'Rapidly forming apatitic mineral in an osteoblastic cell line (Umr 10601 Bsp)', *Journal of Biological Chemistry* **270**(16), 9420–9428.

Staub, J., Tracqui, P., Brezillon, P., Milhaud, G. & Perault-Staub, A. (1988), 'Calcium metabolism in the rat: a temporal self-organized model', *American Journal of Physiology-Regulatory, Integrative and Comparative Physiology* **254**(1), R134–R149.

Stenderup, K., Justesen, J., Clausen, C. & Kassem, M. (2003), 'Aging is associated with decreased maximal life span and accelerated senescence of bone marrow stromal cells¡ sup¿,¡/sup¿', *Bone* **33**(6), 919–926.

Street, J., Bao, M., DeGuzman, L., Bunting, S., Peale, F., Ferrara, N., Steinmetz, H., Hoeffel, J., Cleland, J., Daugherty, A., van Bruggen, N., Redmond, H. P., Carano, R. A. D. & Filvaroff, E. H. (2002), 'Vascular endothelial growth factor stimulates bone repair by promoting angiogenesis and bone turnover', *Proceedings of the National Academy of Sciences of the United States of America* **99**(15), 9656–9661.

Suk, E.-K., Malkin, I., Dahm, S., Kalichman, L., Ruf, N., Kobyliansky, E., Toliat, M., Rutsch, F., Nürnberg, P. & Livshits, G. (2005), 'Association of ENPP1 gene polymorphisms with hand osteoarthritis in a Chuvasha population', *Arthritis Research and Therapy* **7**(5), R1082–R1090.

Sweby, P. K. (1984), 'High resolution schemes using flux limiters for hyperbolic conservation laws', *SIAM Journal on Numerical Analysis* **21**(5), 995–1011.

Terkeltaub, R. A. (2001), 'Inorganic pyrophosphate generation and disposition in pathophysiology', *American Journal of Physiology-Cell Physiology* **281**(1), C1–C11.

Thompson, Z., Miclau, T., Hu, D. & Helms, J. (2002), 'A model for intramembranous ossification during fracture healing', *Journal of Orthopaedic Research* **20**(5), 1091–1098.

Tosounidis, T., Kontakis, G., Nikolaou, V., Papathanassopoulos, A. & Giannoudis, P. (2009), 'Fracture healing and bone repair: an update', *Trauma* **11**(3), 145–156.

Tsiridis, E., Upadhyay, N. & Giannoudis, P. (2007), 'Molecular aspects of fracture healing:which are the important molecules?', *Injury* **38**(1, Supplement 1), S11 – S25.

Turing, A. M. (1952), 'The chemical basis of morphogenesis', *Philosophical Transactions of the Royal Society of London. Series B, Biological Sciences* **237**(641), 37–72.

Umulis, D., O'Connor, M. B. & Blair, S. S. (2009), 'The extracellular regulation of bone morphogenetic protein signaling', *Development* **136**(22), 3715–3728.

Urist, M. (1965), 'Bone: formation by autoinduction.', *Science* **150**(3698), 893–899.

van Gaalen, S. M., Kruyt, M. C., Geuze, R. E., de Bruijn, J. D., Alblas, J. & Dhert, W. J. (2010), 'Use of fluorochrome labels in in vivo bone tissue engineering research', *Tissue Engineering Part B: Reviews* **16**(2), 209–217.

van Leer, B. (1974), 'Towards the ultimate conservative difference scheme. ii. monotonicity and conservation combined in a second-order scheme', *Journal of Computational Physics* **14**(4), 361–370.

Versteeg, H. K. (1995), *An introduction to computational fluid dynamics the finite volume method*, Pearson Education.

Wan, D. C., Pomerantz, J. H., Brunet, L. J., Kim, J.-B., Chou, Y.-F., Wu, B. M., Harland, R., Blau, H. M. & Longaker, M. T. (2007), 'Noggin suppression enhances in vitro osteogenesis and accelerates in vivo bone formation', *Journal of Biological Chemistry* **282**(36), 26450–26459.

Warzecha, J., Seebach, C., Flinspach, A., Wenger, F., Henrich, D. & Marzi, I. (2013), 'Effect of sonic hedgehog/β-TCP composites on bone healing within the critical-sized rat femoral defect', *Experimental and Therapeutic Medicine* **5**(4), 1035–1039.

Welch, R. D., Birch, J. G., Makarov, M. R. & Samchukov, M. L. (1998), 'Histomorphometry of distraction osteogenesis in a caprine tibial lengthening model', *Journal of Bone and Mineral Research* **13**(1), 1–9.

Wozney, J., Rosen, V., Celeste, A., Mitsock, L., Whitters, M., Kriz, R., Hewick, R., Wang, E. et al. (1988), 'Novel regulators of bone formation: molecular clones and activities.', *Science* **242**(4885), 1528–1534.

Xiao, Z., Camalier, C. E., Nagashima, K., Chan, K. C., Lucas, D. A., de la Cruz, M. J., Gignac, M., Lockett, S., Issaq, H. J., Veenstra, T. D., Conrads, T. P. & Beck, G. R. (2007), 'Analysis of the extracellular matrix vesicle proteome in mineralizing osteoblasts', *Journal of Cellular Physiology* **210**(2), 325–335.

Yang, L., Jin, Y. et al. (1990), 'Immunohistochemical observations on bone morphogenetic protein in normal and abnormal conditions.', *Clinical Orthopaedics & Related Research* (257), 249–256.

Yoshimura, Y., Nomura, S., Kawasaki, S., Tsutsumimoto, T., Shimizu, T. & Takaoka, K. (2001), 'Colocalization of noggin and bone morphogenetic protein-4 during fracture healing', *Journal of Bone and Mineral Research* **16**, 876–884.

Yoshizaki, K., Seo, Y., Nishikawa, H. & Morimoto, T. (1982), 'Application of pulsed-gradient 31P NMR on frog muscle to measure the diffusion rates of phosphorus compounds in cells', *Biophysical Journal* **38**(2), 209–211.

Young, M., Carroad, P. & Bell, R. (1980), 'Estimation of diffusion coefficients of proteins', *Biotechnology and Bioengineering* **22**(5), 947–955.

Zhao, B., Katagiri, T., Toyoda, H., Takada, T., Yanai, T., Fukuda, T., Chung, U.-i., Koike, T., Takaoka, K. & Kamijo, R. (2006), 'Heparin potentiates the in vivo ectopic bone formation induced by bone morphogenetic protein-2', *Journal of Biological Chemistry* **281**(32), 23246–23253.

Zimmerman, L., De Jesús-Escobar, J. & Harland, R. (1996), 'The Spemann organizer signal noggin binds and inactivates bone morphogenetic protein 4', *Cell* **86**(4), 599–606.